
LIMITATIONS AND ADVANCES IN THE FIELD
OF FAR-INFRARED/SUBMILLIMETRE
EXTRAGALACTIC ASTRONOMY

or

THE TROUBLE WITH TERRAHERTZ

Gwenifer Raymond

A thesis submitted to Cardiff University, for the degree of

Doctor of Philosophy

September, 2011

Acknowledgements

So, I suppose I should start out by thanking my parents. You know, for all the little things, like bringing me into existence, feeding me, clothing me, buying me Star Wars toys, defending me from bear attacks. Stuff like that seems kind of important in hindsight I guess. So, thanks!

Obviously after that come my supervisors, Steve Eales and Kate Isaak, for their guidance and their telling me what to do when I needed help and was on the edge throwing my computer into an endless fire pit fuelled by incomprehensible graphs and nerd rage.

Then come my office mates, Robbie Auld, Simon Dye and Steve Flynn for politely ignoring my sporadically screamed obscenities at whatever sheet of paper was drawing my ire on that particular day.

Rounding this list up are fellow postgrads. Rhys Taylor, maintainer of the magnificent beard and co-watcher of Star Trek and some truly awful, awful movies. Sarah and Ian Harry, one for being the co-founder of cake day - laying a firm foundation for fat postgrads in the years to come - and the other, for avidly competing to make the geekiest jokes possible. Sara Carver, whom I loathe for being the only friend with a bigger dvd collection and tv than me. Elizabeth Pearson, for two simple reasons. Oliver Lomax, because of all the souls I've encountered in my travels, his was the most... *human*. Actually, no, never mind, thanks for nothing you guys.

A portion of the work presented in this thesis is based on observations obtained with MegaPrime/MegaCam, a joint project of CFHT and CEA/DAPNIA, at the Canada-France-Hawaii Telescope (CFHT) which is operated by the National Research Council (NRC) of Canada, the Institut National des Science de l'Univers of the Centre National de la Recherche Scientifique (CNRS) of France, and the University of Hawaii. Another portion the of work is based in part on data products produced at TERAPIX and the Canadian Astronomy Data Centre as part of the Canada-France-Hawaii Telescope Legacy Survey, a collaborative project of NRC and CNRS.

Abstract

I present new optical and infrared photometry for a statistically complete sample of seven sources selected at 1.1 mm. Comparing their photometric redshifts with redshifts from previous 850 μm selected surveys indicates that 1.1 mm selected surveys may be better at finding high redshift sources. I also perform a banded V_e/V_a analysis on the sample, and find no evidence for a redshift cutoff in the space density of sources. However, the sample size is very small. I perform the same analysis on a statistically complete sample of 38 galaxies selected at 850 μm . I find a evidence for a drop off in space density of sources beyond between $z \sim 1-2$ as well as for the existence of two differently evolving sub-populations separated in luminosity.

I present a sample of SPIRE sources, selected at 250 μm , with a set of previously collected ancillary photometry and either spectroscopic or photometric redshifts. I find that only $\sim 1/4$ of the sources at redshifts $z \sim 1$ show evidence of undergoing a major merger. I find evidence to support a downsizing model of galaxy evolution, where the most massive galaxies form first. I find some correlation with star formation rate and the gas mass of a galaxy, therefore the drop in cosmic star formation rate since $z = 1$ may be caused by a coinciding drop in the average gas mass of galaxies over this era.

Finally, I discuss the possibility of using imaging spectrometers to break through the confusion limit. Taking the SAFARI instrument as a test case I find that I can uniquely identify galaxies by their redshift, determined via an automated method. I find that this method works for galaxies with fluxes as much as ten times below the traditional continuum confusion limit. I also find that I can uniquely identify spectrally confused sources.

A long time ago in a galaxy far, far away. . . .

Contents

1	Introduction	1
1.1	The View in Infrared	1
1.2	Observing in the Infrared	2
1.2.1	Transmission of the Atmosphere	2
1.2.2	The History of Infrared Astronomy	3
1.3	Technical Limitations and Selection Effects in IR Astronomy	7
1.3.1	K-Correction	8
1.3.2	Angular Resolution and Confusion	8
1.4	The Cosmic Infrared Background	12
1.4.1	The Infrared Galaxy Population	14
1.4.2	The Evolution of the CIB	16
1.5	The Future of Extragalactic Infrared Astronomy	17

1.6	This Work	18
2	Is There a Redshift Cutoff for Submillimetre galaxies?	21
2.1	Introduction	21
2.2	New Images and Photometry for the AzTEC Sample	24
2.2.1	Notes on Individual Objects	26
2.3	Estimated Redshifts for the AzTEC Sample	33
2.4	A Banded V_e/V_a Analysis	37
2.5	Conclusions	42
3	Morphology Versus Redshift of Herschel Sources in the GOODS-N Field	45
3.1	Introduction	45
3.2	Data	47
3.2.1	SPIRE Photometry	48
3.2.2	Identifying Optical Counterparts	55
3.2.3	Ancillary Data	57
3.3	Estimating Photometric Redshifts	58
3.4	Morphology as a Function of Redshift	64

3.5	Discussion	72
3.6	Conclusions	83
4	Star Formation Rates of Herschel Galaxies in the GOODS-N Field	85
4.1	Introduction	85
4.2	The da Cunha et al. (2008) Model	88
4.3	Data	89
4.4	Results & Discussion	90
4.4.1	Star Formation Rate as a Function of Redshift	93
4.4.2	Star Formation Rate as a Function of Stellar Mass	94
4.4.3	Star Formation Rate as a Function of Dust Mass	98
4.5	Conclusions	100
5	The Effectiveness of MIR/FIR Blind, Wide Area, Spectral Surveys in Breaking the Confusion Limit	103
5.1	Introduction	103
5.2	Extracting Redshifts From an Artificial Sky	107
5.2.1	Generating an Artificial Sky	108
5.2.2	Generating Datacubes/Source Catalogs	115

5.2.3	Detecting Sources and Extracting Their Redshifts	117
5.3	Results	125
5.3.1	Results From Clements et al. (2007)	125
5.3.2	Analysis Using FIR Emission Lines Only	126
5.3.3	Extending Analysis to MIR	127
5.4	Discussion	129
5.5	Conclusions	134
6	Spectral Line Confusion in SAFARI Surveys	137
6.1	Introduction	137
6.2	The Model Spectra	139
6.3	Simulations	144
6.3.1	Modifications to the Algorithm	144
6.4	Results & Discussion	150
6.4.1	As a Function of Flux	150
6.4.2	As a Function of Redshift	156
6.5	Conclusions	163

7	Conclusions	165
7.1	Selecting Galaxies at 1.1 mm	165
7.2	The Origin of the Decline in the Cosmic Star Formation Rate . . .	166
7.3	Breaking Through the Confusion Limit	167
7.4	Finally...	168
A	The Instrumental Specifications of SAFARI	171

List of Tables

2.1	Photometry for the AzTEC sources.	32
2.2	The best photometric redshift fits for the AzTEC sources.	34
3.1	The SPIRE 250 μm , 350 μm and 500 μm fluxes ($S_{250\mu\text{m}}$, $S_{350\mu\text{m}}$ and $S_{500\mu\text{m}}$ respectively) for of each of the 116 SPIRE sources in the region covered by the EIP ancillary photometry.	49
3.2	The collected EIP ancillary photometry for the 74 SPIRE sources with a single optical counterpart.	59
3.3	The photometric redshift estimates (z_{photo}), 1σ errors and reduced χ^2 fit values for each of the 74 SPIRE sources with a single optical counterpart.	65
3.4	The total number of sources that lie in the redshift bands $z < 0.4$, $0.4 < z < 0.8$, $0.8 < z < 1.2$, $1.2 < z < 1.6$, $1.6 < z < 2.0$ and $z > 2.0$, subdivided into number of single source counterparts, possible merger system counterparts, and isolated spiral counterparts	69

3.5	My estimated number of contaminants, the percentage of mergers (corrected for contamination) and the percentage of isolated spirals that lie in the redshift bands $z < 0.4$, $0.4 < z < 0.8$, $0.8 < z < 1.2$, $1.2 < z < 1.6$, $1.6 < z < 2.0$ and $z > 2.0$	80
5.1	Sources used for the addition of MIR lines to the template spectra that populate the data cube.	113
5.2	Lines used in source redshift-determination through template fitting for the FIR emission line only method.	124
5.3	Lines used in source redshift-determination through template fitting for the method using both FIR and MIR emission lines.	125
5.4	The percentage of sources with accurately recovered redshifts for primary and secondary sources, using FIR emission lines only as well as both MIR and FIR emission lines, and employing cutoff fluxes of $S_{120\mu m} > 0.342$ mJy and $S_{120\mu m} > 1$ mJy.	129
6.1	Emission lines included in the model spectra for the template galaxies.	141
6.2	Template emission lines used in the redshift fitting procedure. . . .	148

List of Figures

1.1	The percentage transmission of the Earth's atmosphere as a function of wavelength, in the MIR to FIR/submm.	4
1.2	A plot of the same blackbody at redshifts $z = 1$ and $z = 2$. At $z = 2$ a brighter portion of the SED has been shifted into the waveband at $250 \mu\text{m}$, than at $z = 1$	9
1.3	The predicted flux density of IR and submm galaxies as a function of redshift and wavelength.	9
1.4	Estimate of the cosmic optical and infrared backgrounds in the Universe.	13
2.1	Subaru i+ band cutouts for AzTEC1 to 7, with the exception of AzTEC4 and 6, which are the combined CFHT and Subaru i-band images.	27
2.2	The best spectral fits for the AzTEC sources and their marginalized reduced χ^2 distribution as a function of redshift.	35

2.3	Flux versus redshift for both the cold and hot SEDs.	39
2.4	The distribution of the values of $\langle V_e/V_a \rangle$ with z_{low} for the GOODS-N sample.	40
2.5	The distribution of the values of $\langle V_e/V_a \rangle$ with z_{low} for the GOODS-N sample, using only the sources with reliable identifications.	41
2.6	The distribution of the values of $\langle V_e/V_a \rangle$ with z_{low} for the GOODS-N sample, where four (roughly half) of the unreliable identifications have been pushed to redshifts of $z = 4$	42
2.7	The distribution of the values of $\langle V_e/V_a \rangle$ with z_{low} for the AzTEC sample.	43
3.1	HST/ACS F850LP band photometry overlain with IRAC 3.5 μ m flux contours showing examples of a possible multiple source and an isolated source.	56
3.2	A plot of the estimated photometric redshift (z_{photo}) versus the B08 spectroscopic redshift (z_{spec}) for each EIP source where a spectroscopic redshift is available.	63
3.3	A plot of the estimated photometric redshifts (z_{photo}) versus the B08 spectroscopic redshifts (z_{spec}) for each of the SPIRE sources with a single optical counterpart, where a spectroscopic redshift is available.	64
3.4	The ACS F850LP band cutouts for SPIRE sources at redshifts $z < 0.4$	68

3.5	The ACS F850LP band cutouts for SPIRE sources at redshifts $0.4 < z < 0.8$	70
3.6	The ACS F850LP band cutouts for SPIRE sources at redshifts $0.8 < z < 1.2$	73
3.7	The ACS F850LP band cutouts for SPIRE sources at redshifts $1.2 < z < 1.6$	77
3.8	The ACS F850LP band cutouts for SPIRE sources at redshifts $1.6 < z < 2.0$	78
3.9	The ACS F850LP band cutouts for SPIRE sources at redshifts $z > 2.0$	79
4.1	Some example best fit model SEDs for my data set.	91
4.2	Probability distributions for two of the outlying galaxies. Examples are shown for extreme outliers in M_{star} and in SFR.	92
4.3	Median likelihood estimations of star formation rate (SFR) as a function of redshift (z).	93
4.4	Median likelihood estimations of specific star formation rate ($sSFR = SFR/M_{star}$) as a function of redshift (z).	95
4.5	Median likelihood estimates of star formation rate (SFR) versus stellar mass (M_{star}).	96
4.6	Median likelihood estimates of specific star formation rate ($sSFR$) versus stellar mass (M_{star}).	97

4.7	Median likelihood estimates of star formation rate (SFR) versus dust mass (M_{dust}).	99
4.8	Median likelihood estimates of specific star formation rate ($sSFR$) versus dust mass (M_{dust}).	100
5.1	An example spectrum with an approximate dust temperature of 35K, with the strong [OI] and [CII] lines shortward and longward of the SED peak, respectively.	106
5.2	Template spectra which were used to populate the datacube.	112
5.3	A plot of the flux and redshift distributions, for each SED type, of the sources that populate the bright-end and burst mode evolution data cubes.	114
5.4	A flowchart of the order in which the sources are observed and then the redshift-determination method implemented.	118
5.5	A sample spectrum as can be found in the artificial ‘skies’, and the example spectrum after the continuum fit has been subtracted.	119
5.6	Plots of the 120 μm continuum flux distribution for both the total input primary sources and primary sources with accurately determined redshifts.	128
5.7	Plots of the 120 μm continuum flux distribution for both the total input secondary sources and secondary sources with accurately determined redshifts.	130

5.8	Plots of the cumulative fractional recovery of sources (fraction of sources accurately recovered with flux less than that defined by the x-axis) with increasing $120\ \mu\text{m}$ flux, measured as a fraction of the traditional $120\ \mu\text{m}$ continuum confusion limit.	132
6.1	The rest frame template spectra used in this work and their $40\ \mu\text{m}$ flux as a function of redshift.	145
6.2	The results from running the modified continuum fitting method on a confused spectrum.	149
6.3	The average percentage of component sources with accurately estimated redshifts for spectra made up of two component sources as a function of the $40\ \mu\text{m}$ flux of each of the component sources.	152
6.4	The distribution of sources with accurately estimated redshifts as a function of the redshift of each of the component galaxies.	157

Chapter 1

Introduction

1.1 The View in Infrared

Astronomical observations in the mid/far infrared (MIR/FIR) and submillimetre (submm) is still a relatively young field of science. There have, however, in recent years been a number of great leaps forward in the capabilities of the instruments, and therefore also in our understanding of the Universe at these wavelengths. There are a number of instruments currently operating, providing a stream of new insights, and those instruments planned for the future should endow even more important developments to come.

The MIR and FIR/submm are defined as being the areas of the electromagnetic spectrum that lie in the wavelength bands 5 - 30 and 30 - 1000 μm , respectively. The IR is uniquely sensitive to objects at relatively cold temperatures, typically between $\sim 3 - 2000\text{K}$. Most of the emission from galaxies at these wavelengths comes from thermal continuum emission by dust grains. The remainder comes

from fine-structure atomic and molecular rotational line emission. The thermal dust emission is caused by optical/UV photons emitted by stars being absorbed by dust grains in the galaxy. The dust is then heated and the light re-emitted in the IR.

There is much evidence to support the idea that the vast majority, if not all galaxies go through an IR phase in their evolution, when the peak of their continuum emission is emitted in this wavelength region (e.g., Blain et al., 2002). Independent observations in the optical (Bouwens et al., 2007) and IR (Pascale et al., 2009) both appear to show that this phase occurred at redshifts $z \sim 1 - 3$. Therefore, the IR waveband is critical for a full understanding of this phase of galaxy evolution.

1.2 Observing in the Infrared

1.2.1 Transmission of the Atmosphere

One of the main difficulties in IR astronomy is the opacity of the Earth's atmosphere at these wavelengths. Water vapour in the upper regions of the atmosphere absorbs IR radiation over all but a few wavelength bands. Therefore, IR observations need to be made from above the majority of this water vapour; either from very high altitude sites, or from space.

An example profile of the Earth's atmosphere's transmission as a function of wavelength is shown in figure 1.1. This shows the IR transmission spectrum as seen from a site at the summit of Mauna Kea - one of the best ground based observing sites. There are a number of 'windows' across various wavebands where the absorption by the atmosphere is low enough that observations may be made from a

high altitude site. These windows exist at around $\sim 10, 20, 350, 450, 600, 750$ and $800 \mu\text{m}$. However, observations at 350 and $450 \mu\text{m}$ are still extremely difficult, even at high altitude sites. FIR observations between $\sim 20 - 350 \mu\text{m}$ are not possible from ground based sites, and thus must be made from space based observatories.

1.2.2 The History of Infrared Astronomy

IR radiation was first discovered by William Herschel in 1800. When passing sunlight through a prism he found that if he held a thermometer just beyond the red end of the spectrum, the thermometer showed a higher temperature rise than when it was exposed to the visible sunlight. He concluded with some further experimentation that there must be some form of invisible light beyond the red end of the visible spectrum.

The first IR all-sky map was made in 1967 by Hi Star, operated by the Air Force Cambridge Research Laboratory. The observations were taken by cooled IR telescopes placed on rockets, which allowed the sky to be observed for minutes at a time. Several high-altitude, ground-based observatories were also built around this time, including the Mauna Kea observatory in 1967.

The next great leap came in 1974 with the Kuiper Airborne Observatory (KAO) (Cameron, 1976), an IR telescope mounted on a C-141A jet transport aircraft which flew up to altitudes of 41,000 feet, which is above 99% of the Earth's water vapour. KAO continued to operate for the next 20 years making many discoveries, including the ring of Uranus and water in the atmospheres of Jupiter and Saturn.

A huge leap forward came in 1983 with the first ever cryogenic, space-borne, IR observatory: IRAS (Infrared Astronomical Satellite). IRAS surveyed 96% of the

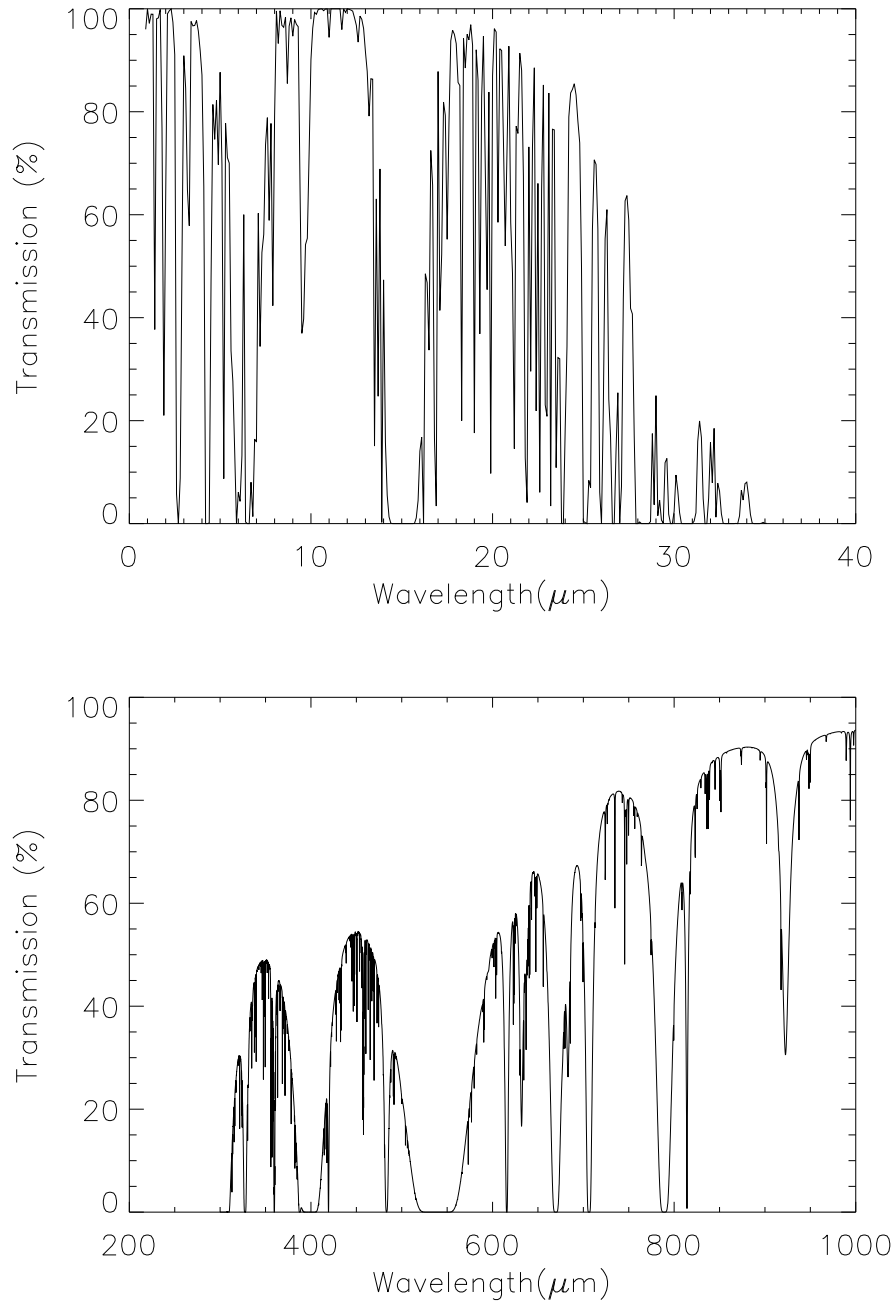


Figure 1.1: (*Values taken from Joint Astronomy Centre, 2004*) The percentage transmission of the Earth's atmosphere as a function of wavelength, in the MIR to FIR/submm. Results are as viewed from a site on the summit Mauna Kea.

sky with its four broadband filters at 12, 25, 60 and 100 μm , down to a limiting flux of approximately a Jy (Neugebauer et al., 1984). IRAS detected roughly 500,000 IR sources, doubling the number of known IR sources at the time.

A number of IR satellites were launched in the following years, including the Infrared Space Observatory (ISO, Kessler et al., 1996), launched by the European Space Agency (ESA) in 1995. ISO was much more sensitive than IRAS and covered a wider wavelength band, with the Infrared Camera instrument (ISOCAM, Cesarsky et al., 1996) covering the region 2.5 - 17 μm and the Photo-polarimeter (ISOPHOT, Lemke et al., 1996) instrument covering the region 2.5 - 240 μm . ISO also had on board high-resolution spectrometers which gave us the first sensitive spectroscopic surveys of the sky, including the Short Wave Spectrometer (ISO-SWS, de Graauw et al., 1996) covering the region 2.4 - 45 μm and the Long Wave Spectrometer (ISO-LWS, Clegg et al., 1996) covering the region 45 - 196.8 μm . Operating for around 2.5 years, ISO led to a number of new discoveries including the first detections of large amounts of dust in the spaces between galaxies, previously thought to be empty.

In 2003, NASA's *Spitzer* Space Telescope was launched (Werner et al., 2004); the payload consisting of 3 instruments:

- Infrared Array Camera (IRAC, Fazio et al., 2004),
an imaging photometer with four arrays designed to observe at 3.5, 4.5, 5.8 and 8.0 μm .
- Infrared Spectrograph (IRS, Houck et al., 2004),
a spectrograph providing both low and high-resolution spectroscopy across the 5 - 40 μm waveband.

- Multiband Imaging Photometer (MIPS, Rieke et al., 2004),

an imaging photometer with three cameras designed to observe at 24, 70 and 160 μm .

Spitzer is still operating at present (September 2011), and has given us an unprecedentedly sensitive view of the IR Universe over a broad range of wavelengths. However, its relatively small dish size (0.6 m) means that its observations are extremely limited in terms of angular resolution.

The *Herschel* Space Observatory was successfully launched in May 2009 (Pilbratt et al., 2010). *Herschel*, an ESA space-based FIR observatory, operates over the wavelength range 55-671 μm . It carries a 3.5 m dish passively cooled to 160 K. The science payload consists of 3 instruments:

- Photodetector Array Camera and Spectrometer (PACS, Poglitsch et al., 2010),

an imaging camera and spectrometer covering the wavelengths between 55 - 210 μm . The spectrometer has a spectral resolution between $R = 1000 - 5000$.

- Spectral and Photometric Imaging Receiver (SPIRE, Griffin et al., 2010),

an imaging camera with 3 detectors centered on 250, 350 and 500 μm , with 5σ 1 hour sensitivities of up to 7.8, 9.2 and 10 mJy, respectively, as well as a Fourier Transform spectrometer covering the region 200 - 670 μm with a spectral resolution between $R = 20 - 1000$ at 250 μm .

- Heterodyne Instrument for the Far Infrared (HIFI, de Graauw et al., 2010),

a heterodyne instrument designed to provide extremely high (as much as $R = 10^7$) resolving power, over as broad a waveband as possible. The spec-

trometer can be operated over two wavebands: 157 - 212 μm and 240 - 625 μm .

Herschel offers a combination of higher (relative to ISO/*Spitzer*) angular resolution, sensitivity and large field of view over a relatively unexplored waveband, that will allow us to view great amounts of the previously unseen IR universe. *Herschel* is expected to be operational from launch for a period of ~ 3 years.

1.3 Technical Limitations and Selection Effects in IR Astronomy

It is important, in order to fully understand the results from IR/submm observations, to be able to quantify their limitations and selection effects, and be able to tightly constrain their effect on the results from observations.

One of the most difficult aspects of IR and submm astronomy is the identification of optical counterparts. This is due to a number of reasons. IR/submm observations are typically of poorer angular resolution than optical observations. This, in conjunction with the faintness of IR/submm bright galaxies in the optical - due to their high dust contents - makes the identification of these optical counterparts very difficult. However, there is a benefit of observations in the IR/submm, beyond about 100 - 200 μm (the typical wavelength of the SED peak) - that of the negative K-correction due to the shape of galaxies' spectral energy distributions (SEDs).

1.3.1 K-Correction

A benefit of observing IR/submm galaxies is that, due to the shape of their SED, as their redshift increases the peak of their SED moves into the observed waveband. An example shown in figure 1.2 illustrates the effect where at higher redshifts a brighter portion of the SED has been shifted into the FIR waveband. The effect is a negative K-correction which results in a counteraction against the dimming of the galaxy from the increasing luminosity-distance. Figure 1.3 shows this effect in action. As the galaxies move to higher redshifts the peak of their SED emission move into the various wavebands. The effect is strongest in the longer wavelength bands (typically the effect is only useful when operating at wavelengths $\lambda > 100 \mu\text{m}$, at wavelengths shorter than this, there can actually be a positive K-correction, which makes galaxies appear fainter), where the effect of the negative K-correction dominates over the dimming from the increase in luminosity distance, over a certain redshift range.

The negative K-correction effect gives IR/submm galaxies an increased apparent brightness at higher redshifts that is unavailable in other wavelength regimes. As such the IR/submm wavebands may provide a uniquely suitable platform for observing galaxies at moderate to high redshifts.

1.3.2 Angular Resolution and Confusion

The angular resolution of a telescope, θ , is described by the equation:

$$\theta = \frac{1.22\lambda}{D} \tag{1.1}$$

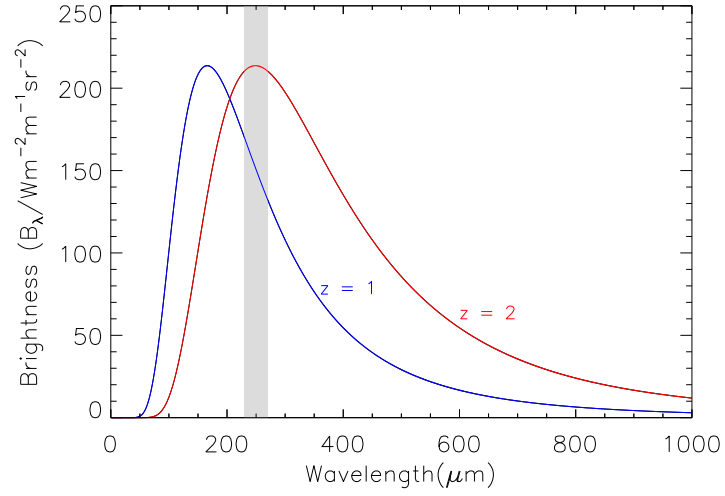


Figure 1.2: The red line represents a 35 K blackbody redshifted to $z = 1$, and the blue line represents a 35 K blackbody redshifted to $z = 2$ (ignoring the effects of dimming from increasing luminosity-distance). The grey region of the plot shows an example FIR 230 - 270 μm waveband. At the higher redshift, a brighter portion of the SED has been shifted into the $\sim 250 \mu\text{m}$ waveband.

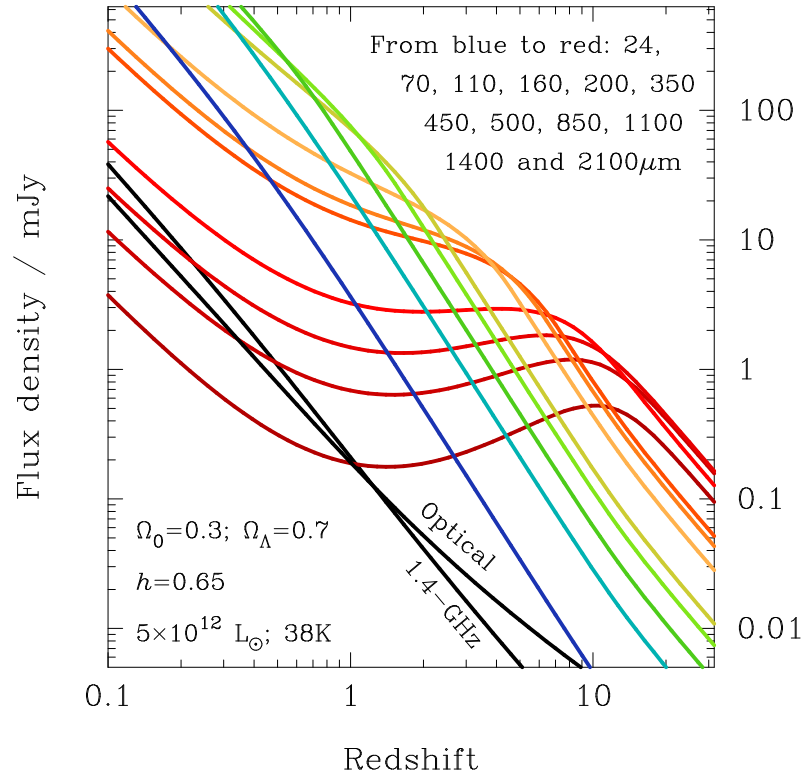


Figure 1.3: (Figure taken from Blain et al., 2002) The predicted flux density of IR and submm galaxies as a function of redshift and wavelength.

Where λ = the wavelength of observation and D = the diameter of the telescope dish.

Thus, the resolution of an IR observation is much coarser than one at, for example, optical wavelengths, for a telescope with the same dish size. Therefore if we want IR observations to be at as high a resolution as those at shorter wavelengths, we need to use telescopes with wider diameter dishes.

Problems arise though when considering the fact, as was discussed earlier, that some portions of the IR waveband cannot be observed from ground based observatories - i.e. they must be made from space. Due to the restrictions on the size and weight of a payload that can be taken into space by a rocket there is a strict limit on the size of dish a space based telescope can have - which then, in turn, limits the achievable angular resolution.

The coarseness of the angular resolution of IR/submm observations compared to those at optical wavelengths can make the cross-identification (XID) of IR/submm counterparts extremely difficult. One method of XIDing an optical counterpart for an IR/submm source makes use of high-resolution radio observations. There is a strong relationship that has been found - both locally and at high redshifts - between the IR and radio flux of a galaxy (e.g. Price & Duric, 1992; Yun et al., 2001; Vlahakis et al., 2007). Due to the relatively low surface density of radio sources on the sky, the probability of a radio source and an IR source being coincident on the sky purely by chance is very small. As radio observations can be made from the Earth's surface, very high resolution observations can be made using extremely large dishes, or interferometers with wide baselines. Therefore, using this IR/radio flux correlation, the spatial coordinates of an IR/submm source can be constrained with very high accuracy. This in turn leads to the much easier identification of an

optical counterpart.

However, the K-correction which allows us to observe IR/submm galaxies at high redshifts, does not similarly benefit radio observations. Therefore, in requiring that IR/submm galaxies also be detected at radio wavelengths, a selection effect is caused which limits observations to galaxies with redshifts $z \lesssim 3$.

Another phenomenon caused by the relatively poor angular resolution of IR observation is that of source confusion. Confusion is caused by the effective blurring of IR sources into one another in deep surveys, greatly reducing our ability to uniquely identify and resolve individual sources. This effectively defines the depth to which deep, wide area IR extragalactic surveys should be conducted. Once the confusion limit has been reached, very little useful further information can be extracted from the data.

The effects of confusion noise can be somewhat overcome through the use of stacking analyses. Such an analysis was performed on confusion-limited data from the Balloon-borne Large Aperture Submillimeter Telescope (BLAST) survey (Devlin et al., 2009; Pascale et al., 2009). Source positions were taken from a *Spitzer* 24 μm catalogue (with IRAC coordinates), within a specified flux density bin. The average flux densities of BLAST objects were then measured at these positions. This was then multiplied by the source density in that bin, and summed over all other bins. This method makes it possible to estimate the contribution of the *Spitzer* galaxies to the cosmic infrared background at BLAST wavelengths, however it doesn't make it possible to resolve the background into individual sources.

A more extreme form of confusion that can occur in IR surveys is that of spectral confusion. Spectral confusion most adversely affects spectral surveys - the spectra

of heavily confused sources can merge, appearing as one single spectrum, with their spectral features not being uniquely resolvable from one-another.

1.4 The Cosmic Infrared Background

The cosmic infrared background (CIB) peaks at $\sim 150 \mu\text{m}$ and comprises the total IR emission from all sources in the sky (e.g. Dole et al., 2001; Elbaz et al., 2002). It has been found to contain as much energy as the combined optical/UV extragalactic background (see figure 1.4). As the most of the CIB is thought to be powered by thermal dust emission, caused by the the absorption of optical/UV photons, this suggests that half of all light emitted by stars and active galactic nuclei (AGN) is absorbed by dust before we are able to observe it in the optical (Hauser & Dwek, 2001). Locally, the IR output of typical galaxies is only one third of their optical output (Soifer & Neugebauer, 1991), which implies strong evolution in the IR properties of galaxies as one moves to high redshift.

Submm galaxies (SMGs), first detected at $850 \mu\text{m}$ with the Submillimetre Common User Bolometer Array (SCUBA) (Holland et al., 1999), are a significant population of high redshift star forming galaxies (e.g., Hughes et al., 1998a; Blain et al., 2002). They are believed to be dust-enshrouded galaxies undergoing prodigious levels of star formation (e.g., Hughes et al., 1998a; Eales et al., 1999) in which the optical/UV radiation emitted by the stars is absorbed by the dust and then re-emitted in the submm. Star formation rates in excess of $1000 \text{ M}_{\odot}\text{yr}^{-1}$ have been inferred (Scott et al., 2002), much higher than locally. The galaxies in these samples have been found to account for up to one tenth of the total CIB (e.g., Dye et al., 2007) and many authors have argued that these galaxies are the progenitors

for the elliptical galaxies we see in the local Universe (Eales et al., 1999; Scott et al., 2002; Dunne et al., 2003).

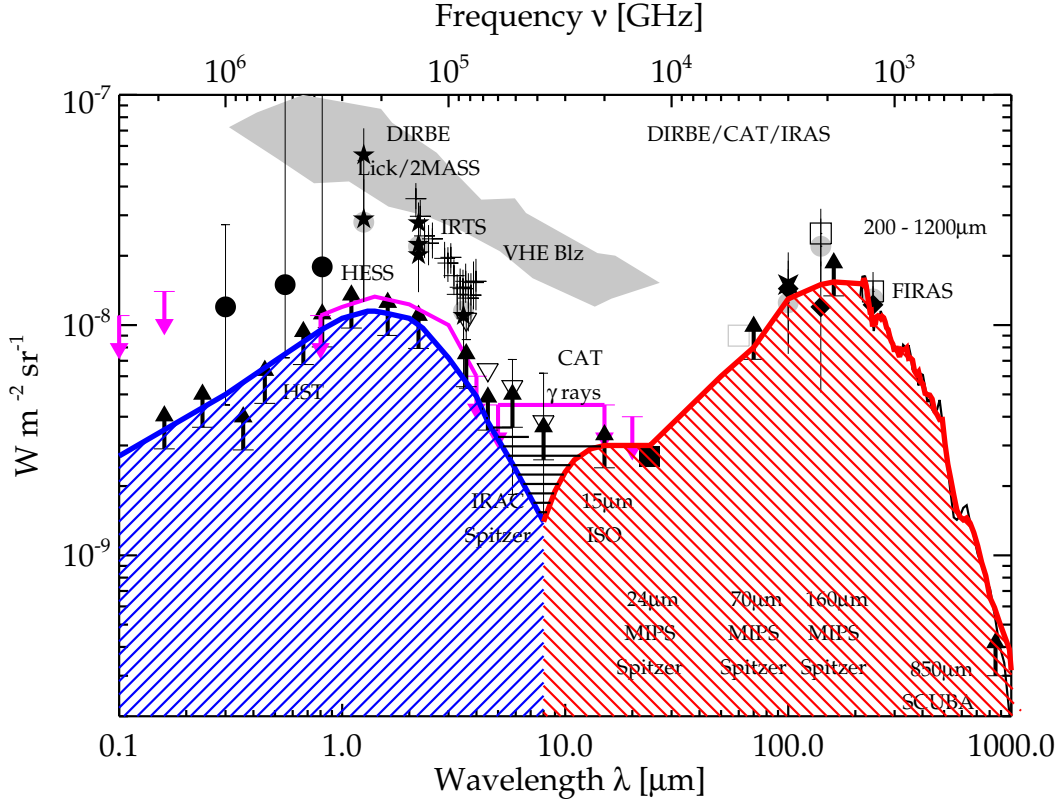


Figure 1.4: (Figure taken from Dole et al., 2006) Estimate of the cosmic optical and infrared backgrounds in the Universe (COB and CIB, respectively). The blue and red shaded regions show the COB and CIB, respectively.

Attempts have been made to resolve the CIB at 15 μm (ISOCAM), 24 μm (MIPS), 160 μm (ISOPHOT) and 850 μm (SCUBA) (Elbaz et al., 2002; Papovich et al., 2004; Juvela et al., 2000; Smail et al., 2002, respectively). However, the peak of the CIB lies at $\sim 150 \mu\text{m}$; a wavelength band which, due to the technical limitations of IR astronomy, has yet to be resolved into individual sources. Thus our understanding of the make-up of the CIB is heavily reliant on extrapolation. For example, the energy density of the CIB at 850 μm , the region at which SMGs were discovered by SCUBA, is ~ 30 times less than that at 150 μm , where the CIB is at its maximum. Therefore the launch of *Herschel*, which is able to observe around the

peak of the CIB and which is unaffected by the opacity of the Earth's atmosphere at these wavelengths, means that we are now able to resolve a significant fraction ($\sim 15\%$, Oliver et al., 2010) of the CIB that has been previously unobservable.

1.4.1 The Infrared Galaxy Population

Galaxies that make the most significant contribution to the CIB (as well as normal galaxies) include :

- High Redshift Galaxies - Galaxies at high redshifts which are observable in the IR/submm due to the beneficial effects of their negative K-correction.
- Starburst Galaxies - Galaxies in which there is strong dust heating powered by intense, ongoing star-formation.
- Active Galactic Nuclei (AGN) - Galaxies in which there is strong dust heating powered by AGN mass accretion.
- Ultraluminous/Luminous Infrared Galaxies (U/LIRGs) - galaxies which have an intrinsic IR luminosity of $L_{8-1000\mu m} > 10^{11} L_{\odot}$ and $L_{8-1000\mu m} > 10^{12} L_{\odot}$ respectively.

U/LIRGs have been found to be, almost exclusively, merging galaxy systems (e.g. Farrah et al., 2001; Bushouse et al., 2002; Veilleux et al., 2002, 2006). They are powered by a composite of AGN mass accretion and star formation heating, and there are a number of spectroscopic diagnostic tools in the MIR that may be used to estimate the contribution each component makes to the total IR luminosity of the galaxy. Typically, we expect a galaxy which is predominantly AGN powered to

be host to a harsher radiation field than a starburst powered galaxy. Knowing this, it is therefore possible to diagnose the heating mechanisms by which the galaxy is powered, using a variety of spectral features (e.g., Genzel et al., 1998; Genzel & Cesarsky, 2000; Laurent et al., 2000).

Another feature commonly seen in IR spectra are polycyclic aromatic hydrocarbons (PAHs). PAHs are particles consisting of fused aromatic rings of hydrogen and carbon which, when exposed to moderately intense UV fields, generate a set of spectral features at 3.3, 6.2, 7.7, 8.6, 11.3 and 12.7 μm (see Puget & Leger, 1989; Duley & Williams, 1981). The PAH features in a predominantly AGN powered galaxy are much weaker than in a starburst powered galaxy. This is most likely due to the destruction of the PAH molecules by the harsher UV field of an AGN powered galaxy.

Other features commonly used to diagnose an IR galaxy's heating mechanisms are the fine structure lines. Again due to the harsher radiation field of an AGN powered galaxy relative to a starburst powered galaxy, we expect to see higher excitation emission lines in the AGN powered galaxies. Therefore, by measuring the relative strengths of certain diagnostic emission lines (eg. $[\text{NeV}]14.3\mu\text{m}/[\text{NeII}]12.8\mu\text{m}$ and $[\text{OIV}]25.9\mu\text{m}/[\text{NeII}]12.8\mu\text{m}$) it is possible, not only to determine what is the dominant heating mechanism, but also the fractional contribution AGN and starburst powering make to the dust heating.

Using these diagnostic methods, observations of local U/LIRGs appear to show that they are dominated by starburst heating (e.g. PAHs - Dudley, 1999; Rigopoulou et al., 1999; Imanishi et al., 2007) (e.g. fine structure lines - Genzel et al., 1998; Sturm et al., 2002; Farrah et al., 2007).

An evolutionary sequence for U/LIRGs was first proposed by Sanders et al. (1988) wherein U/LIRGs, appearing to be systems of merging galaxies, go through an initial starburst dominated phase and then transition into an IR-bright AGN dominated phase. These phases are then followed by an IR-quiet quasar phase and final passive elliptical phase.

SMGs are commonly thought of as being the high-redshift analogue of U/LIRGs. Recent MIR spectroscopic observations of SMGs using the *Spitzer* IRS have shown that SMGs are typically starburst heating dominated (Menéndez-Delmestre et al., 2007; Pope et al., 2008). However, there also appears to be a smaller population of AGN powered SMGs, which may represent a slightly later stage in the evolution of SMGs (Coppin et al., 2010), in agreement with the high-redshift interpretation of the evolutionary model presented in Sanders et al. (1988).

The reliable determination of the processes by which IR galaxies are powered is, to date, still extremely difficult. There is increasing evidence for differences in the heating mechanisms between local U/LIRGs and SMGs (e.g., Hailey-Dunsheath, 2008; Menéndez-Delmestre et al., 2009). Therefore, in order to more fully understand the nature of the sources making up the CIB, observations must not only be able to spatially resolve those component sources, but they must also be able to spectrally resolve emission features, thereby providing insight on their ongoing internal processes.

1.4.2 The Evolution of the CIB

Locally, LIRGs make a negligible contribution to L_{bol} per unit comoving volume. However, their contribution increases by a factor of ~ 70 by redshifts $z \sim 1$ (e.g.,

Chary & Elbaz, 2001; Le Floch et al., 2005). There is considerable evidence for a coinciding increase in the cosmic star formation rate (the average star formation rate per unit mass) by a factor of ~ 10 over this same redshift range (e.g., Lilly et al., 1996; Hogg et al., 1998; Madau et al., 1998; Flores et al., 1999; Haarsma et al., 2000; Hopkins, 2004). The decline in star formation rate since $z \sim 1$ has been linked to the coinciding decrease in the number of LIRGs (Le Floch et al., 2005). As LIRGs appear locally to be powered by mergers (Sanders & Mirabel, 1996), it is not unreasonable to postulate that the decrease in the cosmic star formation rate may be caused by a decline in the number of major mergers since redshift $z \sim 1$.

In this thesis I will present *Herschel*/SPIRE data with ancillary optical data and use this to determine whether a decline in the rate of mergers since this redshift could be the cause for the decline in the cosmic star formation rate - or whether it can be otherwise accounted for.

1.5 The Future of Extragalactic Infrared Astronomy

There are a number of planned space based IR missions for the near future. Of particular note is the proposed JAXA-led SPICA (Space Infrared Telescope for Cosmology and Astrophysics) mission (Nakagawa, 2010)¹. It will have a primary dish diameter of 3.2m, which will be cooled down to < 6 K, and so will offer a great leap in sensitivity over *Herschel*. One of the included onboard instruments will be

¹As SPICA, and its onboard instruments, is currently an instrumental concept, its technical specifications are still under revision. Throughout this thesis, use is made of a number of different revisions of these specifications, the details of which can be found in appendix A

SAFARI (SpicA FIR Instrument) - a high resolution, imaging, Fourier Transform spectrometer, covering the 35 - 210 μm waveband with an instantaneous FoV of $2' \times 2'$. It will offer a range of resolving powers, varying from $R \sim 20$ - 2000 between its low and high resolution modes. Its 5σ 10 hour sensitivity is currently estimated to be 2 mJy.

At a resolving power of $R = 1000$ (at 120 μm) the wavelength resolution of SAFARI is matched to the typical width of emission lines in the MIR/FIR. Clements et al. (2007) has suggested that, since MIR/FIR emission lines may be several times brighter than the traditional continuum confusion limit, that they could be used to overcome some of the effects of confusion. The work modeled the use of a FIR imaging spectrometer, with the specifications of SAFARI, in resolving spatially confused sources via the detection of FIR/MIR emission lines and subsequent estimation of the source redshift. In this thesis I present the results of my own investigation, which models a much larger region of sky, populated by sources using two different evolutionary models, with more realistic spectra, representative of the sky as observed by an imaging spectrometer with the specifications of SAFARI. I also perform a more rigorous investigation into the ability of the same method to resolve spectrally confused sources.

1.6 This Work

Chapter 2 :

I present a set of new optical and IR photometry, and a set of photometric redshifts, for a statistically complete set of seven sources selected at 1.1 mm, with accurate coordinates. I perform a banded V_e/V_a analysis on this galaxy set, and on a

statistically complete sample of 38 galaxies selected at $850\ \mu\text{m}$ from the GOODS-N field. In doing this, I examine the results for evidence of a redshift cutoff in the space density of the sources - and whether the galaxy sample can be separated into differently evolving sub-populations.

Chapter 3 :

I present a set of SPIRE photometry for 116 sources selected at $250\ \mu\text{m}$ in the GOODS-N field, as well as a set of previously collected ancillary photometry at UV, optical, NIR and MIR wavelengths. Most of these sources have spectroscopic redshifts. Where one is not available I estimate a photometric redshift. I then separate these sources into sets of redshift bands and count how many sources show evidence of undergoing mergers or have spiral morphology in each band.

Chapter 4 :

I use the model of da Cunha et al. (2008) to obtain median likelihood estimates of star formation rates, stellar masses and dust masses for the galaxy sample presented in chapter 3. I plot star formation rate as a function of redshift, stellar mass and dust mass, in order to attempt to determine what may be the cause in the dramatic decrease in star formation rate since redshifts $z \sim 1$.

Chapter 5 :

I present the results of my investigation into the effectiveness of MIR/FIR, wide-area spectroscopic surveys in breaking the confusion limit. I use SAFARI, a FIR imaging Fourier Transform Spectrometer concept for the proposed JAXA-led SPICA mission, as a test case. I generate artificial skies representative of 40 SAFARI footprints, populated with sources based on two different galaxy evolution models. I implement a fully automatic redshift estimation algorithm on these artificial skies in order to determine how well I can use this method to uniquely

resolve the sources, and through using this additional information, whether I am able to distinguish between the two evolutionary models.

Chapter 6 :

I present the results of my investigation into how well my fully automated redshift estimation method (as presented in chapter 5) can uniquely identify spectrally confused sources. I constrain the method's efficiency as a function of component source redshift and flux, and attempt to determine what are the key effects which most limit the method's effectiveness in breaking spectral confusion.

Chapter 7 :

I present the main conclusions of all the work presented in this thesis.

Chapter 2

Is There a Redshift Cutoff for Submillimetre galaxies?

2.1 Introduction

Observations of SMGs at ~ 1 mm benefit from a negative K-correction out to high redshifts due the shape of their spectral energy distribution (SED). As the redshift of an SMG increases, the peak of its rest-frame SED moves toward the observed waveband, offsetting the dimming caused by the increasing luminosity distance. This fact accounts for the surprising ability of SCUBA to find large numbers of high-redshift galaxies.

The large amount of dust responsible for the strong submm emission gives rise to high levels of attenuation in the optical. This, in conjunction with the poor angular resolution of single-dish submm facilities, makes the cross identification of SMGs at different wavelengths difficult. Moreover, even when an optical counterpart can

be identified, the high levels of dust attenuation makes the determination of a spectroscopic redshift difficult. As such we are currently unable to determine spectroscopic redshifts for the majority of SMGs. The strong correlation between dust emission and radio emission which appears to hold true in both the low-redshift and high-redshift universe (Vlahakis et al., 2007) has been useful for both identifying the counterparts and estimating redshifts. Due to the low surface density of radio sources on the sky, the probability of the radio counterpart being coincidental with the submm source by chance is small. Due to the high positional accuracy of radio observations, it is then possible to identify the optical counterpart and measure a spectroscopic redshift. It is also possible to estimate the redshift using the ratio of radio to submm flux (e.g., Hughes et al., 1998a; Carilli & Yun, 1999, 2000; Smail et al., 2000).

Chapman et al. (2005), using the Low Resolution Imaging Spectrograph (LRIS) (Oke et al., 1995) on the Keck I telescope, managed to obtain spectroscopic redshifts for a total of 73 radio-identified SMGs with a median $850\ \mu\text{m}$ flux of 5.3 mJy. The galaxies in this sample were found to lie at a median redshift of $z = 2.2$ out to a maximum value of $z_{\text{max}} = 3.6$. However, the K-correction which allows us to detect high-redshift SMGs does not similarly benefit their radio fluxes and so radio identified SMGs are subjected to a radio selection effect which limits redshifts to approximately $z < 3$.

Pope et al. (2006) produced the first complete (i.e. not requiring radio IDs) sample of SMGs selected at $850\ \mu\text{m}$ that has close to 100% redshifts. The sample consists of 35 galaxies, 21 with secure optical counterparts and 12 with tentative optical counterparts, and its completeness means that unlike previous surveys it is not biased towards low- z sources. The median redshift determined for this sample is $z \sim 2.2$. Using this sample, Wall et al. (2008) examined the epoch dependency of

the number density of SMGs. They found an apparent redshift cutoff at $z > 3$ with further evidence for two separately evolving populations, divided by luminosity. However this result was based on calculations using a single model galaxy SED. Since the predicted relationship between submm flux-density and redshift depends strongly on the assumed SED, one of the aims of this chapter is to re-examine their conclusion using a range of empirical SEDs.

There have been a number of explanations for the lack of high-redshift SMGs. Given that dust is thought to form in the atmospheres of highly evolved stars, it is possible that at high redshifts simply not enough time has passed for dust to form (Morgan & Edmunds, 2003). Observations of high-redshift quasars have however detected high levels of dust (e.g., Priddey & McMahon, 2001), suggesting that this is not the explanation. Another possible explanation is that there are fewer large star-forming galaxies at high redshifts.

Eales et al. (2003) presented evidence that SMGs found in 1.1 mm surveys have very low values for the ratio of the 850 μm to 1200 μm fluxes. One possible explanation is that these sources are at very high redshifts. If this is true, then observations at 1.1 mm would be better at finding SMGs at the highest redshifts than observations at 850 μm . A new complete sample of SMGs selected at 1.1 mm located in the COSMOS field (Scoville et al., 2007) has been compiled by Younger et al. (2007). The sources were selected initially at 1.1 mm with the AzTEC camera (Scott et al., 2008; Wilson et al., 2008) on the JCMT. The resultant catalogue consists of 44 sources with $S/N > 3.5\sigma$, 10 of which are robust with $S/N > 5\sigma$. Follow up observations by Younger et al. (2007) were then made with the Submillimetre Array (SMA) at 890 μm for the seven AzTEC sources with the highest signal-to-noise, allowing their positions to be determined with an accuracy of $\sim 0.2''$. The COSMOS field offers a wealth of data over a great number of wavebands including

the optical and infrared. Thus the high positional accuracy makes possible the identification of optical counterparts and hence the determination of photometric redshifts. Of the seven AzTEC sources imaged with the SMA, six have IRAC counterparts, and one source is obscured by a nearby bright galaxy. Using deep Hubble Space Telescope (HST) imaging acquired with the Advanced Camera for Surveys (ACS) (Koekemoer et al., 2007), Younger et al. found optical counterpart candidates for only three of these sources.

In this chapter I carry out a deeper search for the optical counterparts for the AzTEC sources. I use deep imaging with Subaru and the Canada-France-Hawaii-Telescope (CFHT) and find one new possible optical ID. I estimate photometric redshifts for the AzTEC sources using the HYPERZ photometric redshift package (Bolzonella et al., 2000). Throughout this work I employ a concordance cosmological model with $\Omega_{total} = 1$, $\Omega_m = 0.3$, $\Omega_\Lambda = 0.7$ and $H_0 = 75 \text{ kms}^{-1}\text{Mpc}^{-1}$. All magnitudes quoted are AB.

2.2 New Images and Photometry for the AzTEC Sample

I searched for optical counterparts and measured new photometry using deep Subaru¹, CFHT and IRAC images of the AzTEC sources. The IRAC and Subaru images are the publicly available COSMOS images taken by the COSMOS team (Scoville et al., 2007). The CFHT images are taken from the CFHT Deep Legacy Survey. The images I used were taken using the CFHT g_M , r_M , i_M , z_M , Subaru

¹An additional uncertainty of 0.3 mags in the Subaru B_j band magnitudes was taken into account in this photometry due to the possibility of a red leak or a shift in the blue cutoff of this filter.

B_j , V_j , $r+$, $i+$, $z+$ and IRAC channel 1 and 2 filters to average 3σ depths of approximately 28.4, 27.9, 27.6, 26.5, 29.0, 28.2, 28.3, 27.7, 26.4, 24.1 and 23.6 mags respectively.

I searched the i -band images (figure 2.1) at the SMA coordinates. I found bright i -band counterparts for AzTEC1, 3 and 7, all of which were previously known. I also found a faint i -band counterpart for AzTEC5 at the SMA coordinates. I found no objects directly at the SMA coordinates for AzTEC2, but there is a bright object offset from this position by $3''$, meaning that the magnitude limits of this SMG are not useful.

I found no optical counterparts directly at the SMA coordinates for AzTEC4 and 6 in the Subaru and CFHT imaging. For the latter source, however, there is a bright i -band counterpart offset from the SMA position by $\sim 0.6''$ ($\sim 3\sigma$) which could be AzTEC6's counterpart or the true counterpart may be too faint to see. There is also a faint i -band source, offset from AzTEC4's SMA position by $\sim 0.8''$ ($\sim 4\sigma$), in the Subaru imaging. For these two sources I added the i band CFHT and Subaru images, inversely weighting the images by the square of the noise, in order to try and detect any very faint possible counterparts. The stacked i -band images for AzTEC4 and 6 are shown in figure 2.1. I still do not find counterparts at the SMA positions for AzTEC4 and 6 and given the good coincidence between the SMA and optical positions for the other AzTEC sources I tentatively conclude that the true counterparts have not yet been detected.

The typical full-width half-maximum (FWHM) of the optical and IRAC channel 1 and 2 point spread functions (PSFs) are $\sim 0.8''$, $1.66''$ and $1.72''$ respectively. Magnitudes were determined manually by placing apertures onto the images, ensuring that the aperture was large enough to contain as much of the emission from

the galaxy as possible without including any emission from neighbouring objects. Thus the sizes of the optical apertures vary from source to source, although are constant for a given source. I used larger apertures for the IRAC sources due to the images having a larger PSF, but use the procedure outlined below to correct for this.

Due to the difference in the PSF between the optical and IRAC images, as well as the difference in the aperture sizes, a small correction needed to be applied to the IRAC magnitudes before they could be used in conjunction with optical magnitudes to determine a photometric redshift. I corrected IRAC magnitudes by firstly fitting a 2D Gaussian to the IRAC source. I then scaled it to have the FWHM it would have had if observed with CFHT/Subaru. The flux was then computed using the scaled Gaussian and new aperture size. All the corrections applied in this work increase the IRAC magnitudes, and the more extended the source the greater the correction. Corrections range from 0.01 to 0.46 magnitudes.

The new photometry is summarized in table 2.1, and the details of the individual objects are discussed below.

2.2.1 Notes on Individual Objects

AzTEC1- J095942.86+022938.2- AzTEC1 is the brightest submm source in the sample, with fluxes $F_{890\mu m} = 15.6 \pm 1.1$ mJy and $F_{1.1mm} = 10.7 \pm 1.3$ mJy. There is a bright i-band object located directly at the SMA position. Optical fluxes were measured using an aperture 1.94'' in diameter and the source is detected in the Subaru i+ band at 25.11 ± 0.03 mag which is in agreement with the HST i-band magnitude given in Younger et al. (2007). There is some disagreement within

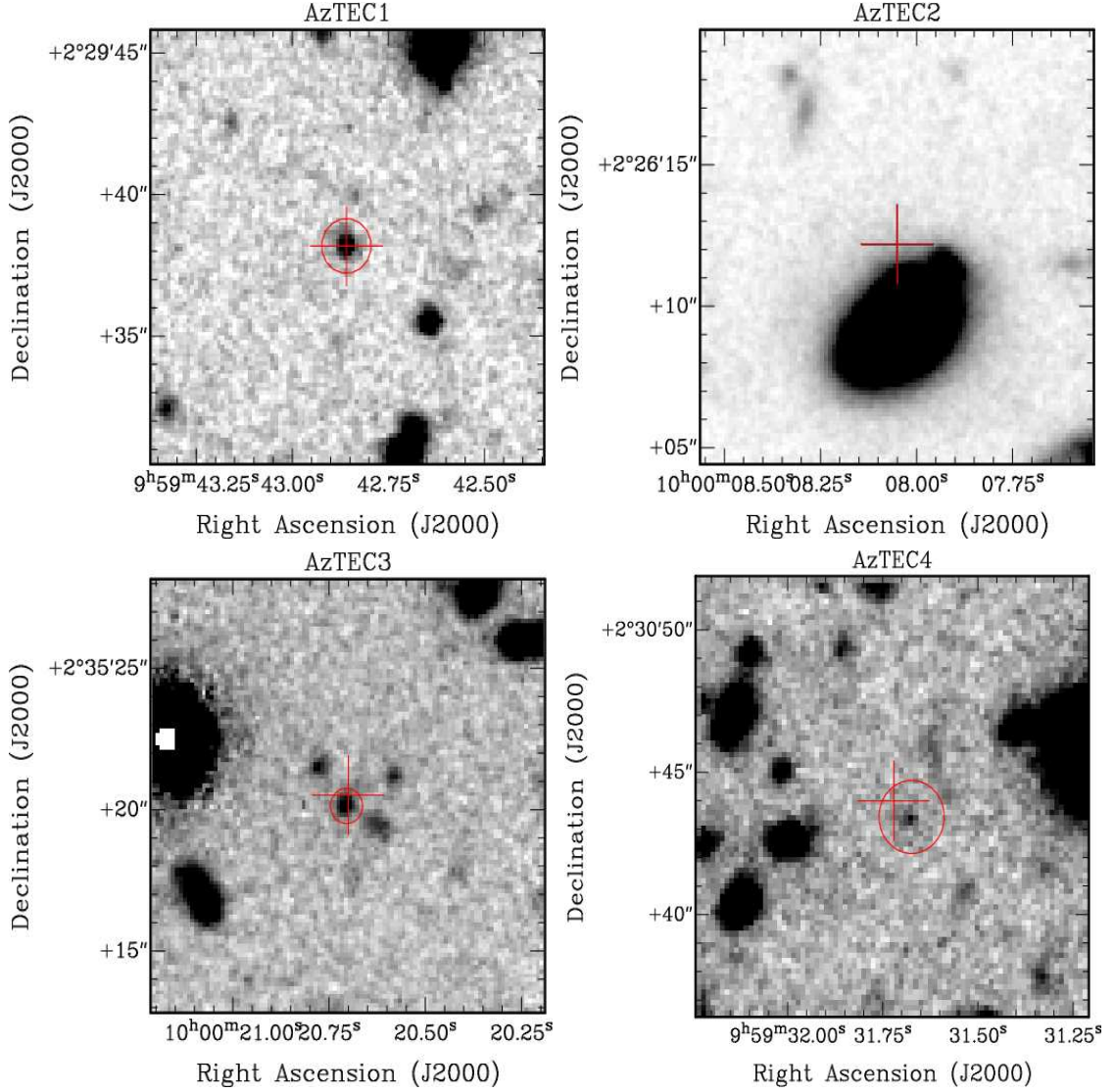


Figure 2.1: Subaru i+ band cutouts for AzTEC1 to 7, with the exception of AzTEC4 and 6, which are the combined CFHT and Subaru i-band images. Each image has a field of view of $15.3'' \times 15.3''$ and a scale of $0.15''/\text{pixel}$. The SMA coordinates of each source are highlighted by cross-hairs and the optical counterpart (including the objects offset from AzTEC4' and 6s SMA coordinates by $\sim 0.8''$ and $\sim 0.6''$ respectively, see text) is circled with an aperture the size of which was used in its photometry. SMA coordinates are accurate to $\sim 0.2''$.

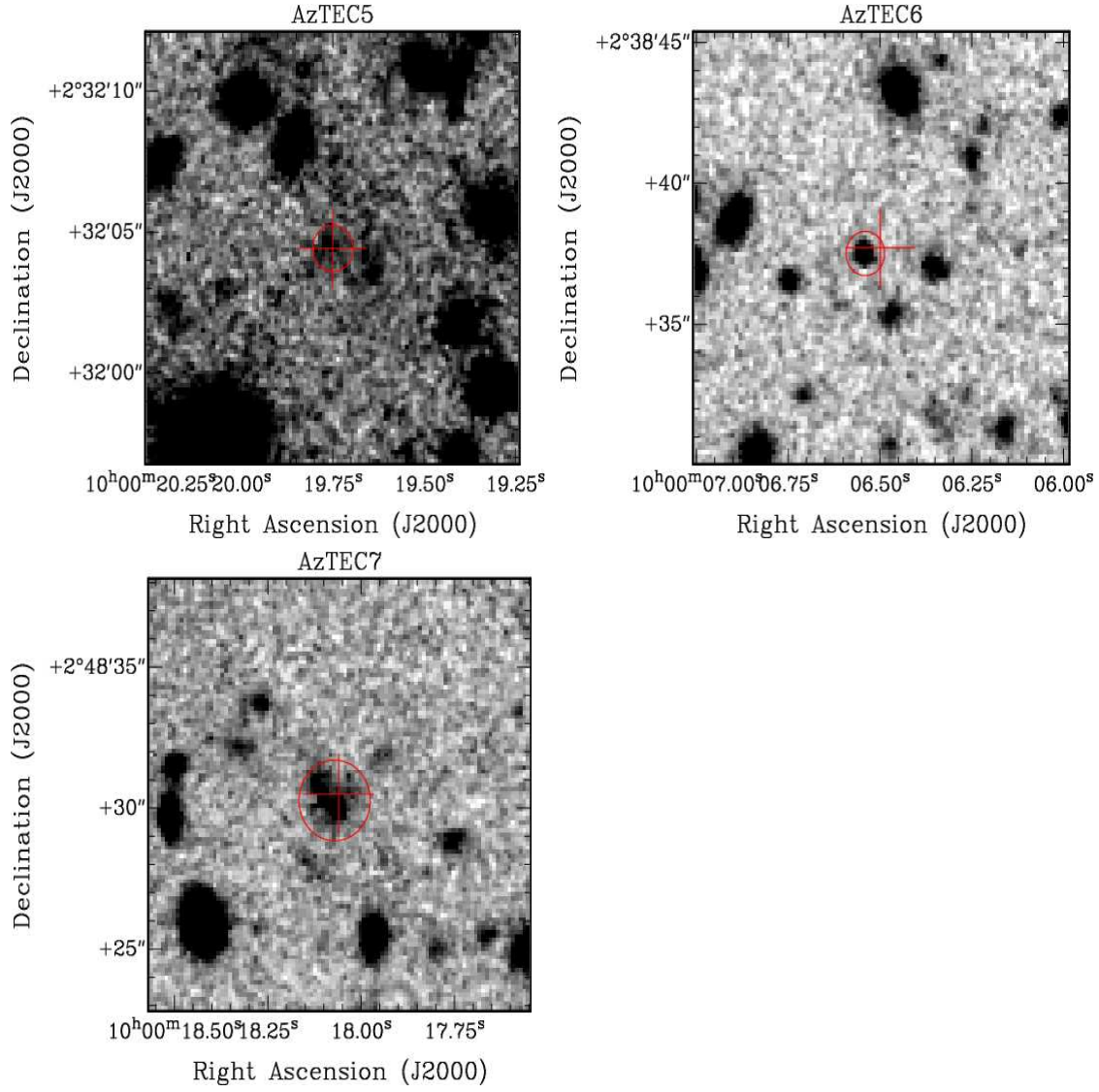


Figure 2.1: *cont.*

the same wavebands between the CFHT and Subaru photometry (table 2.1), but the discrepancy is small enough that the photometric redshift is not significantly affected. IRAC magnitudes were measured using an aperture of diameter $4.45''$. Only a small correction was applied to the IRAC magnitudes; $+0.01$ mag in both IRAC channel 1 and 2.

AzTEC2- *J100008.05+022612.2*- AzTEC2 is detected in the submm with fluxes $F_{890\mu m} = (12.4 \pm 1.0)$ mJy and $F_{1.1mm} = (9.0 \pm 1.3)$ mJy. No objects are found directly at the SMA coordinates, but there is a bright object offset from SMA position by $3''$. Thus the limit on the magnitude of the optical counterpart is not very useful.

AzTEC3- *J100020.70+023520.5*- AzTEC3 is detected in the submm with fluxes $F_{890\mu m} = 8.7 \pm 1.5$ mJy and $F_{1.1mm} = 7.6 \pm 1.2$ mJy. There is a bright i-band object located at the SMA coordinates as well as three companion objects offset by between $1''$ and $2''$. Since SMGs often seem to consist of multiple components (Ivison et al., 1998) it is possible that these companion objects are also part of AzTEC3. However, since six of the seven AzTEC sources are detected in the IRAC bands, it seems likely that if the companion objects are part of the same galaxy then they should also be contributing to the IRAC emission. I attempted to determine whether this is the case by convolving the Subaru image with the IRAC beam and comparing the FWHM of the IRAC source with that of the convolved Subaru image. I find that the FWHM of the convolved image is $\sim 4.4''$. The FWHM of the IRAC $3.6 \mu m$ image is $\sim 2.87''$, suggesting that the $3.6 \mu m$ emission is associated only with the central object. Optical fluxes were measured using a aperture of diameter $1.26''$ and the source is detected in the Subaru i+ band at 26.18 ± 0.08 mag which is in agreement with the HST i-band magnitude.

The CFHT and Subaru magnitudes within the same bands are consistent with each other. IRAC magnitudes were measured using an aperture of diameter $4.80''$. A correction of $+0.2$ mag was applied to the IRAC magnitudes in channels 1 and 2.

AzTEC4- *J095931.72+023044.0* AzTEC4 is detected in the submm with fluxes $F_{890\mu m} = 14.4 \pm 1.9$ mJy and $F_{1.1mm} = 6.8 \pm 1.3$ mJy. I find a tentative i-band counterpart, offset from the SMA position by $0.8''$ ($\sim 4\sigma$), in the Subaru image with a magnitude of 27.43 ± 0.13 . In the combined image (see above), the counterpart can be seen more clearly and has a magnitude of 26.99 ± 0.18 in a $2.57''$ diameter aperture. However I found it is too faint to detect in the other Subaru and CFHT bands. IRAC magnitudes were measured using an aperture of diameter $4.80''$. Corrections of $+0.11$ and $+0.04$ mags were applied to the IRAC magnitudes in channels 1 and 2 respectively. Because of the good agreement between the SMA the optical positions for the other AzTEC sources I tentatively conclude that this is not the true counterpart.

AzTEC5- *J100019.75+023204.4* AzTEC5 is detected in the submm with fluxes $F_{890\mu m} = 9.3 \pm 1.3$ mJy and $F_{1.1mm} = 7.6 \pm 1.3$ mJy. Younger et al. (2007) found no optical counterpart in ACS imaging, but I find a faint Subaru source at the SMA coordinates with a Subaru i+ band magnitude of 26.74 ± 0.13 , measured in an aperture of diameter $1.68''$. The CFHT and Subaru magnitudes within the same bands are consistent with each other. IRAC magnitudes were measured using a aperture of diameter $4.80''$. Corrections of $+0.46$ and $+0.14$ mag were applied to the IRAC magnitudes in channels 1 and 2 respectively.

AzTEC6- *J100006.50+023837.7* AzTEC6 is detected in the submm with fluxes $F_{890\mu m} = 8.6 \pm 1.3$ mJy and $F_{1.1mm} = 7.9 \pm 1.2$ mJy. Younger et al. (2007) find

no optical counterpart in ACS imaging. In CFHT and Subaru imaging I find no source directly at the SMA coordinates, but I do find a source offset from the SMA position by $\sim 0.6''$ ($\sim 3\sigma$). This could therefore be the optical counterpart, or the true counterpart may be too faint to detect. The source offset from the SMA position has a Subaru i+ magnitude of 25.38 ± 0.04 magnitudes, measured in an aperture of diameter $1.59''$. The CFHT and Subaru magnitudes within the same bands are consistent with each other. IRAC magnitudes were measured using an aperture of diameter $5.88''$. A correction of $+0.13$ mag is applied to the IRAC magnitudes in channels 1 and 2. Because of the good agreement between the SMA the optical positions for the other AzTEC sources I tentatively conclude that this is not the true counterpart, although I do estimate a photometric redshift for it.

AzTEC7- *J100018.06+024830.5*- AzTEC7 is detected in the submm with fluxes $F_{890\mu m} = 12.0 \pm 1.5$ mJy and $F_{1.1mm} = 8.3 \pm 1.4$ mJy. I find an optical counterpart with a disturbed morphology at the SMA coordinates which could be a system of merging galaxies. Optical fluxes were measured by placing an aperture of diameter $2.87''$ over the whole of the system. The source is detected in the Subaru i+ band at 24.20 ± 0.04 mag. IRAC magnitudes were measured using an aperture of diameter $6.12''$. Corrections of $+0.08$ and $+0.02$ mag were applied to the IRAC magnitudes in channels 1 and 2 respectively.

	AzTEC1	AzTEC2	AzTEC3	AzTEC4	AzTEC5	AzTEC6	AzTEC 7
RA	09:59:42.86	10:00:08.05	10:00:20.70	09:59:31.72	10:00:19.75	10:00:06.50	10:00:18.06
Dec	+02:29:38.2	+02:26:12.2	+02:35:20.5	+02:30:44.0	+02:32:04.4	+02:38:37.7	+02:48:30.5
Optical Ap. Size	1.94''	...	1.26''	2.57''	1.68''	...(1.59'')	2.87''
m_B	>28.88	...	>29.14	>28.67	28.80±0.47	>28.98(25.80±0.30)	25.67±0.31
m_V	27.13±0.17	...	28.77±0.75	>28.21	28.76±0.62	>28.32(25.67±0.04)	25.10±0.06
m_{r+}	26.21±0.06	...	27.39±0.22	>28.02	27.07±0.13	>28.47(25.77±0.03)	24.97±0.05
m_{i+}	25.11±0.03	...	26.18±0.08	(27.43±0.13)	26.74±0.13	>27.97(25.38±0.04)	24.20±0.04
m_{z+}	25.02±0.02	...	25.58±0.15	>26.50	26.07±0.22	>26.79(24.80±0.06)	23.65±0.07
g_M	>28.12	...	>28.71	>27.93	>28.41	>28.42(26.16±0.05)	N/A
r_M	26.54±0.15	...	27.13±0.24	>27.46	27.15±0.20	>27.96(25.61±0.05)	N/A
i_M	25.25±0.05	...	26.30±0.12	>26.19	26.50±0.13	>27.81(25.42±0.05)	N/A
z_M	25.11±0.13	...	25.69±0.22	>26.27	26.46±0.38	>26.06(24.87±0.08)	N/A
IRAC Ap. Size	4.45''	...	4.80''	4.80''	4.80''	5.88''	6.12''
$m_{3.6\mu m}$	23.40±0.07	...	23.72±0.11	22.11±0.04	23.24±0.08	24.13±0.25	20.63±0.01
$m_{4.5\mu m}$	23.08±0.08	...	22.98±0.12	22.15±0.04	22.31±0.06	23.50±0.27	20.15±0.02

Table 2.1: Photometry for the AzTEC sources, given in AB magnitudes. The first two rows give the SMA co-ordinates. Aperture sizes are the diameters used for measuring optical and IRAC magnitudes. The IRAC magnitudes are corrected to take into account the difference in the seeing and aperture sizes for the IRAC and optical imaging (see text). No optical counterparts are found for AzTEC2. The only nearby optical counterparts for AzTEC4 and 6 are offset from their SMA positions by $\sim 4\sigma$ and $\sim 3\sigma$ respectively. I give the photometry for these objects in parentheses.

2.3 Estimated Redshifts for the AzTEC Sample

Photometric redshifts were determined by applying the photometric redshift package, HYPERZ (Bolzonella et al., 2000), to the 11 band photometry (Subaru:B, V, r+, i+, z+; CFHT: g_M , r_M , i_M , z_M ; IRAC: 3.6 μm , 4.5 μm). The spectra used for fitting in this work are taken from the set compiled by Dye et al. (2008), which is optimized for the determination of photometric redshifts when including filters in the near/mid-infrared. Dye et al. (2008) compared the photometric redshifts determined using these spectral templates with those determined using synthetic spectra constructed from the best-fit star formation history for their sample of 60 SCUBA sources. Since these methods are completely independent and the redshifts found using both sets of templates were found to be in good agreement, I assume that my template set is adequate.

I varied the redshift in the range $z = 0$ to 10. I employed the reddening regime of Calzetti et al. (2000), with A_V allowed to vary in the range $A_V = 0$ to 5 in steps of 0.2. I used a minimum photometric error of 0.05 magnitudes for each band. For wavebands in which I have no detection I took the flux of the source to be zero with a 1σ error equal to the sensitivity of the detector in that waveband. The photometric redshifts obtained are listed in table 2.2.

The median redshift of the sample is 2.7 which is somewhat higher than the median redshift, 2.2, of the sample presented by Chapman et al. (2005). The maximum redshift found is 4.64 and the minimum redshift found is 0.18. Comparing the redshift distribution of this sample to that of the samples presented in Chapman et al. (2005), Pope et al. (2006), Dye et al. (2008) and Clements et al. (2008), I note that only one of the sources in this combined sample of ~ 200 850 μm selected sources is at a comparably high redshift as my two highest redshift sources, although this

ID	z	χ^2_{min}	Notes
AzTEC1	4.64 ± 0.06	1.537	...
AzTEC2	No optical counterpart.
AzTEC3	4.54 ± 0.10	2.196	There is a secondary chi-squared minimum at the lower redshift of $z \sim 0.4$ with a chi-squared fit value of ~ 3.5 .
AzTEC4	Nearest counterpart only detected in one optical band.
AzTEC5	1.49 ± 0.10	1.488	There is a secondary chi-squared minimum at the higher redshift of $z \sim 4$ with a chi-squared fit value of ~ 4 .
AzTEC6	(2.09 ± 0.01)	(6.172)	The redshift and chi-squared values are for the optical source offset from AzTEC6's SMA position. The chi-squared fit to this source is much poorer compared to the others in the sample. This may further imply that the nearby optical counterpart I have selected is not the true counterpart to AzTEC6 and that the IRAC emission is unassociated with the optical emission.
AzTEC7	0.18 ± 0.01	7.021	CFHT data not available. There are several other possible redshifts with chi-squared fit values of ~ 10 up to $z \sim 2$. Even the best chi-squared fit is still relatively poor however, which may be due to the unusual nature of the source.

Table 2.2: The best photometric redshift fits for the AzTEC sources with their minimum reduced χ^2 value, χ^2_{min} . Notes of interest on the photometric redshifts, including secondary fits, for each source are also given. I do not give the best fit SED type, as typically for each source there are several SED types which fit equally well. Note that reduced chi-squared values given here are not those directly output by HYPERZ, which takes the number of degrees of freedom as being the (number of filters−1). This is true if only the redshift is allowed to vary. However, I am additionally allowing A_v , SEDs type and the normalization to vary. Thus the correct number of degrees of freedom is given by (number of filters−4).

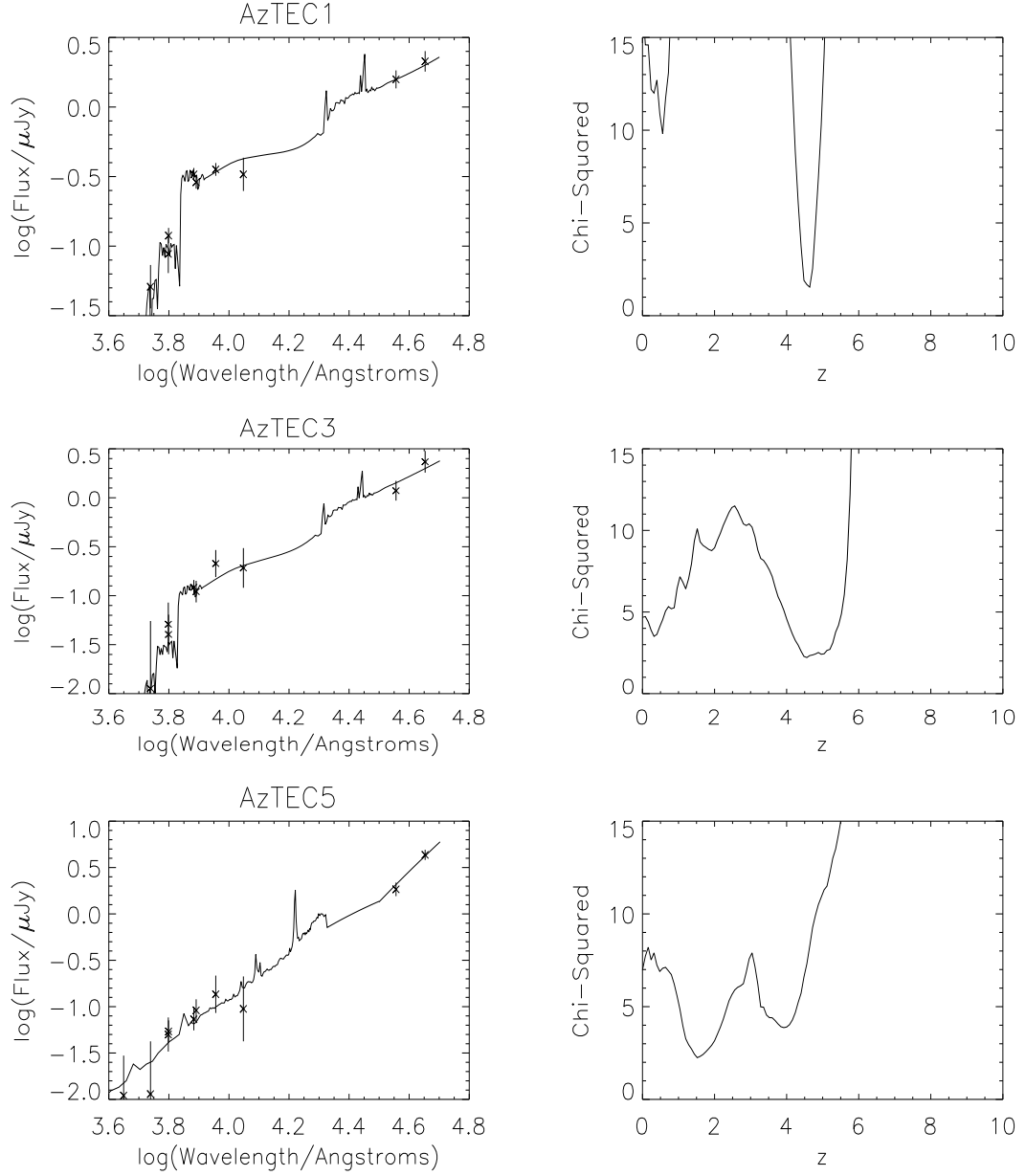


Figure 2.2: The left hand column shows the photometric data points for the AzTEC sources with optical counterparts. The best spectral fits for the sources are overlaid. The right hand column shows the marginalized reduced χ^2 distribution as a function of redshift. The AzTEC6 plots correspond to the nearby optically bright object.

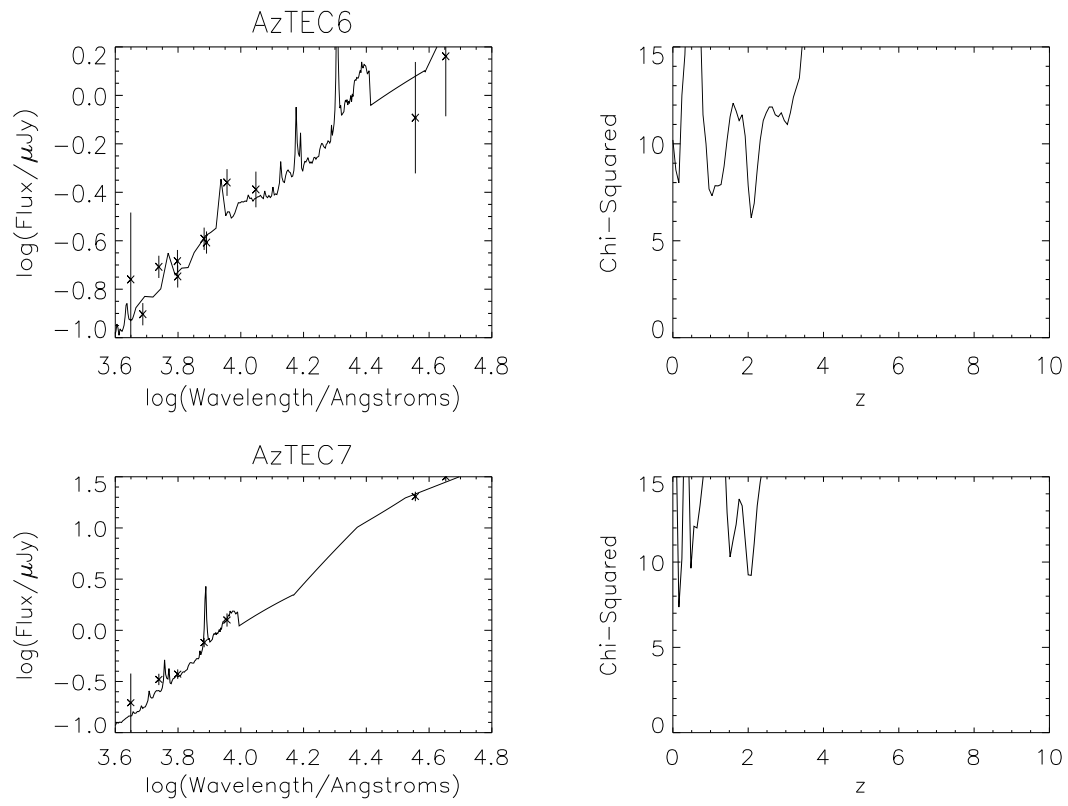


Figure 2.2: *cont.*

difference is not significant when analyzed with a Kolmogorov-Smirnov test. However, two of the other AzTEC sources are undetected to very faint limits in the i-band, and these facts may indicate that 1.1 mm surveys find more sources at very high redshifts than 850 μm surveys.

2.4 A Banded V_e/V_a Analysis

Wall et al. (2008) examined a sample of 38 SMGs in the GOODS-N field and found evidence for a diminution in the space density of SMGs at redshifts $z > 3$. They also found evidence for two separately evolving sub-populations separated by luminosity. In this section I present the results of my re-examination of this result using a banded V_e/V_a analysis and a range of empirical SEDs rather than the theoretical SED used by Wall et al.

The most well known method of investigating the evolution of the space density of galaxies with redshift is the $\langle V/V_{max} \rangle$ test (Schmidt, 1968; Rowan-Robinson, 1968). V is the co-moving volume enclosed by the galaxy (that volume which the field of view traces out in moving from a redshift of $z = 0$ out to the galaxy) and V_{max} is the volume that would be enclosed by the galaxy were it pushed to the redshift at which its flux drops to the survey limit. This method encounters problems when a survey encloses two galaxy populations, one undergoing positive evolution, and the other negative. If we have a uniform distribution of galaxies in space, then we expect the value of $\langle V/V_{max} \rangle$ to be $0.5 \pm (12N)^{-0.5}$, where N is the number of sources in the sample. A value of $\langle V/V_{max} \rangle > 0.5$ then implies a concentration of sources toward the more distant regions of their accessible volume and a value of $\langle V/V_{max} \rangle < 0.5$ implies a deficit of sources at higher redshifts. Therefore if we

have in our sample separate populations undergoing high levels of positive and negative evolution, then $\langle V/V_{max} \rangle$ may still be close to 0.5, incorrectly implying zero evolution.

This problem can be solved by implementing instead a $\langle V_e/V_a \rangle$ test (Dunlop & Peacock, 1990). This is effectively a banded version of the $\langle V/V_{max} \rangle$ test. V_e , the effective volume, is the volume enclosed between a minimum redshift z_{low} and the redshift of the galaxy. V_a , the accessible volume, is the volume enclosed between z_{low} and the redshift at which the galaxy's flux drops below the sensitivity of the survey. By investigating the variation of $\langle V_e/V_a \rangle$ with z_{low} I can distinguish between a positively evolving and a negatively evolving population.

I investigated the evolution of the space density of the sample with redshift through the implementation of a $\langle V_e/V_a \rangle$ test. Wall et al. based the K-correction necessary to calculate accessible volume on a single theoretical SED, whereas real galaxies have a range of SEDs. To investigate this, I carried out the $\langle V_e/V_a \rangle$ analysis using two different assumptions about SEDs. I used the two extreme two-component dust models of Dunne & Eales (2001), who provided fits to the hottest and coldest local SMGs. The cold SED, based on NGC 958, contains dust at temperatures of 20 and 44 K with a cold-to-hot dust mass ratio of 186:1. The hot SED, based on IR1525+36, contains dust at temperatures of 19 and 45 K with a cold-to-hot dust mass ratio of 15:1. Figure 2.3, which shows the predicted flux versus redshift plot for the different models, shows the effect of using different SED templates on the flux-redshift relation. The two SED types are normalized such that they produce a flux of 1 mJy at a redshift of $z = 1$.

I took the limiting flux of each source in the GOODS sample to be 3.5σ and measured $\langle V_e/V_a \rangle$ for $z_{low} = 0$ to 4 in steps of 0.1. I also separated sources into two

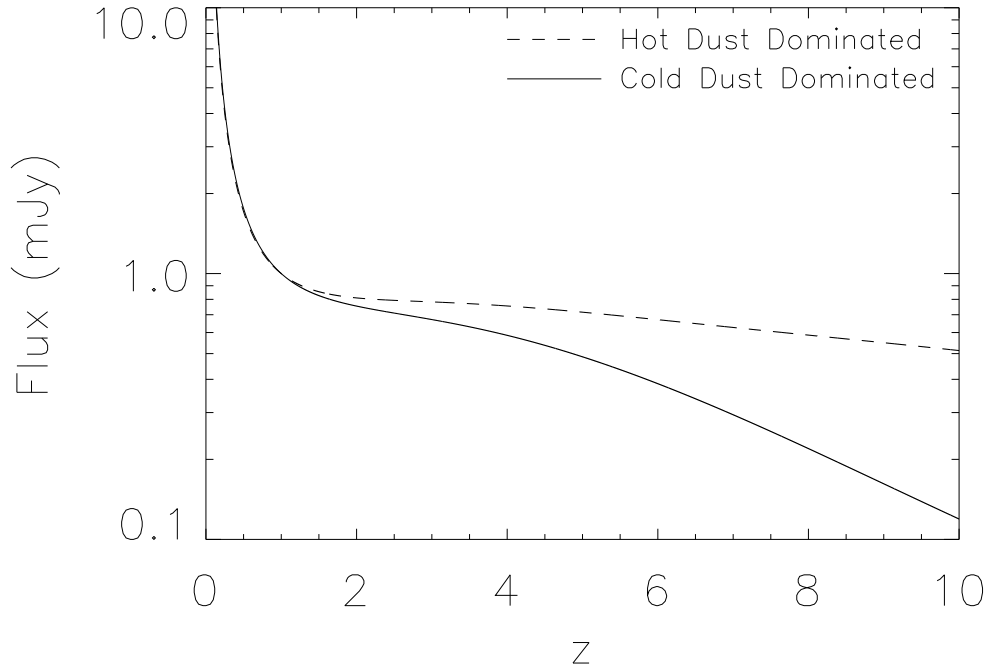


Figure 2.3: Flux versus redshift for both the cold (solid line) and hot (dashed line) SEDs. Both SEDs are normalized such that they produce a flux of 1 mJy at a redshift of $z = 1$.

samples of equal size according to luminosity. In doing this I am able to determine whether there are differences in the evolution of the two sub-populations.

My results for the 38 SMGs of Wall, Pope & Scott are shown in figure 2.4. I find good evidence for the existence of a redshift cutoff at $z > 1$ for the hot SED, and slightly weaker evidence for a redshift cutoff at $z > 2$ for the cold SED. Dividing the sample into separate populations of high and low luminosity sources shows differences in the evolution of the two populations. The low luminosity sources show much sharper redshift cutoffs whereas the evidence for redshift cutoffs in the high luminosity sources is far more marginal. Thus I find evidence to support the conclusions given in Wall et al. (2008): there is a redshift cutoff for the sample and that there is evidence for two separately evolving sub-populations

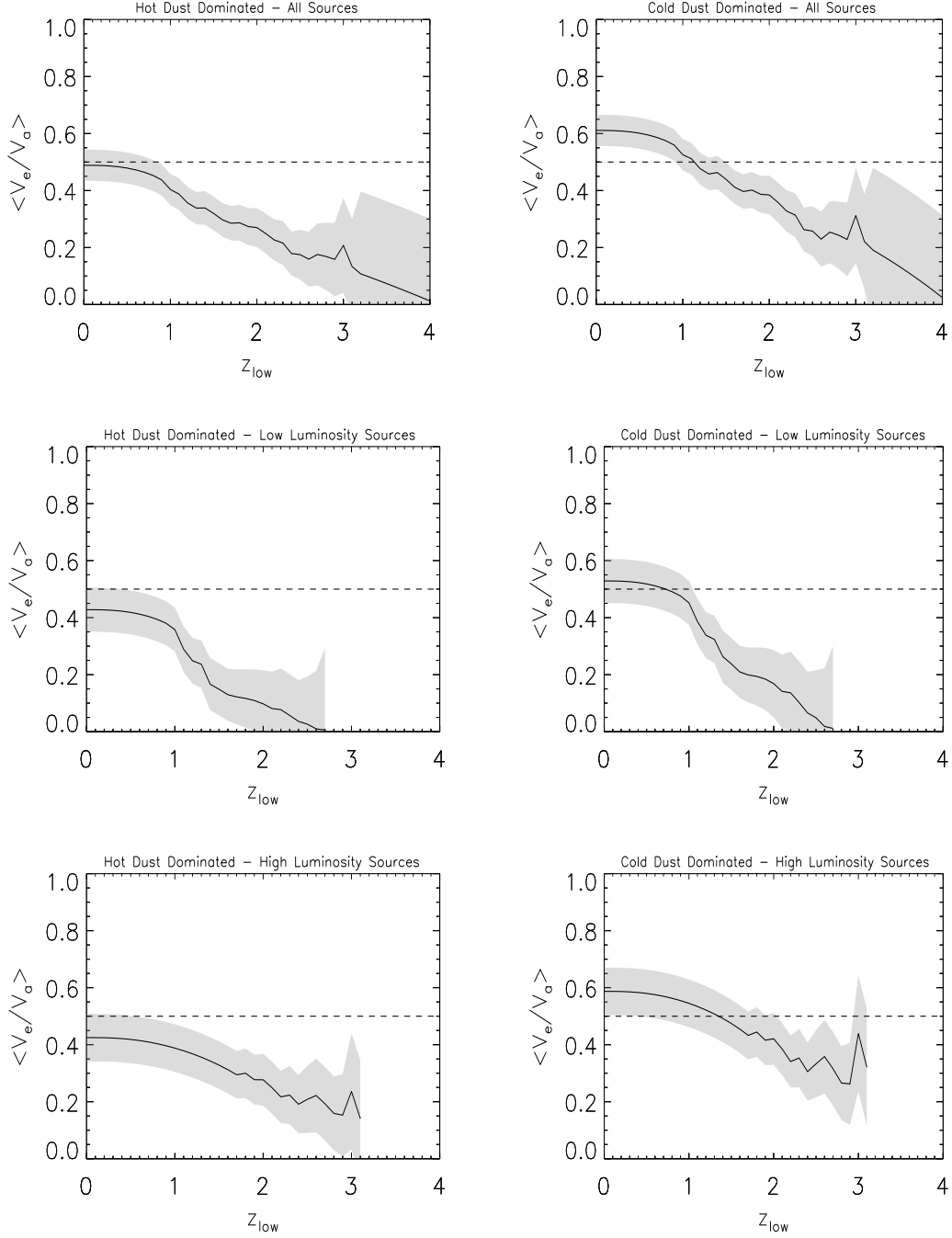


Figure 2.4: The distribution of the values of $\langle V_e/V_a \rangle$ with z_{low} for the GOODS-N sample. Figures in the left hand column are for hot SEDs and figures in the right hand column are for cold SEDs. The sample is also separated into high and low luminosity sources. The dashed line denotes the position of $\langle V_e/V_a \rangle = 0.5$ on the graph, values above which imply a concentration of galaxies at higher redshifts and below which imply a concentration of galaxies at lower redshifts. The grey shaded region shows the area enclosed by the 1σ error.

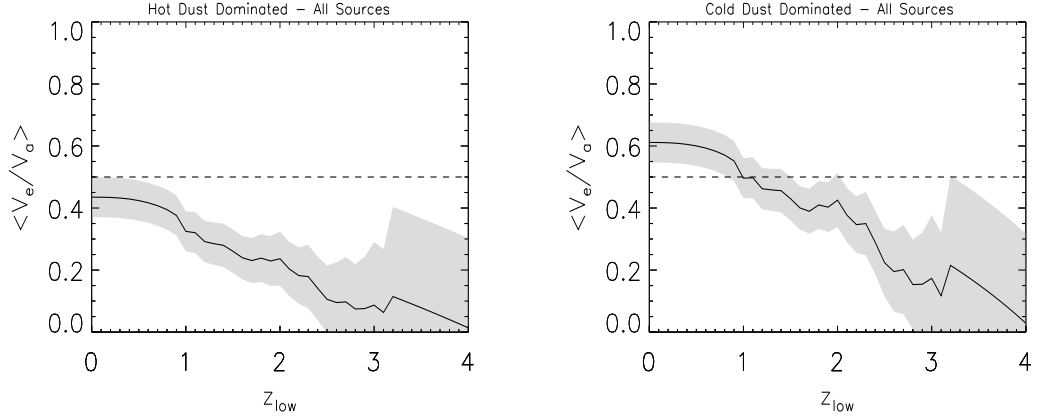


Figure 2.5: The distribution of the values of $\langle V_e/V_a \rangle$ with z_{low} for the GOODS-N sample, using only the sources with reliable identifications. Figures in the left hand column are for hot SEDs and figures in the right hand column are for cold SEDs. The dashed line denotes the position of $\langle V_e/V_a \rangle = 0.5$ on the graph, values above which imply a concentration of galaxies at higher redshifts and below which imply a concentration of galaxies at lower redshifts. The grey shaded region shows the area enclosed by the 1σ error.

An additional uncertainty about this results is that Pope et al. (2006) claim that only 60% of their identifications are reliable. Therefore I also performed the $\langle V_e/V_a \rangle$ analysis only on sources with reliable identifications, the results of which are shown in figure 2.5. Using these sources only, I still find good evidence for a redshift cutoff at $z > 1$ for the hot SED, and some marginal evidence for a cutoff at $z > 2$ for the cold SED. However, I am unable to find any clear evidence for two separately evolving galaxy sub-populations, separated in luminosity, as the sample size is too small.

However, by only taking into account the reliable identifications, I am probably biased towards optically brighter galaxies and therefore lower redshifts. I further investigated the effect of the unreliable identifications by putting four (roughly half) of the unreliable identifications at $z = 4$ and repeating the analysis (figure 2.6). Doing this, I find that for hot SEDs my results are largely unaffected, with a relatively clear cutoff at redshifts higher than $z = 1$. However for the cold

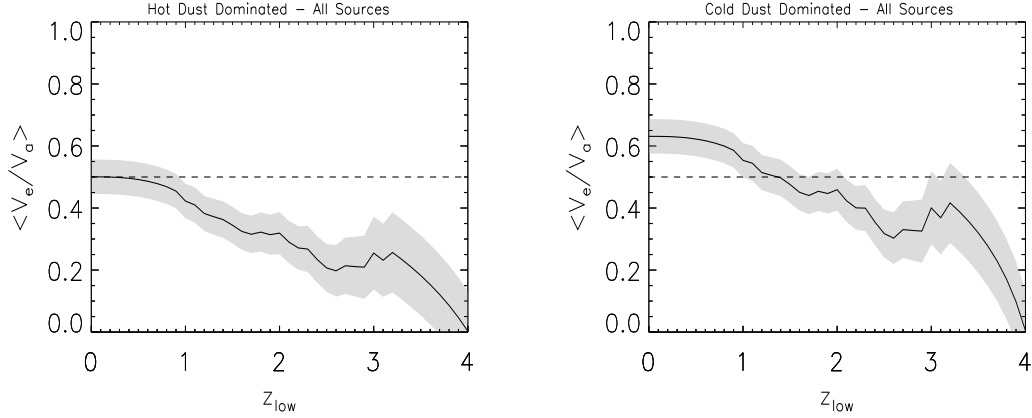


Figure 2.6: The distribution of the values of $\langle V_e/V_a \rangle$ with z_{low} for the GOODS-N sample, where four (roughly half) of the unreliable identifications have been pushed to redshifts of $z = 4$. Figures in the left hand column are for hot SEDs and figures in the right hand column are for cold SEDs. The dashed line denotes the position of $\langle V_e/V_a \rangle = 0.5$ on the graph, values above which imply a concentration of galaxies at higher redshifts and below which imply a concentration of galaxies at lower redshifts. The grey shaded region shows the area enclosed by the 1σ error.

SEDs I find that my results are strongly affected, with no clear redshift cutoff up to a redshift of $z \sim 3$.

I also performed a banded $\langle V_e/V_a \rangle$ analysis on my sample of AzTEC sources (excluding the AzTEC6 counterpart), the results of which are shown in figure 2.7, but my sample is too small to find any clear evidence of a redshift cutoff.

2.5 Conclusions

I gave new Subaru, CFHT and IRAC photometry for a number of sources in the AzTEC / COSMOS survey with accurate coordinates from SMA imaging. I estimated photometric redshifts for four of the seven galaxies in the sample. I found a median redshift of $z_{mean} \sim 2.57$ and a maximum of $z_{max} = 4.50$. Of the sources in the combined $850 \mu\text{m}$ surveys presented in Chapman et al. (2005), Pope

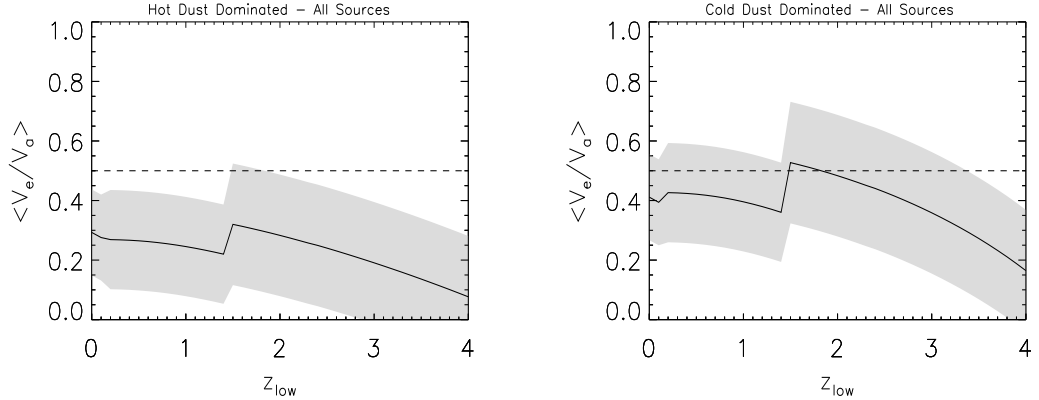


Figure 2.7: The distribution of the values of $\langle V_e/V_a \rangle$ with z_{low} for the AzTEC sample. The panels on the left hand side uses the hot SED and the panels on the right hand side uses the cold SED. The dashed line denotes the position of $\langle V_e/V_a \rangle = 0.5$ on the graph, values above which imply a concentration of galaxies at higher redshifts and below which imply a concentration of galaxies at lower redshifts. The grey shaded region shows the area enclosed by the 1σ error.

et al. (2006), Dye et al. (2008) and Clements et al. (2008), consisting of ~ 200 sources, only one is at a redshift greater than my two highest redshift sources. This in addition to the fact that I am unable to detect two of the sources in the optical bands down to very faint magnitudes may indicate that 1.1 mm surveys are more efficient at detecting very high-redshift sources than $850 \mu\text{m}$ surveys.

It is worth noting that since this work was carried out, Smolčić et al. (2011) have measured a redshift (using multiband photometry Keck DEIMOS spectroscopy) for AzTEC1 of $z = 4.6$, which is very close to the value estimated here.

Re-investigating the space density evolution of a sample of 38 GOODS-N sources (Pope et al., 2006; Wall et al., 2008) with more realistic SEDs I find a redshift cutoff at $z \sim 1$ if I assume a 'hot' SED and marginal evidence for a cutoff at $z \sim 2$ if I assume a 'cold' SED (in reasonable agreement with Wall et al.). Similar to Wall et al. (2008) I also found evidence for two differently evolving sub-populations of SMGs, separated in luminosity, with high luminosity sources showing a less

negative evolution.

I performed a similar test on the AzTEC sources but was unable to draw any reliable conclusions as the sample is too small. The GOODS-N sample is also relatively small, and therefore any evidence for redshift cutoffs and differently evolving sub-populations must be treated with caution. In order to harden the conclusions in general we require larger surveys with accurate redshifts. We would also need surveys taken over larger areas of sky in order to take into account the effects of cosmic variance. Future, larger surveys (e.g. with *Herschel*, SCUBA2) therefore will enable us to more robustly determine the nature of the number density evolution of SMGs in the Universe.

Chapter 3

Morphology Versus Redshift of Herschel Sources in the GOODS-N Field

The photometric redshifts estimated in this chapter have been used by Eales et al. (2010) in an investigation of the 250 μm luminosity function out to $z = 2$.

3.1 Introduction

There is mounting evidence that the cosmic star-formation rate, the average star-formation rate (SFR) per unit comoving volume, has declined by roughly an order of magnitude since $z \sim 1$ (e.g., Lilly et al., 1996; Hogg et al., 1998; Madau et al., 1998; Flores et al., 1999; Haarsma et al., 2000; Hopkins, 2004). This decline in star formation has been linked to the rapid evolution of LIRGs since this epoch (Le

Floc'h et al., 2005). Locally, LIRGs make a negligible contribution to L_{bol} per unit comoving volume; their contribution is comparable to that of normal starbursts at $z \sim 0.7$, and they dominate beyond. In fact LIRGs are the galaxies which exhibit the fastest evolution between $z = 0$ and $z = 1$, with their luminosity per unit comoving volume increasing by a factor of ~ 70 over this time (e.g., Chary & Elbaz, 2001; Le Floc'h et al., 2005).

In the local universe, the majority of LIRGs seem to be powered by major mergers of massive spiral galaxies. Many merging systems appear to be undergoing periods of intense star formation (Barton et al., 2000). Given the observed drop in the merger rate since $z \sim 1$ (e.g., Le Fèvre et al., 2000; Patton et al., 2002; Conselice et al., 2003) it is not unreasonable to postulate that the drop in cosmic SFR since this epoch could be due, at least in part, to this corresponding drop in merger rate.

However, mounting evidence shows that major mergers may not be the main physical process powering LIRGs at redshifts $z \sim 1$. Examination of the optical morphology of LIRGs at these redshifts has found that only a small number, typically $\sim 1/3$, show evidence that they are undergoing some form of merger (e.g., Elbaz et al., 2007; Bell et al., 2005; Zheng et al., 2004; Melbourne et al., 2005). Moreover, as many as half of the LIRGs at these redshifts show optical morphological evidence of being spiral galaxies (e.g., Elbaz et al., 2007; Bell et al., 2005). This in turn suggests that the decline in the rate of major mergers since $z \sim 1$ may not be the main cause of the rapid drop of the cosmic SFR since this era.

There are a number of other physical processes that could be the cause of the drop in the cosmic SFR. Minor mergers have been shown to enhance the SFR of galaxies in the local universe (e.g., Barton et al., 2000). Another likely cause could be the exhaustion of cold gas in galaxies. For example, many massive local

galaxies have low gas fractions ($< 10\%$), (e.g., Kennicutt et al., 1994; Bell & de Jong, 2000) which, given the galaxies' SFRs, will be exhausted within ~ 5 Gyr (e.g., Kennicutt et al., 1994). This implies that higher redshift galaxies could have had higher gas masses than locally, which might explain the decrease in the cosmic SFR. However, this lifetime could be extended with freshly infalling or recycled gas. Other possible processes that might explain the evolution include ram pressure stripping, galaxy harassment during group formation and dynamical instabilities during tidal interaction (Combes, 2005).

In this chapter I present a set SPIRE galaxies, selected at $250\ \mu\text{m}$ and located in the GOODS-N field, and attempt to identify their optical counterparts. I visually inspect their optical counterparts - looking for evidence that a major merger is occurring - and attempt to estimate the relative contribution of lone sources and possible merging systems to the total number of SPIRE sources in the $z < 0.4$, $0.4 < z < 0.8$, $0.8 < z < 1.2$, $1.2 < z < 1.6$, $1.6 < z < 2.0$ and $z > 2.0$ redshift bands.

3.2 Data

GOODS is a *Spitzer* Legacy Program and HST Treasury Program, offering a wealth of data over a wide range of wavelengths. It is made up of two fields, both $10' \times 16'$ in size. The GOODS-N field is centered on the Hubble Deep Field (HDF: $12^h36^m49.4^s, +62^\circ12'58.0''$) and GOODS-S is contained within the Chandra Deep Field South (CDFS: $3^h32^m28.0^s, -27^\circ48'30.0''$).

SPIRE observations have been made over the GOODS-N field. In this section I present SPIRE photometry for 116 $250\ \mu\text{m}$ selected sources, as well as a set of ancil-

lary optical and IR photometry collected by Elbaz (In Prep) (hereafter referred to as EIP). In addition, I take NUV and FUV photometry and spectroscopic redshifts from Barger et al. (2008) (hereafter referred to as B08).

3.2.1 SPIRE Photometry

SPIRE observations at 250 μm , 350 μm and 500 μm were taken over the GOODS-N field down to a 5σ limit of 8.9 mJy at 250 μm . The dominant source of noise in this data is confusion noise, estimated to be 5.8 mJy beam $^{-1}$ at 250 μm (Nguyen et al., 2010). In order to measure robust fluxes for sources near to the confusion limit, a source-extraction method was developed by Roseboom et al. (2010).

The source extraction-technique relies on the assumption that sources detected at 250 μm will also be detected at 24 μm . This assumption is based on recent studies that suggest that sources detected with Spitzer at 24 μm make up the bulk of the far-infrared background (FIRB) emission at 160 μm (Dole et al., 2006), 250, 350 and 500 μm (Marsden et al., 2009). The method of Roseboom et al. (2010) effectively reduces the confusion noise at 250 μm by using the better resolution at 24 μm . The first step in the method is to produce a list of all of the 24 μm sources in the field. A 'matrix inversion' technique is then used to find the 250 μm fluxes at these positions that provide the best fit to the 250 μm image.

The selection of sources detected at $> 5\sigma$ in the 250 μm SPIRE band with 250 μm flux > 10 mJy results in a list of 127 SPIRE sources in the GOODS-N region, 116 of which lie in the region covered by the EIP ancillary photometry. The SPIRE and 24 μm photometry, as well as the nearest IRAC counterpart coordinates for these 116 sources, are shown in table 3.1

Name	RA (IRAC)	DEC (IRAC)	$S_{24\mu m}$	$S_{250\mu m}$	$S_{350\mu m}$	$S_{500\mu m}$
SPIRE1	189.3064185	62.371177	436.0±44.0	13.2±1.8	0.0±4.2	0.0±21.8
SPIRE2	189.3564612	62.3281726	969.0±97.7	23.6±2.5	3.6±1.0	0.0±1.4
SPIRE3	189.3562196	62.3138949	484.0±48.8	10.2±1.4	6.7±1.4	4.2±3.5
SPIRE4	189.2563155	62.3118621	416.0±42.3	15.0±1.7	0.0±.9	0.0±1.1
SPIRE5	189.2200919	62.302129	752.0±75.6	34.0±3.5	11.8±1.7	0.0±1.1
SPIRE6	189.278618	62.2839119	913.0±91.8	12.4±2.3	3.8±6.9	0.0±1.0
SPIRE7	189.1354399	62.283149	718.0±72.9	30.6±3.2	18.7±2.7	5.8±6.1
SPIRE8	189.0936826	62.2623312	725.0±72.8	15.3±2.1	0.0±3.0	0.0±15.8
SPIRE9	189.4205682	62.2547865	239.0±24.5	13.8±1.9	7.8±2.0	0.0±4.5
SPIRE10	189.331859	62.2270467	187.0±19.3	11.3±2.0	0.0±3.1	0.0±1.4
SPIRE11	189.1457143	62.2067186	345.0±35.2	18.0±2.1	8.0±3.5	5.9±24.0
SPIRE12	189.1533826	62.2036468	386.0±38.9	10.9±1.5	11.5±3.7	0.0±42.5
SPIRE13	189.1436266	62.2036037	1310.0±131.3	56.2±5.7	29.4±4.0	10.5±30.5
SPIRE14	189.2745165	62.1982418	665.0±67.2	18.9±2.2	6.9±2.3	0.0±8.6
SPIRE15	189.153692	62.1930192	763.0±76.9	12.9±1.8	6.3±2.3	3.0±83.0
SPIRE16	189.0135593	62.1863635	1250.0±125.4	25.3±2.8	11.1±2.3	0.0±8.3
SPIRE17	189.2130234	62.1752367	1000.0±100.6	20.9±2.3	7.0±1.5	0.0±3.5
SPIRE18	189.2431388	62.1661521	484.0±49.4	12.8±1.6	6.6±1.5	5.5±2.6
SPIRE19	189.2086346	62.133747	226.0±23.7	14.3±2.0	8.9±3.0	2.4±11.1
SPIRE20	189.1082482	62.1153397	220.0±23.0	10.4±1.3	3.3±1.7	10.1±5.9

Table 3.1: The SPIRE 250 μm , 350 μm and 500 μm fluxes ($S_{250\mu m}$, $S_{350\mu m}$ and $S_{500\mu m}$ respectively) for of each of the 116 SPIRE sources in the region covered by the EIP ancillary photometry. The 24 μm flux and nearest IRAC counterpart coordinates of each source's 24 μm counterpart are also given. All fluxes are measured in mJy.

Name	RA (IRAC)	DEC (IRAC)	$S_{24\mu m}$	$S_{250\mu m}$	$S_{350\mu m}$	$S_{500\mu m}$
SPIRE21	189.2994986	62.3700396	65.5 \pm 7.9	15.4 \pm 2.1	43.7 \pm 10.3	11.1 \pm 39.5
SPIRE22	189.317085	62.354114	322.0 \pm 32.5	11.0 \pm 1.5	8.5 \pm 4.1	4.1 \pm 6.2
SPIRE23	189.3438506	62.3106001	241.0 \pm 24.7	11.4 \pm 1.5	8.4 \pm 1.5	2.7 \pm 1.4
SPIRE24	189.2708892	62.2907828	65.6 \pm 8.1	10.6 \pm 2.0	1.0 \pm 2.9	0.0 \pm 1.0
SPIRE25	189.3938243	62.2897977	741.0 \pm 74.4	35.4 \pm 3.7	17.0 \pm 3.1	14.0 \pm 11.5
SPIRE26	189.3798383	62.2722947	622.0 \pm 62.6	18.4 \pm 2.1	11.0 \pm 1.7	6.0 \pm 1.4
SPIRE27	189.3689794	62.2396965	230.0 \pm 24.3	15.0 \pm 2.2	16.8 \pm 4.5	15.8 \pm 17.8
SPIRE28	189.1619652	62.2159014	236.0 \pm 24.1	15.3 \pm 1.9	9.3 \pm 2.6	8.7 \pm 12.4
SPIRE29	189.1663945	62.213871	511.0 \pm 51.6	11.1 \pm 1.7	7.7 \pm 3.3	0.0 \pm 35.7
SPIRE30	189.136518	62.2121934	121.0 \pm 14.1	12.0 \pm 1.7	3.5 \pm 2.7	0.0 \pm 11.5
SPIRE31	189.3002105	62.2033231	40.0 \pm 6.8	10.4 \pm 1.5	9.4 \pm 2.3	7.4 \pm 19.2
SPIRE32	189.2458566	62.2024658	273.0 \pm 28.1	10.9 \pm 1.4	7.1 \pm 1.3	0.0 \pm 3.4
SPIRE33	189.0242911	62.1966726	171.0 \pm 17.8	12.6 \pm 1.6	12.6 \pm 2.5	.9 \pm 18.0
SPIRE34	189.1213065	62.1794346	730.0 \pm 74.1	32.6 \pm 3.4	27.0 \pm 3.1	16.8 \pm 8.8
SPIRE35	188.9638432	62.1777637	30.4 \pm 5.7	11.1 \pm 1.8	3.3 \pm 5.1	.4 \pm 31.2
SPIRE36	189.0479349	62.17602	293.0 \pm 29.7	11.6 \pm 1.5	11.6 \pm 2.0	8.8 \pm 11.9
SPIRE37	188.9900926	62.1734304	110.0 \pm 12.3	11.4 \pm 1.5	13.6 \pm 2.3	12.5 \pm 15.4
SPIRE38	189.0797115	62.167884	219.0 \pm 23.0	10.0 \pm 1.6	12.7 \pm 2.9	5.9 \pm 21.9
SPIRE39	189.1302972	62.1660685	207.0 \pm 21.8	28.2 \pm 3.0	25.4 \pm 2.8	15.1 \pm 8.0
SPIRE40	189.1774028	62.1594473	481.0 \pm 48.6	15.0 \pm 2.3	2.5 \pm 6.8	0.0 \pm 29.5

Table 3.1: *cont.*

Name	RA (IRAC)	DEC (IRAC)	$S_{24\mu m}$	$S_{250\mu m}$	$S_{350\mu m}$	$S_{500\mu m}$
SPIRE41	189.1542805	62.1478793	371.0±37.9	16.0±1.9	17.4±2.5	16.6±7.7
SPIRE42	189.2233698	62.1472838	133.0±14.4	10.6±1.6	11.5±2.5	12.3±11.2
SPIRE43	189.1106261	62.1431663	139.0±15.3	14.1±1.8	12.9±3.1	5.2±19.7
SPIRE44	189.2330801	62.1356151	859.0±86.6	33.0±3.6	22.1±3.3	18.5±12.4
SPIRE45	189.1324759	62.1121078	347.0±36.1	18.3±2.0	20.4±2.4	18.7±4.4
SPIRE46	189.1436872	62.1077989	108.0±13.9	15.7±1.8	18.8±2.1	14.4±2.3
SPIRE47	189.3514397	62.3660174	399.0±40.6	12.2±1.5	0.0±.9	0.0±1.6
SPIRE48	189.4387472	62.3469994	36.4±6.3	13.3±1.7	14.0±2.2	11.1±5.1
SPIRE49	189.3995936	62.3452635	176.0±18.4	15.1±2.0	13.6±2.5	6.0±3.5
SPIRE50	189.5203313	62.3041802	230.0±23.7	11.1±1.5	7.0±1.6	0.0±1.0
SPIRE51	189.0874127	62.2859984	355.0±36.5	28.8±3.1	28.2±3.2	15.8±8.0
SPIRE52	189.4282547	62.2659032	312.0±31.8	11.0±1.4	16.6±1.9	9.3±3.5
SPIRE53	189.0187141	62.2643943	112.0±12.8	10.5±1.8	10.4±3.8	0.0±8.9
SPIRE54	188.9988616	62.2638386	1510.0±151.8	34.7±3.6	11.7±1.9	2.6±5.9
SPIRE55	188.9704727	62.2279918	217.0±23.1	15.2±2.2	23.0±4.4	22.9±11.8
SPIRE56	189.4043985	62.2013608	763.0±76.7	23.8±2.7	13.5±3.1	3.2±23.1
SPIRE57	189.3806849	62.1979585	332.0±33.9	14.3±1.6	10.9±1.5	7.7±4.4
SPIRE58	189.3674617	62.1901188	85.2±10.3	11.4±1.5	6.2±.9	1.6±7.1
SPIRE59	189.3405606	62.1789524	230.0±23.8	11.9±2.4	6.4±8.7	7.9±55.5
SPIRE60	189.3653786	62.176653	869.0±88.2	30.7±3.3	13.4±2.3	2.7±9.3

Table 3.1: *cont.*

Name	RA (IRAC)	DEC (IRAC)	$S_{24\mu m}$	$S_{250\mu m}$	$S_{350\mu m}$	$S_{500\mu m}$
SPIRE61	188.974446	62.2270318	553.0±56.8	23.0±3.1	9.8±4.1	0.0±14.5
SPIRE62	189.0510176	62.1452089	47.3±7.1	15.0±1.8	23.6±2.8	14.0±5.7
SPIRE63	189.1451345	62.119483	380.0±39.9	20.7±2.3	20.5±2.5	6.9±3.7
SPIRE64	189.1452503	62.2745124	510.0±51.5	11.3±1.5	4.9±1.8	4.6±2.1
SPIRE65	189.1521215	62.2280044	101.0±11.1	18.4±2.0	13.6±1.8	1.8±5.4
SPIRE66	189.1758564	62.2626177	866.0±87.2	17.0±1.9	12.3±1.7	0.0±1.1
SPIRE67	189.1897385	62.140317	236.0±25.1	12.5±1.7	4.3±2.1	0.0±8.5
SPIRE68	189.2146227	62.1121744	582.0±59.3	20.4±2.5	11.4±4.1	0.0±1.1
SPIRE69	189.2408083	62.2486088	373.0±38.1	14.0±1.9	7.6±2.3	16.4±5.8
SPIRE70	189.2614148	62.2337629	349.0±36.0	18.9±2.1	17.1±2.1	13.0±2.6
SPIRE71	189.3553978	62.1683453	683.0±68.8	24.9±2.7	13.9±2.3	.3±1.2
SPIRE72	189.3824909	62.2176008	250.0±25.6	13.4±2.0	9.9±3.4	21.0±26.7
SPIRE73	189.4152532	62.2091394	136.0±15.5	13.6±2.6	0.0±6.3	18.9±96.7
SPIRE74	189.4224207	62.2142218	385.0±39.2	26.1±2.8	20.6±3.0	12.1±12.4
SPIRE75	189.2942674	62.3762704	386.0±38.9	23.6±2.6	12.6±2.4	0.0±9.9
SPIRE76	189.292339	62.3685205	125.0±13.1	17.0±2.4	0.0±13.5	55.7±57.7
SPIRE77	189.2865478	62.3671758	20.2±4.0	11.3±1.6	20.3±5.1	0.0±28.0
SPIRE78	189.2552308	62.3516852	272.0±27.8	15.6±1.8	13.9±2.4	9.9±6.5
SPIRE79	189.2717422	62.3307925	483.0±48.8	18.1±2.0	1.6±.8	0.0±1.0
SPIRE80	189.1689753	62.3091483	32.7±6.6	11.7±1.5	11.0±1.5	0.0±1.0

Table 3.1: *cont.*

Name	RA (IRAC)	DEC (IRAC)	$S_{24\mu m}$	$S_{250\mu m}$	$S_{350\mu m}$	$S_{500\mu m}$
SPIRE81	189.445161	62.2953985	32.5±6.3	18.6±2.3	17.7±2.7	2.3±3.7
SPIRE82	189.3191012	62.2787154	508.0±51.2	18.6±2.1	11.8±1.8	5.1±2.5
SPIRE83	189.5308778	62.2726499	141.0±14.9	10.2±1.8	6.6±3.5	9.7±8.7
SPIRE84	188.9979521	62.2600304	141.0±16.2	12.6±2.0	1.6±2.2	0.0±8.8
SPIRE85	189.0722302	62.2582017	502.0±50.8	11.3±1.4	4.4±1.4	9.1±5.6
SPIRE86	189.0670817	62.2537872	326.0±33.6	27.6±2.9	26.4±3.0	9.3±4.6
SPIRE87	189.4821954	62.2518585	683.0±70.2	36.0±3.7	11.3±1.4	0.0±1.1
SPIRE88	189.4131632	62.2485215	373.0±37.5	11.2±1.4	13.3±1.8	6.8±2.5
SPIRE89	189.3659297	62.2436217	338.0±34.4	11.4±1.6	7.7±1.8	6.5±5.2
SPIRE90	189.3709333	62.2416469	91.3±10.5	14.5±2.3	13.3±4.1	1.7±14.2
SPIRE91	189.074069	62.2355019	429.0±43.5	13.5±2.1	16.2±3.1	0.0±1.0
SPIRE92	189.3781214	62.2162335	181.0±19.2	48.7±5.1	52.8±5.7	36.1±11.0
SPIRE93	189.0813149	62.2145657	971.0±97.7	30.0±3.3	17.0±3.5	0.0±1.1
SPIRE94	189.18328	62.2138893	434.0±43.8	11.2±1.7	3.6±2.4	4.2±12.8
SPIRE95	189.1438075	62.2113877	444.0±44.7	63.0±6.4	50.3±5.7	23.0±14.6
SPIRE96	189.30956	62.2023589	225.0±24.5	13.4±2.0	16.7±3.7	24.8±41.1
SPIRE97	189.0367125	62.1954558	273.0±28.0	28.5±3.0	21.7±2.8	23.7±9.5
SPIRE98	189.222393	62.1943448	336.0±34.4	20.9±2.3	12.6±1.8	1.4±6.5
SPIRE99	189.1694277	62.1932317	105.0±11.3	11.2±2.2	5.7±4.3	9.0±40.4
SPIRE100	189.1724094	62.1915337	320.0±33.1	11.5±1.8	9.3±2.6	2.5±18.3

Table 3.1: *cont.*

Name	RA (IRAC)	DEC (IRAC)	$S_{24\mu m}$	$S_{250\mu m}$	$S_{350\mu m}$	$S_{500\mu m}$
SPIRE101	189.2217444	62.1879865	363.0 \pm 37.0	12.6 \pm 1.9	16.0 \pm 3.8	9.0 \pm 39.6
SPIRE102	189.1310966	62.1871655	480.0 \pm 48.4	16.2 \pm 2.0	11.1 \pm 2.5	2.2 \pm 2.6
SPIRE103	188.9469755	62.1808828	84.2 \pm 11.0	10.7 \pm 2.0	9.2 \pm 3.5	5.2 \pm 15.3
SPIRE104	189.1403248	62.1683198	581.0 \pm 58.8	20.3 \pm 2.2	14.3 \pm 1.8	6.9 \pm 6.5
SPIRE105	188.9712164	62.1651232	241.0 \pm 24.7	11.7 \pm 1.5	12.9 \pm 2.4	0.0 \pm 13.2
SPIRE106	189.0273787	62.1643276	499.0 \pm 50.6	30.7 \pm 3.4	20.3 \pm 4.4	5.2 \pm 36.5
SPIRE107	189.2092214	62.1457043	596.0 \pm 60.3	15.7 \pm 1.9	6.2 \pm 1.6	5.3 \pm 7.1
SPIRE108	189.1384373	62.1429788	779.0 \pm 78.3	22.4 \pm 2.5	19.2 \pm 2.6	6.4 \pm 9.7
SPIRE109	189.2278054	62.1344974	269.0 \pm 27.5	19.1 \pm 2.3	14.5 \pm 2.7	.8 \pm 8.8
SPIRE110	189.190949	62.1317286	374.0 \pm 38.2	18.0 \pm 2.0	11.4 \pm 1.7	4.6 \pm 6.1
SPIRE111	189.151538	62.1185885	594.0 \pm 61.6	28.2 \pm 3.0	20.1 \pm 2.5	16.3 \pm 4.5
SPIRE112	189.1205614	62.1044603	342.0 \pm 35.4	19.2 \pm 2.1	26.3 \pm 2.9	25.8 \pm 4.7
SPIRE113	189.2566069	62.1961931	739.0 \pm 74.7	41.4 \pm 4.3	41.5 \pm 4.5	25.6 \pm 8.9
SPIRE114	189.326116	62.1925457	107.0 \pm 12.1	18.3 \pm 2.6	12.3 \pm 4.0	7.4 \pm 40.9
SPIRE115	189.0308352	62.1480791	68.1 \pm 9.1	14.0 \pm 1.9	18.6 \pm 3.2	20.7 \pm 13.4
SPIRE116	189.4226556	62.3177359	296.0 \pm 30.6	16.7 \pm 2.3	11.6 \pm 3.3	0.0 \pm 1.0

Table 3.1: *cont.*

3.2.2 Identifying Optical Counterparts

The identification of optical counterparts is complicated by the low resolution of IR observations compared to that of optical observations. However, the positional accuracy of the SPIRE sources is greatly increased by having associated $24\ \mu\text{m}$ counterparts. This accuracy is then high enough that it is possible to make XIDs with IRAC counterparts, endowing yet higher positional accuracy. From this, the coordinates of the SPIRE sources are known to high enough resolution that optical counterparts can be identified. IRAC observations, however, still have much lower resolution than optical observations, which means that in many cases there may be more than one optical source contributing to the IRAC flux.

In cases where there are multiple optical counterparts, there are two possible explanations :

1 - The sources are simply coincident on the sky by chance. The probability of this occurring can be calculated from number counts of the optical sources in the region. If there is a high probability of this, then I cannot determine which is the true optical counterpart. This makes it impossible to be sure which is producing the SPIRE emission, although one could use the properties of the two galaxies (optical mag and colour etc.) to infer which is the true counterpart.

2 - The optical counterpart is a merging system. Evidence for a major merger can be seen through direct visual examination of the optical imaging - looking for tidal interactions or a disturbed morphology. If the optical counterpart of the SPIRE source is a merging system, then if a spectroscopic redshift exists for one of the component optical galaxies, then this is also the redshift of the SPIRE source. However, if no spectroscopic redshift exists, it is hard to estimate a photometric

redshift, as the system contains multiple components which might have different spectral energy distributions.

In order to identify the optical counterparts for our SPIRE sources I overlaid the $3.5\ \mu\text{m}$ flux contours over HST/ACS F850LP images to attempt to determine whether there may be more than one optical source contributing to the IRAC flux. The ACS F850LP band was chosen as this corresponds roughly to the rest frame B-band for galaxies at $z \sim 1$. This method is illustrated in figure 3.1.

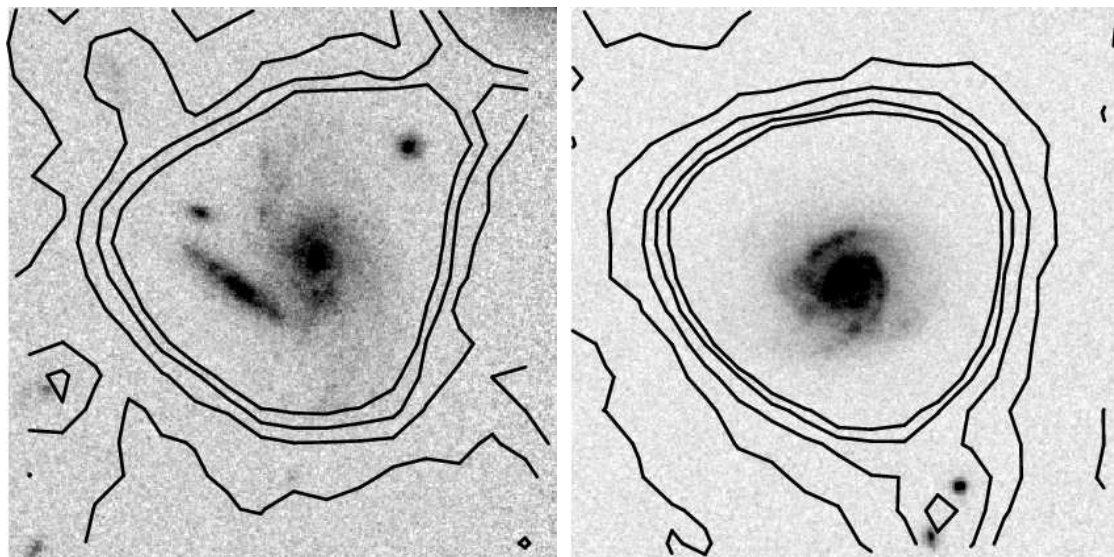


Figure 3.1: HST/ACS F850LP band photometry overlain with IRAC $3.5\ \mu\text{m}$ flux contours. The left panel shows an example of an IRAC source where there may be multiple optical counterparts contributing to the flux. The right panel shows an example where we can only see one optical source coincident with the IRAC flux.

Of the 116 SPIRE sources I find 78 where there appears to be a single contributing optical galaxy, and 38 where more than one optical galaxy is coincident with the IRAC emission. The possibility of these being genuine mergers will be discussed in section 5.4. Of the 78 single optical counterparts, there is one whose IRAC flux is heavily confused with that of a nearby bright object. No further conclusions can be drawn about the photometry of this source, as its IR flux cannot be reliably measured. Therefore the sample of SPIRE sources with single optical counterparts

drops to 77.

3.2.3 Ancillary Data

Ancillary data for this region has been compiled by EIP: KPNO/MOSAIC U band; HST/ACS F435W, F606W, F775W and F850LP; SUBARU/MOIRCS JK bands; Spitzer IRAC 3.5 μm , 4.5 μm , 5.8 μm and 8.0 μm ; Spitzer MIPS 24 μm . Fluxes were measured by EIP for the “full” galaxies, hence no aperture correction was applied. The final catalogue consists of 2792 sources, detected at 24 μm at $> 3\sigma$.

B08 compiled the most spectroscopically complete redshift catalogue to date for the GOODS-N field, comprising of 2097 galaxies with $K < 24.5$ and $F850LP < 26$. In addition to their spectroscopic catalog, B08 also measured NUV and FUV photometry from a deep 150 ks GALEX mission exposure of the ACS GOODS-N region. However, given the large PSF of GALEX, any source within 8” of any other bright GALEX source at the same wavelength was eliminated. The final sample contains 1016 sources with $NUV < 25$ and 478 sources with $FUV < 25.5$.

I searched for optical counterparts using the Elbaz catalogue ACS coordinates, within 1” of the IRAC positions. Doing this, I found an optical counterpart in the Elbaz catalog for 74 of the 77 single optical SPIRE counterparts. Of these 74 sources 46 have counterparts in the B08 spectroscopic redshift catalogue. In addition 20 sources have a counterpart in the B08 GALEX photometry catalog.

Of the 38 SPIRE sources where the counterpart may be a merging system, 28 have an associated spectroscopic redshift from the B08 catalogue.

The collected photometry from EIP for the SPIRE sources with a single optical

counterpart is shown in table 3.2.

3.3 Estimating Photometric Redshifts

I first estimated photometric redshifts for all of the 1057 sources in the Elbaz catalogue which have a counterparts in the B08 spectroscopic catalogue. By comparing the spectroscopic and photometric redshifts it is possible to determine the reliability of the photometric redshift estimates. There still remains the issue for each of these sources that they have not been filtered to determine whether there may be more than one optical source contributing to the IRAC flux. However, as I am only using these sources to gain a very rough estimate of the reliability of the photometric redshift estimates, I do not take this into account. In addition, the majority of these galaxies are not SPIRE galaxies - therefore we expect far fewer mergers and therefore fewer cases of multiple optical galaxies being coincident with an IRAC source.

Photometric redshifts were estimated using the HYPERZ photometric redshift package (Bolzonella et al., 2000), using the NUV, FUV, U, F435W, F606W, F775W, F850LP, J, K, 3.5 μm and 4.5 μm to magnitude limits of 28.0, 25.0, 28.7, 33.2, 29.3, 27.4, 27.0, 27.3, 22.8, 22.0 and 21.9 respectively. I allowed the redshift to vary in the range 0 - 6 in steps of 0.05. Employing the reddening regime of Calzetti et al. (2000), I also allowed A_V to vary in the range 0 - 5 in steps of 0.1. For wavebands in which there is no detection I took the flux of the source to be zero with a 1σ error equal to the limiting flux of the observations in that waveband.

The results of this are shown in figure 3.2, which plots the estimated photometric redshifts against the spectroscopic redshifts from B08. There are a number of

Name	FUV	NUV	U	F435W	F606W	F775W	F850LP	J	K	3.6 μ m	4.5 μ m	5.8 μ m	8 μ m	24 μ m
SPIRE1	26.75	24.15	23.77	23.99	23.15	22.16	21.62	20.68	19.81	19.65	19.94	20.08	20.13	17.32
SPIRE2	21.25	20.49	20.04	19.67	18.73	18.33	18.14	17.69	17.28	18.50	18.51	18.89	17.36	16.36
SPIRE3	-28.19	23.98	23.27	23.02	22.11	20.99	20.59	19.81	19.13	19.14	19.55	19.55	19.85	17.19
SPIRE4	21.90	21.24	20.26	20.14	18.94	18.41	18.15	17.42	17.02	18.52	18.71	19.14	17.97	17.37
SPIRE5	24.63	23.68	22.06	21.58	20.08	19.36	19.04	18.24	17.52	18.47	18.46	18.73	16.91	16.71
SPIRE6	20.65	19.89	20.03	20.09	19.84	19.88	19.86	19.30	18.98	18.39	18.19	17.90	17.61	16.50
SPIRE7	23.32	21.80	21.13	20.64	19.54	18.90	18.61	18.06	17.50	18.51	18.65	18.90	18.12	16.65
SPIRE8	25.52	23.05	22.49	22.07	21.19	20.41	20.18	19.53	19.03	19.30	19.68	19.47	19.25	16.76
SPIRE9	22.89	22.06	21.32	21.08	19.69	18.95	18.62	17.80	17.21	18.51	18.72	19.10	18.89	17.95
SPIRE10	26.96	24.66	23.87	23.09	21.57	20.61	20.19	19.47	18.56	19.14	19.38	19.59	19.28	18.23
SPIRE11	25.42	23.61	22.85	22.22	20.75	19.71	19.29	18.67	17.83	18.28	18.64	18.69	19.03	17.54
SPIRE12	-27.42	23.85	22.94	22.58	21.77	20.60	20.14	19.49	18.69	18.78	19.18	19.31	19.70	17.45
SPIRE13	24.62	22.98	22.02	21.45	19.96	19.15	18.80	18.13	17.31	17.86	18.09	18.19	17.56	16.12
SPIRE14	27.93	24.55	23.29	22.90	22.07	21.03	20.61	19.84	19.19	19.08	19.46	19.51	19.72	16.87
SPIRE15	20.37	20.06	19.57	18.87	18.37	18.07	17.99	17.66	17.58	18.83	19.21	19.08	17.32	16.70
SPIRE16	25.39	23.49	22.87	22.38	21.22	20.30	20.00	19.33	18.51	18.58	18.97	18.76	18.80	16.18
SPIRE17	25.60	24.92	23.56	22.71	21.17	20.36	19.94	19.28	18.47	18.96	18.91	19.10	17.74	16.44
SPIRE18	21.23	20.82	19.96	19.21	18.23	17.74	17.54	17.00	16.77	18.00	18.36	18.62	17.12	17.05
SPIRE19	26.17	24.48	24.09	23.51	22.40	21.65	21.41	20.75	19.97	20.08	20.32	20.11	19.79	18.04
SPIRE20	25.68	23.42	23.00	22.45	21.41	20.48	20.16	19.42	18.82	19.17	19.61	19.60	19.94	18.02

Table 3.2: The collected EIP ancillary photometry for the 74 SPIRE sources with a single optical counterpart. Also included are the GALEX NUV and FUV magnitudes from B08. Coordinates given are ACS coordinates. All magnitudes are AB.

Name	FUV	NUV	U	F435W	F606W	F775W	F850LP	J	K	3.6 μ m	4.5 μ m	5.8 μ m	8 μ m	24 μ m
SPIRE21	28.64	27.18	25.22	24.42	24.16	24.71	22.65	21.79	21.48	20.88	20.37	19.31
SPIRE22	24.19	23.96	23.13	22.22	21.38	20.30	19.48	19.22	19.39	19.76	19.75	17.62
SPIRE23	24.48	24.11	24.03	23.39	22.61	21.32	20.20	19.55	19.41	19.65	19.78	17.92
SPIRE24	28.27	26.28	25.42	25.15	24.65	98.85	22.29	21.99	21.86	21.67	21.86	19.30
SPIRE25	24.57	23.87	22.15	20.92	20.42	19.44	18.25	18.31	18.70	18.60	18.78	16.72
SPIRE26	24.18	23.89	22.90	21.76	21.18	20.35	19.40	19.12	19.42	19.60	19.62	16.92
SPIRE27	99.00	26.40	25.98	25.46	24.95	99.00	99.00	21.56	21.29	21.05	21.17	17.99
SPIRE28	23.82	23.49	22.88	22.13	21.41	20.68	19.95	19.48	19.63	20.00	20.02	18.11
SPIRE29	23.98	23.51	22.51	21.37	21.00	20.21	19.62	19.50	19.88	19.78	20.05	17.21
SPIRE30	24.94	23.90	22.45	21.44	21.02	20.37	19.37	19.70	20.03	20.07	20.23	18.70
SPIRE31	99.00	27.45	26.73	25.94	25.69	99.00	99.00	21.34	20.99	20.61	20.44	19.71
SPIRE32	24.67	24.45	23.26	21.95	21.38	20.50	19.53	19.37	19.77	19.88	20.18	17.82
SPIRE33	99.00	24.89	24.09	23.45	22.96	99.00	99.00	19.80	19.71	19.89	20.07	18.28
SPIRE34	25.96	25.41	24.14	22.77	21.95	20.58	19.54	18.98	19.07	19.21	19.24	16.75
SPIRE35	25.03	24.62	24.18	23.31	22.95	22.20	22.01	21.42	21.80	22.08	22.25	19.89
SPIRE36	27.11	29.36	27.91	27.18	26.89	23.38	21.56	20.80	20.54	20.24	20.54	17.72
SPIRE37	24.34	23.81	22.71	22.57	22.62	21.93	21.80	21.30	20.93	20.53	19.91	18.99
SPIRE38	25.46	25.53	25.03	24.38	24.79	22.71	21.40	21.14	20.84	20.54	20.73	18.07
SPIRE39	99.00	27.83	26.78	26.06	25.98	99.00	99.00	21.50	21.31	20.97	20.96	18.08
SPIRE40	23.83	22.96	21.65	20.82	20.43	19.78	19.02	19.35	19.54	19.60	19.03	17.21

Table 3.2: *cont.*

Name	FUV	NUV	U	F435W	F606W	F775W	F850LP	J	K	3.6 μ m	4.5 μ m	5.8 μ m	8 μ m	24 μ m
SPIRE41	25.83	99.00	99.00	99.00	99.00	21.86	22.74	21.31	21.04	20.65	20.94	17.49
SPIRE42	25.21	25.77	25.10	25.01	24.64	27.27	21.77	21.63	21.38	21.08	21.19	18.62
SPIRE43	26.30	25.78	25.12	24.39	23.49	23.43	21.61	20.46	20.27	20.46	20.45	18.53
SPIRE44	25.72	25.20	23.12	21.57	21.05	20.26	19.05	18.74	19.08	19.12	19.02	16.59
SPIRE45	99.00	29.10	29.27	26.73	25.83	99.00	99.00	20.15	19.83	19.81	20.02	17.60
SPIRE46	25.92	25.73	24.86	23.47	22.28	20.90	19.87	19.28	19.34	19.68	19.83	18.81
SPIRE47	21.32	20.72	19.17	18.41	18.08	17.28	16.73	18.02	18.20	18.63	18.12	17.40
SPIRE48	26.84	33.20	25.51	24.55	23.61	23.99	21.77	21.09	21.15	21.61	21.41	19.97
SPIRE49	99.00	99.00	99.00	99.00	99.00	99.00	99.00	20.23	19.96	20.10	20.27	18.27
SPIRE50	26.21	29.57	24.40	23.11	22.55	21.60	20.46	20.04	20.31	20.40	20.65	17.97
SPIRE51	24.88	24.68	24.35	23.92	23.57	22.91	22.13	20.96	20.71	20.40	20.71	17.51
SPIRE52	99.00	28.99	28.38	27.38	26.97	99.00	99.00	23.57	23.69	22.90	22.17	17.66
SPIRE53	99.00	31.60	26.53	25.26	23.95	99.00	99.00	20.56	20.43	20.77	20.59	18.72
SPIRE54	20.94	23.31	19.46	18.94	18.63	18.09	17.55	18.40	18.27	18.59	17.15	15.96
SPIRE55	24.44	24.32	23.42	22.30	21.78	20.93	20.15	20.01	20.36	20.51	20.69	18.10
SPIRE56	21.48	99.00	99.00	99.00	99.00	18.25	17.67	18.53	18.63	18.88	18.09	16.71
SPIRE57	28.13	26.13	23.85	22.53	22.11	21.42	20.50	20.63	21.05	21.15	20.81	17.60
SPIRE58	25.52	25.08	24.47	24.21	24.07	22.78	21.98	21.23	21.00	21.17	21.36	18.98
SPIRE59	24.57	24.39	23.58	22.53	22.07	21.26	20.58	20.23	20.57	20.68	20.75	17.98
SPIRE60	20.30	21.44	18.48	17.93	17.70	17.09	16.66	17.96	18.16	18.52	16.98	16.58

Table 3.2: *cont.*

Name	FUV	NUV	U	F435W	F606W	F775W	F850LP	J	K	3.6 μ m	4.5 μ m	5.8 μ m	8 μ m	24 μ m
SPIRE61	25.21	24.69	23.64	22.44	21.91	20.80	19.76	19.36	19.66	19.70	19.89	17.07
SPIRE62	25.71	25.03	24.54	24.42	24.09	22.31	21.35	21.72	21.61	21.49	21.73	19.61
SPIRE63	23.49	22.79	21.74	20.86	20.53	19.88	19.12	19.30	19.71	19.57	19.72	17.52
SPIRE64	25.40	24.72	23.69	22.42	21.94	20.87	19.85	19.54	19.92	19.85	19.92	17.19
SPIRE65	25.27	24.87	22.92	21.75	21.29	20.11	19.38	19.62	19.97	19.99	20.11	18.84
SPIRE66	24.31	23.78	22.62	21.38	20.90	20.04	19.05	18.76	18.94	18.78	18.57	16.58
SPIRE67	24.41	23.54	21.96	21.10	20.69	20.02	19.15	19.55	19.66	19.83	19.10	17.96
SPIRE68	25.17	27.54	23.75	22.19	21.65	20.56	19.29	19.14	19.51	19.48	19.68	17.00
SPIRE69	25.34	24.67	23.45	22.12	21.64	20.69	19.90	19.70	20.06	19.99	20.15	17.48
SPIRE70	24.50	24.09	23.38	22.59	21.86	21.14	20.04	19.56	19.60	19.96	19.75	17.56
SPIRE71	21.61	99.0	20.13	19.56	19.26	18.73	18.16	18.90	18.92	19.19	18.02	16.81
SPIRE72	25.50	24.99	24.13	22.93	22.35	21.29	20.18	19.95	20.26	20.37	20.57	17.88
SPIRE73	24.30	23.40	23.43	22.96	22.65	21.70	20.97	20.95	20.95	20.97	20.87	18.56
SPIRE74	25.09	24.36	23.91	23.09	22.45	20.83	19.91	19.29	19.11	19.28	19.55	17.46

Table 3.2: *cont.*

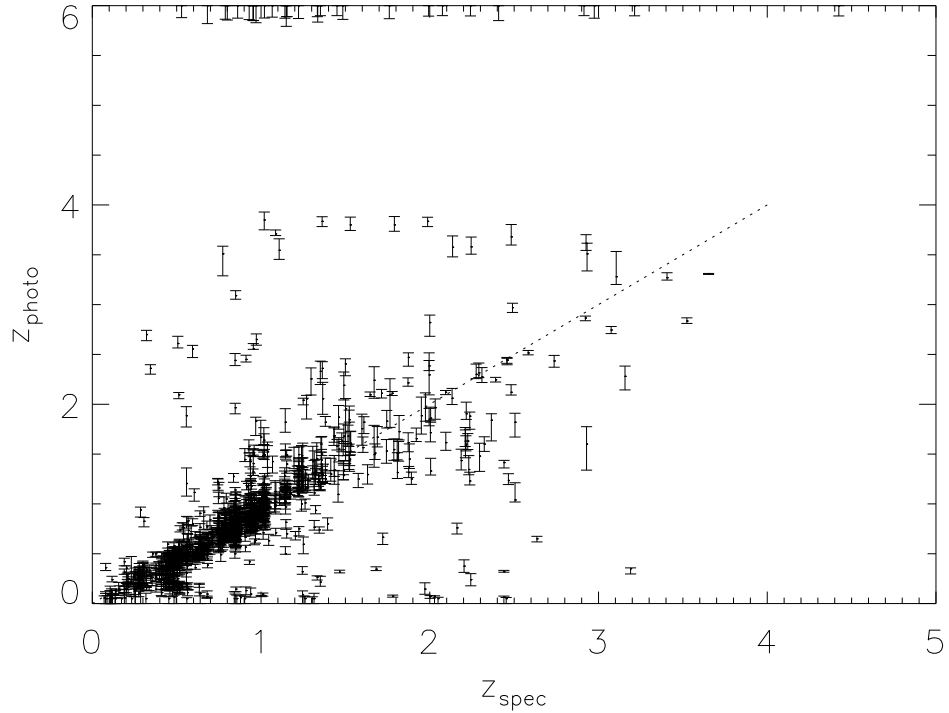


Figure 3.2: A plot of the estimated photometric redshift (z_{photo}) versus the B08 spectroscopic redshift (z_{spec}) for each EIP source where a spectroscopic redshift is available. The dashed line shows where $z_{photo} = z_{spec}$.

photometric redshift estimates at the upper limit, 6, meaning that the program has been unable to find any good fits to the data. Therefore all of these results should be discarded. There appears to be a relatively tight correlation between photometric and spectroscopic redshift up to values of $\sim 1 - 1.5$. Beyond this redshift the correlation appears to become much looser. Thus photometric redshifts higher than this should not be considered to be reliable.

Table 3.3 lists the photometric redshifts (using the same photometric bands, magnitude limits and settings as described previously) for all 74 of the SPIRE sources with single optical counterparts. Also listed are the B08 spectroscopic redshifts where available. Figure 3.3 shows a plot of the photometric redshifts versus their B08 spectroscopic redshifts (where available). This plot is similar to the one for

the entire EIP catalogue, with the photometric redshifts appearing to become less reliable beyond redshifts of $\sim 1 - 1.5$ (there are very few sources with spectroscopic redshifts beyond this - so it's impossible to tell exactly where photometric redshift estimates begin to fail from this plot alone).

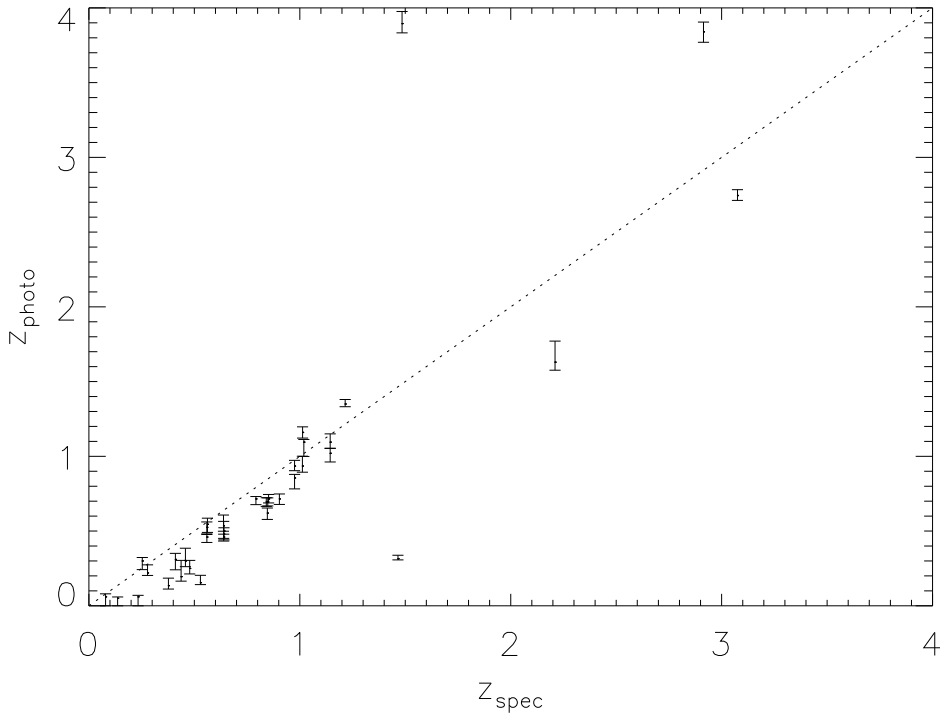


Figure 3.3: A plot of the estimated photometric redshifts (z_{photo}) versus the B08 spectroscopic redshifts (z_{spec}) for each of the SPIRE sources with a single optical counterpart, where a spectroscopic redshift is available. The dashed line shows where $z_{\text{photo}} = z_{\text{spec}}$.

3.4 Morphology as a Function of Redshift

In the previous section I focused on non-merging, isolated sources. However for the rest of this chapter I include in my results any source which has some form of redshift estimate. This includes non-merging, isolated sources with a spectroscopic redshift if available, or with a photometric redshift estimate if not, as well as pos-

Name	z_{spec}	z_{photo}	χ^2
SPIRE1	0.98	$0.94^{+.04}_{-.03}$	30.02
SPIRE2	0.28	$0.22^{+.05}_{-.02}$	29.64
SPIRE3	0.84	$0.69^{+.03}_{-.03}$	16.83
SPIRE4	0.23	$0.06^{+.01}_{-.06}$	34.07
SPIRE5	0.25	$0.30^{+.02}_{-.06}$	29.32
SPIRE6	1.02	$1.10^{+.02}_{-.10}$	31.13
SPIRE7	0.44	$0.19^{+.11}_{-.03}$	28.82
SPIRE8	0.64	$0.48^{+.09}_{-.03}$	28.26
SPIRE9	0.38	$0.14^{+.05}_{-.02}$	32.75
SPIRE10	0.48	$0.25^{+.05}_{-.04}$	28.17
SPIRE11	0.56	$0.55^{+.04}_{-.05}$	28.43
SPIRE12	0.85	$0.69^{+.03}_{-.03}$	16.99
SPIRE13	0.46	$0.30^{+.08}_{-.04}$	28.25
SPIRE14	0.90	$0.71^{+.03}_{-.04}$	28.24
SPIRE15	0.08	$0.06^{+.02}_{-.06}$	31.24
SPIRE16	0.64	$0.54^{+.07}_{-.04}$	28.25
SPIRE17	0.41	$0.31^{+.04}_{-.07}$	28.49
SPIRE18	0.14	$0.05^{+.01}_{-.05}$	31.76
SPIRE19	0.56	$0.52^{+.04}_{-.04}$	28.42
SPIRE20	0.64	$0.46^{+.02}_{-.03}$	28.65
SPIRE21	-9.00	$3.65^{+.05}_{-.03}$	2.57
SPIRE22	1.14	$1.02^{+.03}_{-.06}$	2.09
SPIRE23	-9.00	$1.66^{+.10}_{-.07}$	2.88
SPIRE24	-9.00	$3.04^{+.02}_{-.04}$	36.53
SPIRE25	0.64	$0.50^{+.02}_{-.06}$.76
SPIRE26	0.98	$0.86^{+.02}_{-.07}$.37
SPIRE27	-9.00	$3.86^{+.05}_{-.10}$	19.74
SPIRE28	1.14	$1.10^{+.05}_{-.04}$.45
SPIRE29	0.85	$0.62^{+.03}_{-.04}$.73
SPIRE30	0.56	$0.46^{+.02}_{-.04}$.88

Table 3.3: The photometric redshift estimates (z_{photo}), 1σ errors and reduced χ^2 fit values for each of the 74 SPIRE sources with a single optical counterpart. The spectroscopic redshifts from B08 are also included where available (z_{spec}). A value of -9.00 denotes where no spectroscopic redshift is available.

Name	z_{spec}	z_{photo}	χ^2
SPIRE31	2.91	$3.84^{+.07}_{-.07}$	10.45
SPIRE32	0.85	$0.71^{+.03}_{-.03}$.67
SPIRE33	1.48	$3.89^{+.08}_{-.06}$	67.87
SPIRE34	1.01	$1.16^{+.04}_{-.04}$	1.34
SPIRE35	1.01	$0.94^{+.07}_{-.04}$	1.42
SPIRE36	-9.00	$1.88^{+.17}_{-.06}$	2.90
SPIRE37	3.08	$2.74^{+.04}_{-.03}$	4.36
SPIRE38	2.21	$1.63^{+.14}_{-.05}$	3.89
SPIRE39	-9.00	$3.71^{+.06}_{-.17}$	8.27
SPIRE40	0.53	$0.16^{+.05}_{-.01}$.63
SPIRE41	-9.00	$1.40^{+.29}_{-.27}$.43
SPIRE42	-9.00	$3.38^{+.19}_{-.07}$	62.64
SPIRE43	1.47	$0.31^{+.02}_{-.01}$	1.22
SPIRE44	0.79	$0.71^{+.02}_{-.04}$.96
SPIRE45	-9.00	$5.67^{+.07}_{-.10}$	1.75
SPIRE46	1.22	$1.35^{+.03}_{-.02}$	1.05
SPIRE47	-9.00	$0.19^{+.01}_{-.04}$	4.57
SPIRE48	-9.00	$4.24^{+.01}_{-.00}$	4.78
SPIRE49	-9.00	$4.24^{+1.5}_{-.31}$	1.56
SPIRE50	-9.00	$4.16^{+.00}_{-.01}$	9.34
SPIRE51	-9.00	$0.34^{+.06}_{-.02}$.36
SPIRE52	-9.00	$0.22^{+.10}_{-.22}$	1.80
SPIRE53	-9.00	$4.18^{+.03}_{-.03}$	12.39
SPIRE54	-9.00	$0.46^{+.00}_{-.00}$	15.21
SPIRE55	-9.00	$0.81^{+.03}_{-.03}$.81
SPIRE56	-9.00	$1.04^{+.09}_{-.06}$	37.14
SPIRE57	-9.00	$0.40^{+.02}_{-.03}$	2.09
SPIRE58	-9.00	$1.95^{+.09}_{-.10}$.56
SPIRE59	-9.00	$0.85^{+.06}_{-.03}$.49
SPIRE60	-9.00	$0.24^{+.01}_{-.02}$	10.85

Table 3.3: *cont.*

Name	z_{spec}	z_{photo}	χ^2
SPIRE61	0.88	$0.83^{+.08}_{-.04}$.829
SPIRE62	-9.00	$1.33^{+.17}_{-.03}$	8.02
SPIRE63	0.63	$0.48^{+.04}_{-.04}$	1.15
SPIRE64	0.85	$0.76^{+.03}_{-.07}$.99
SPIRE65	0.56	$0.31^{+.02}_{-.04}$	2.55
SPIRE66	0.86	$0.74^{+.03}_{-.04}$.29
SPIRE67	0.48	$0.30^{+.06}_{-.08}$.73
SPIRE68	-9.00	$0.50^{+.04}_{-.01}$	3.08
SPIRE69	0.85	$0.59^{+.07}_{-.02}$	1.12
SPIRE70	1.248	$1.22^{+.15}_{-.05}$.23
SPIRE71	-9.00	$4.39^{+.01}_{-.01}$	25.14
SPIRE72	0.94	$0.90^{+.03}_{-.08}$	1.14
SPIRE73	-9.00	$1.24^{+.07}_{-.05}$	3.38
SPIRE74	-9.00	$1.69^{+.05}_{-.04}$	2.37

Table 3.3: *cont.*

sibly merging systems with an associated spectroscopic redshift. Possible merging systems with no associated spectroscopic redshift cannot be included as I cannot reliably estimate a photometric redshift for them.

Figures 3.4, 3.5, 3.6, 3.7, 3.8 and 3.9 collect thumbnails of the ACS F850LP imaging for each of the SPIRE optical XIDs with some form of redshift estimate (be it spectroscopic or photometric), that lie in the redshift ranges $z < 0.4$, $0.4 < z < 0.8$, $0.8 < z < 1.2$, $1.2 < z < 1.6$, $1.6 < z < 2.0$ and $z > 2.0$ respectively.

Table 3.4 divides up the total number of sources that lie in each redshift band. These are then further sub-divided into the number of SPIRE sources with a single optical counterpart, and those with a possible merger system counterpart. Also given are the number of isolated sources which appear to be spiral galaxies.

At redshifts $z < 0.8$, visual examination of the F850LP images shows direct evidence of interaction between possibly merging systems for a number of SPIRE counterparts - suggesting that these are in fact genuinely interacting merging sys-

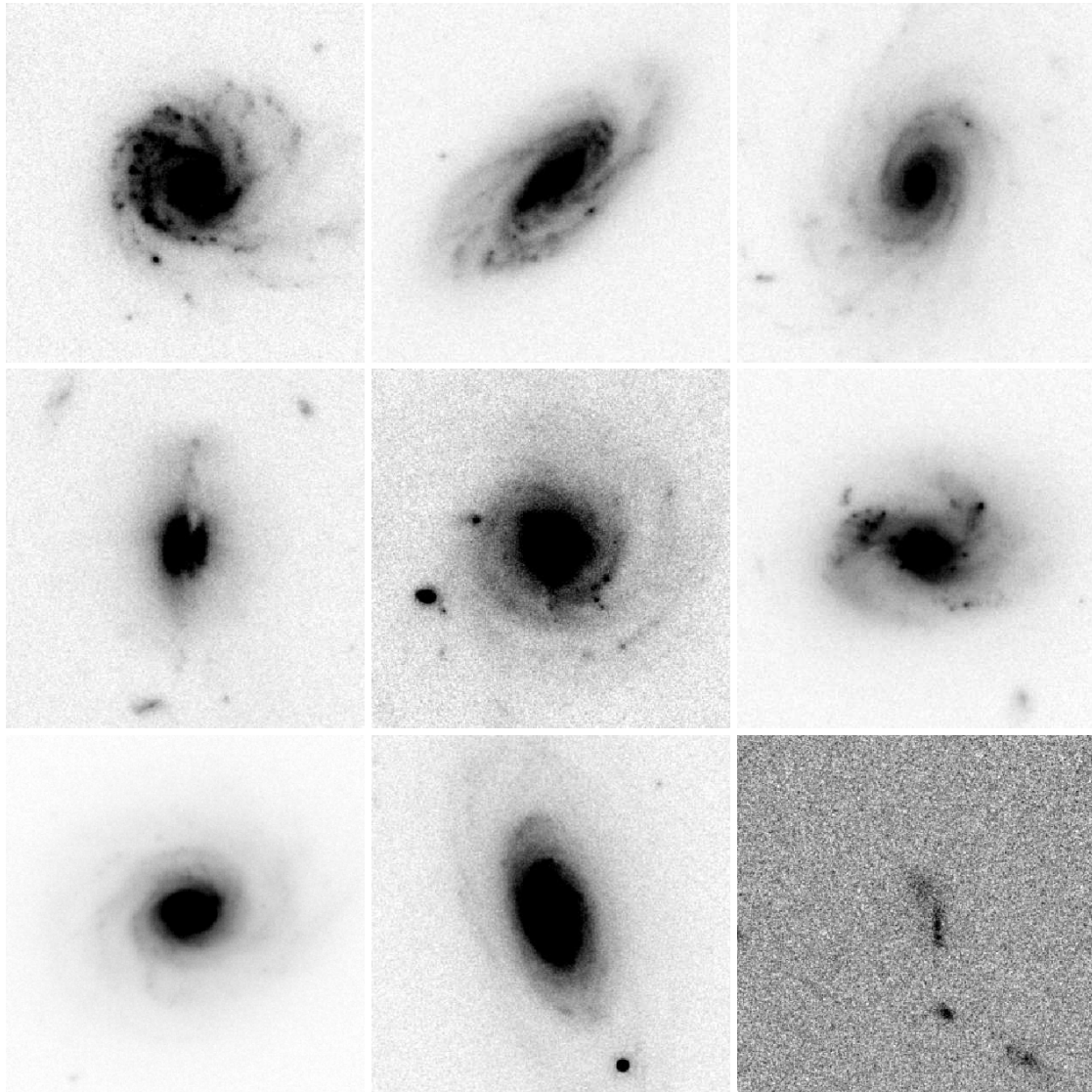


Figure 3.4: The ACS F850LP band cutouts for SPIRE sources at redshifts $z < 0.4$. The images are all $10''$ across. Top to bottom, left to right: SPIRE2, 60, 4, 5, 9, 15, 18, 47, 51.

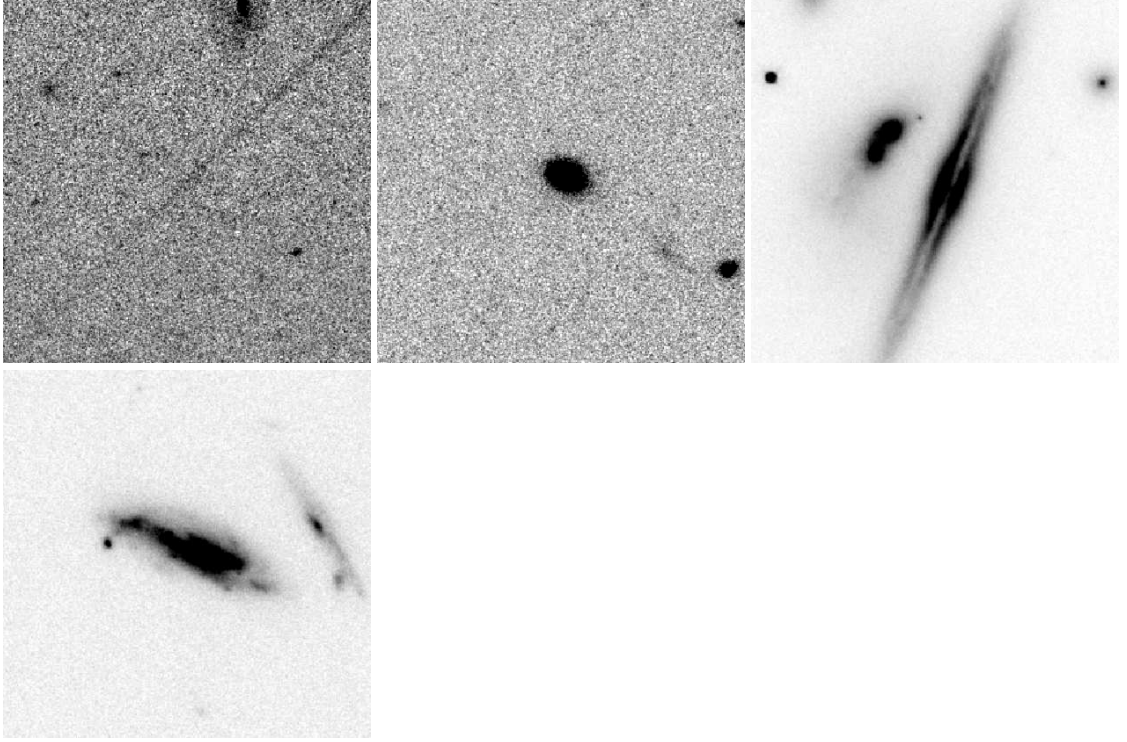


Figure 3.4: *cont.* Top to bottom, left to right: SPIRE52, 57, 87, 111.

Redshift Band	Total	Single Counterpart	Possible Merger	Spiral
$z < 0.4$	13	11	2	7
$0.4 < z < 0.8$	23	18	5	7
$0.8 < z < 1.2$	33	20	13	8
$1.2 < z < 1.6$	14	7	7	1
$1.6 < z < 2.0$	4	4	0	0
$z > 2.0$	15	14	1	1

Table 3.4: The total number of sources that lie in the redshift bands $z < 0.4$, $0.4 < z < 0.8$, $0.8 < z < 1.2$, $1.2 < z < 1.6$, $1.6 < z < 2.0$ and $z > 2.0$. The number of sources in each redshift band is further subdivided into number of single source counterparts, possible merger system counterparts, and isolated spiral counterparts according to their visual classification based on ACS F850LP imaging.

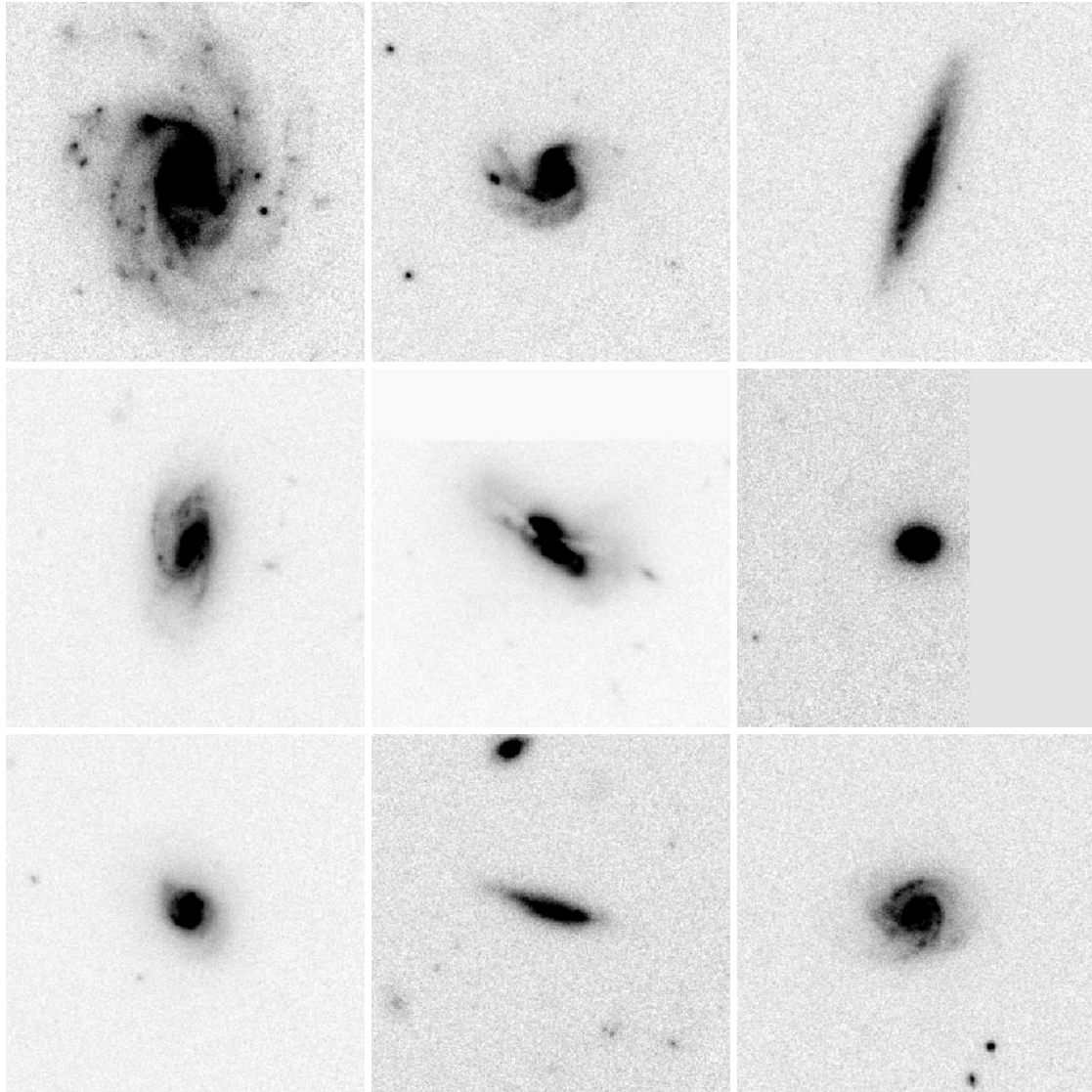


Figure 3.5: The ACS F850LP band cutouts for SPIRE sources at redshifts $0.4 < z < 0.8$. The images are all $10''$ across. Top to bottom, left to right: SPIRE7, 8, 10, 11, 13, 16, 17, 19, 20.

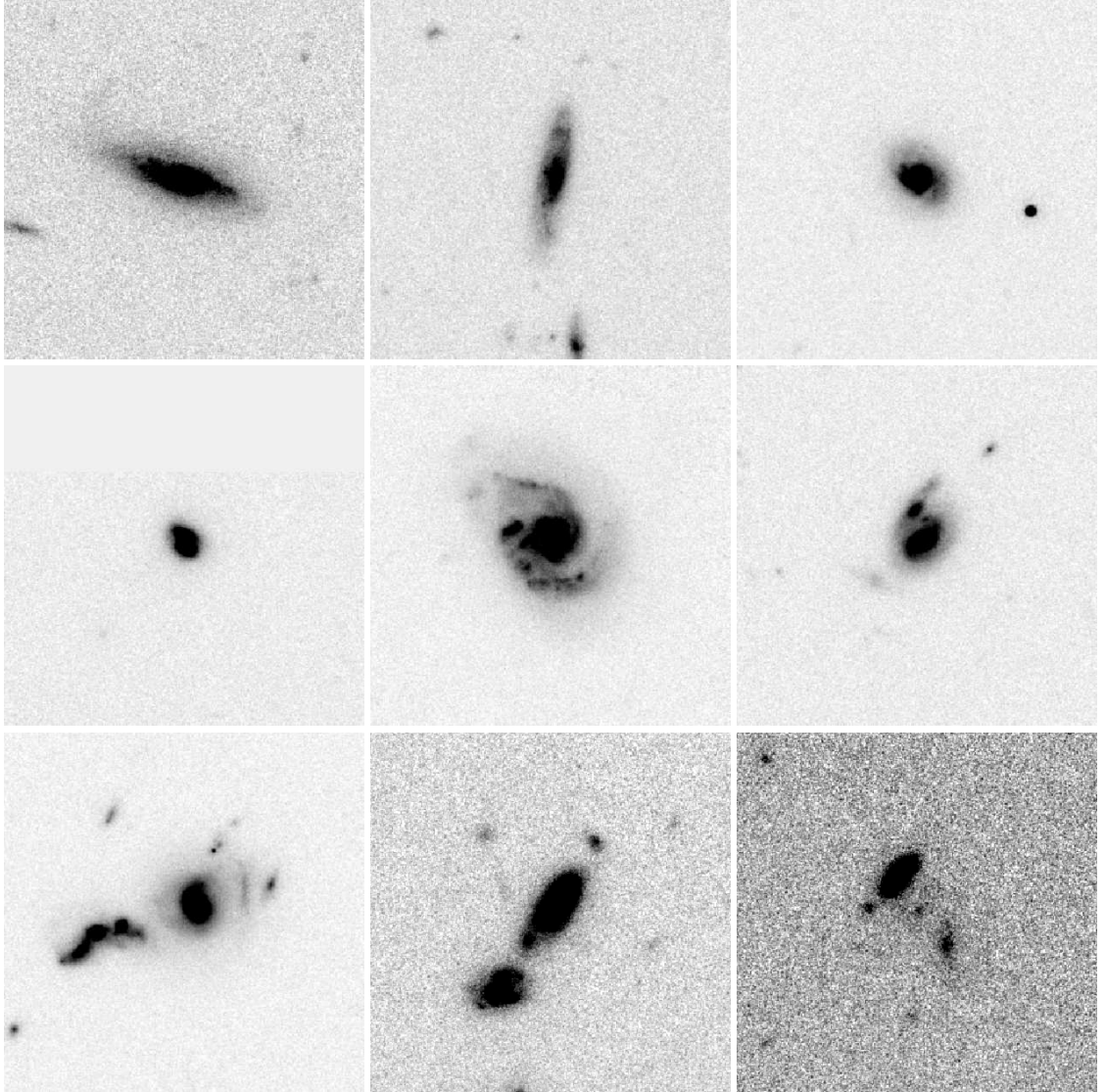


Figure 3.5: *cont.* Top to bottom, left to right: SPIRE25, 30, 40, 44, 54, 107, 93, 94, 82.

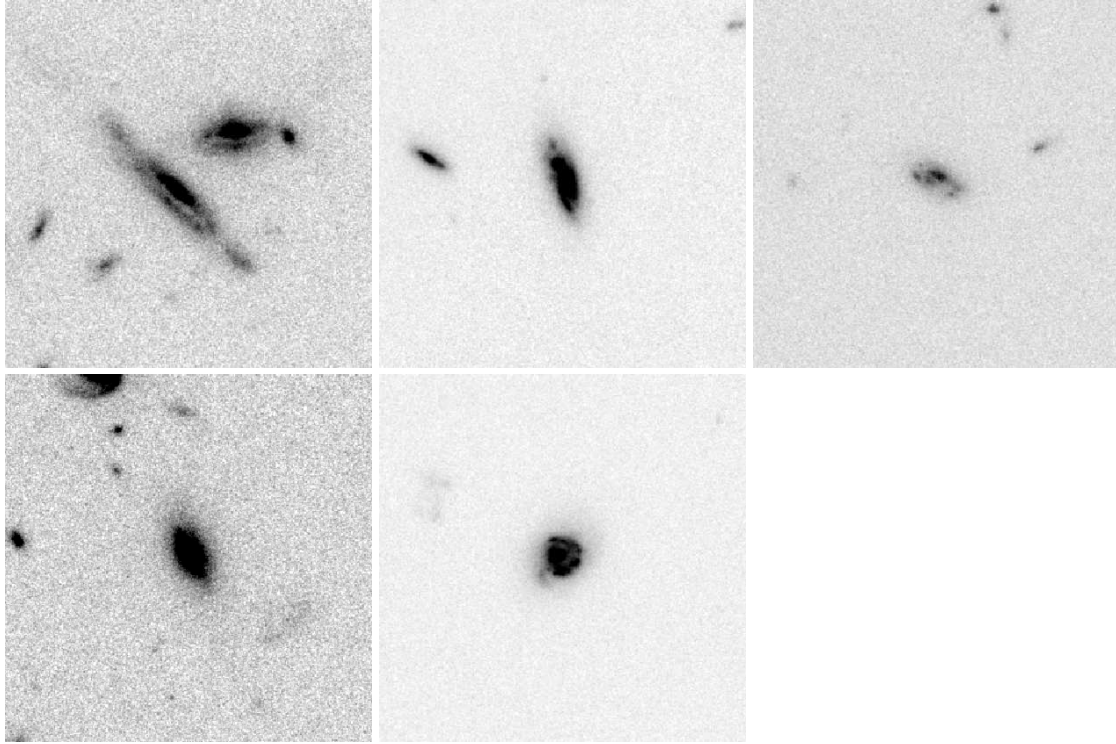


Figure 3.5: *cont.* Top to bottom, left to right: SPIRE106, 67, 68, 65, 63.

tems. At higher redshifts than this the ACS imaging is not sensitive enough to show any observable evidence of physical processes such as tidal interaction occurring.

Similarly, spiral galaxies are easier to identify at redshifts $z < 0.8$ than in the higher redshift bands. This is again due to the ACS imaging at redshifts higher than this not being sensitive enough to be able to visually identify the spiral arms.

3.5 Discussion

Visually classifying the optical morphology of galaxies is highly subjective. The $(1+z)^4$ surface brightness dimming of galaxies makes it very difficult to see tidal tails and morphology at high redshifts. Apparent major mergers are subject to contamination from irregular galaxies, and at redshifts $z > 0.8$ the ACS imaging is

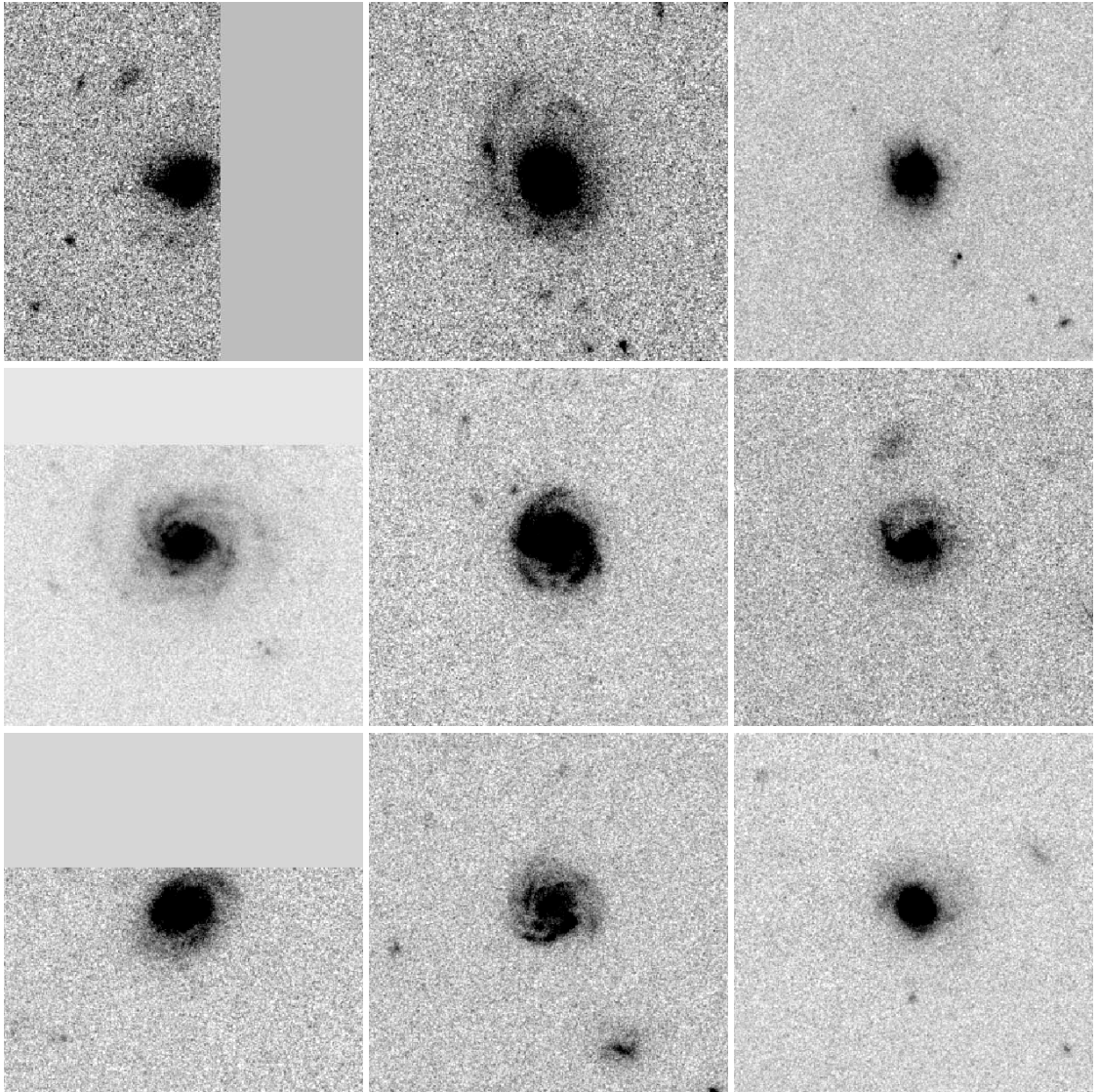


Figure 3.6: The ACS F850LP band cutouts for SPIRE sources at redshifts $0.8 < z < 1.2$. The images are all $10''$ across. Top to bottom, left to right: SPIRE1, 3, 6, 12, 14, 22, 16, 28, 29.

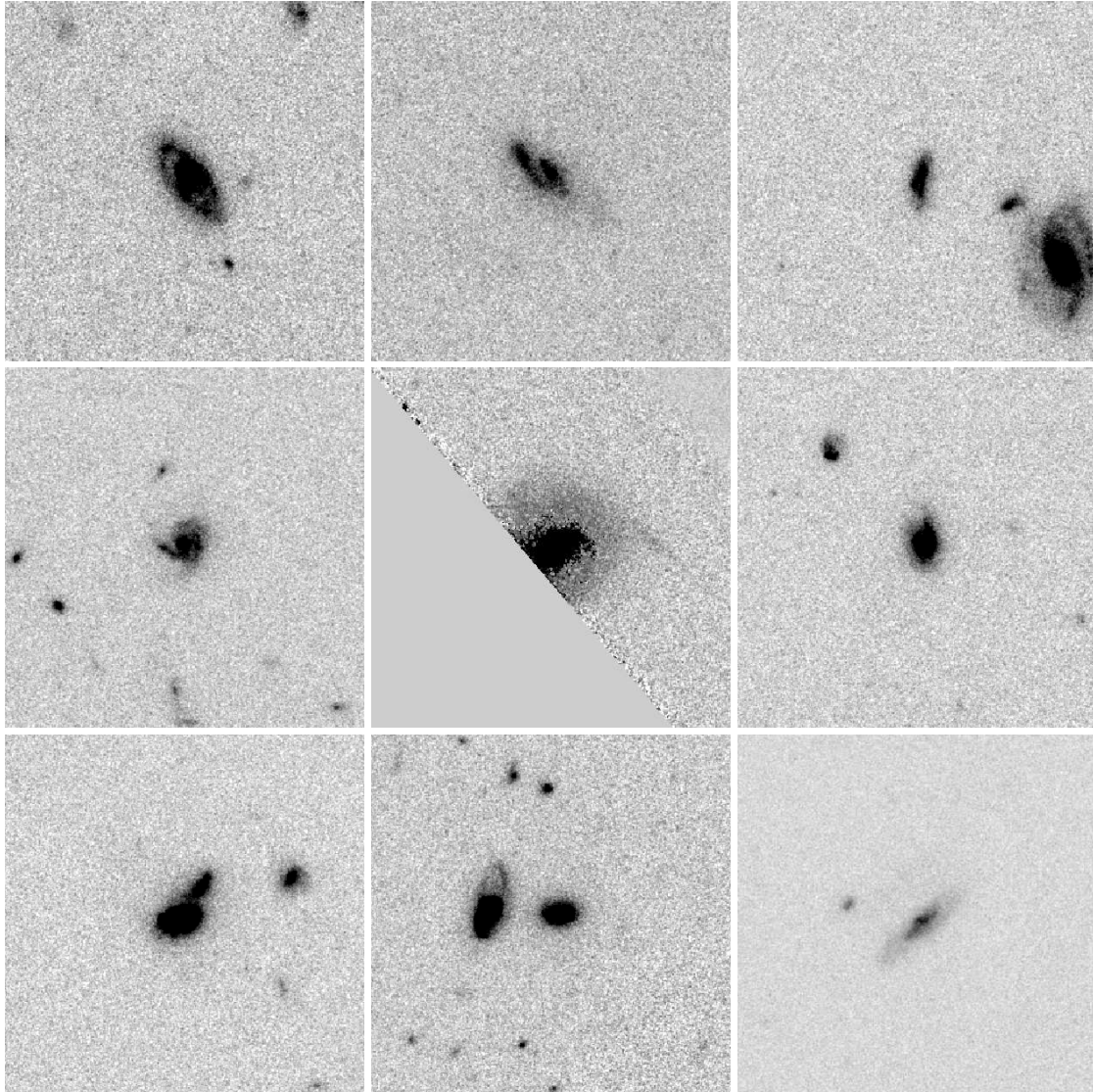


Figure 3.6: *cont.* Top to bottom, left to right: SPIRE32, 34, 35, 55, 56, 59, 88, 79, 109.

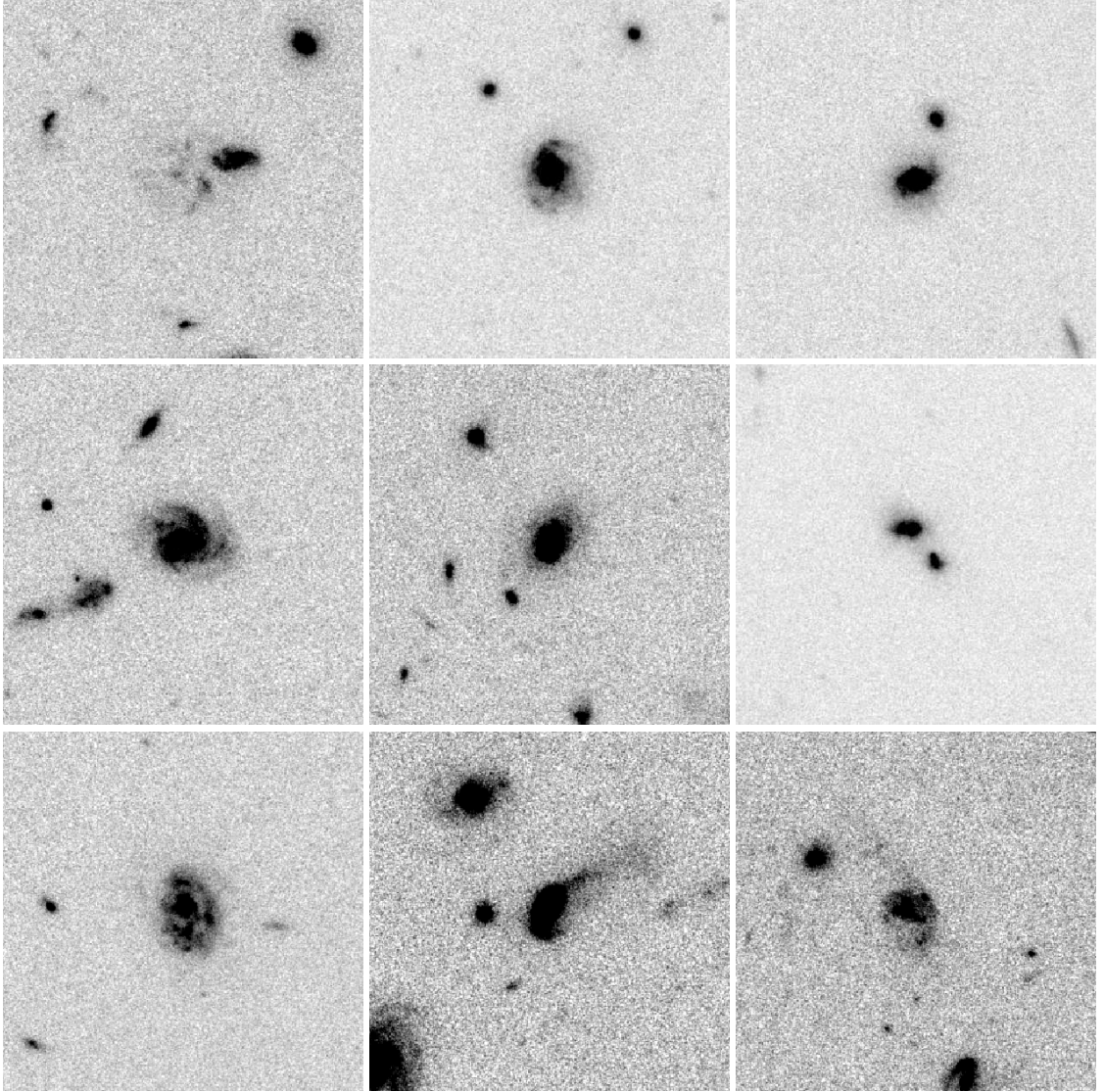


Figure 3.6: *cont.* Top to bottom, left to right: SPIRE91, 85, 108, 101, 89, 102, 104, 80, 81.

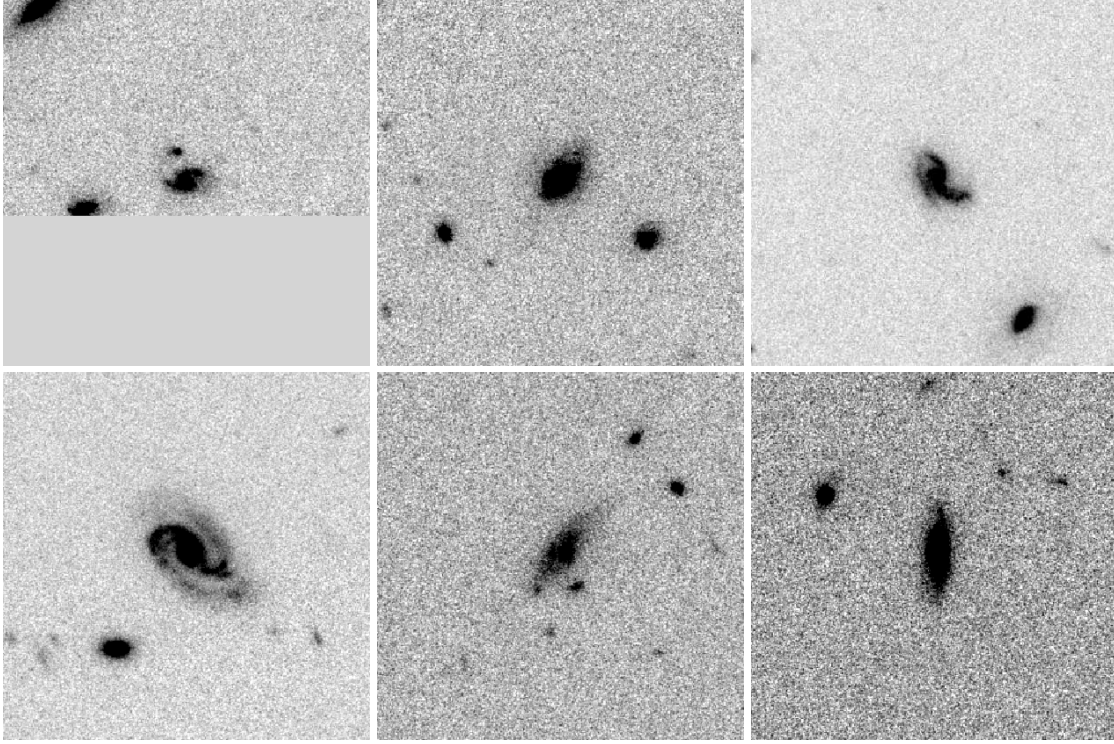


Figure 3.6: *cont.* Top to bottom, left to right: SPIRE83, 64, 69, 66, 61, 72.

not sensitive enough to be able to see direct evidence of interaction. Therefore the best estimate of the number of merging systems has to take into account how many of my identified possible merging system counterparts could simply be coincident with the IRAC emission by chance.

To determine how many of the possible mergers in table 3.4 could be chance coincidences of optical counterparts with the IRAC emission, I take number counts for the HDF field from Williams et al. (1996). I take the number counts for the F814W band as this is the closest available band to the F850LP band used in this work. The mean F850LP band magnitude of sources in the EIP catalogue is ~ 23 , and in the examples where there is a possible merger occurring, the component sources are typically separated by between 1 and $3''$.

Using the number counts from figure 30 of Williams et al. (1996), my estimates

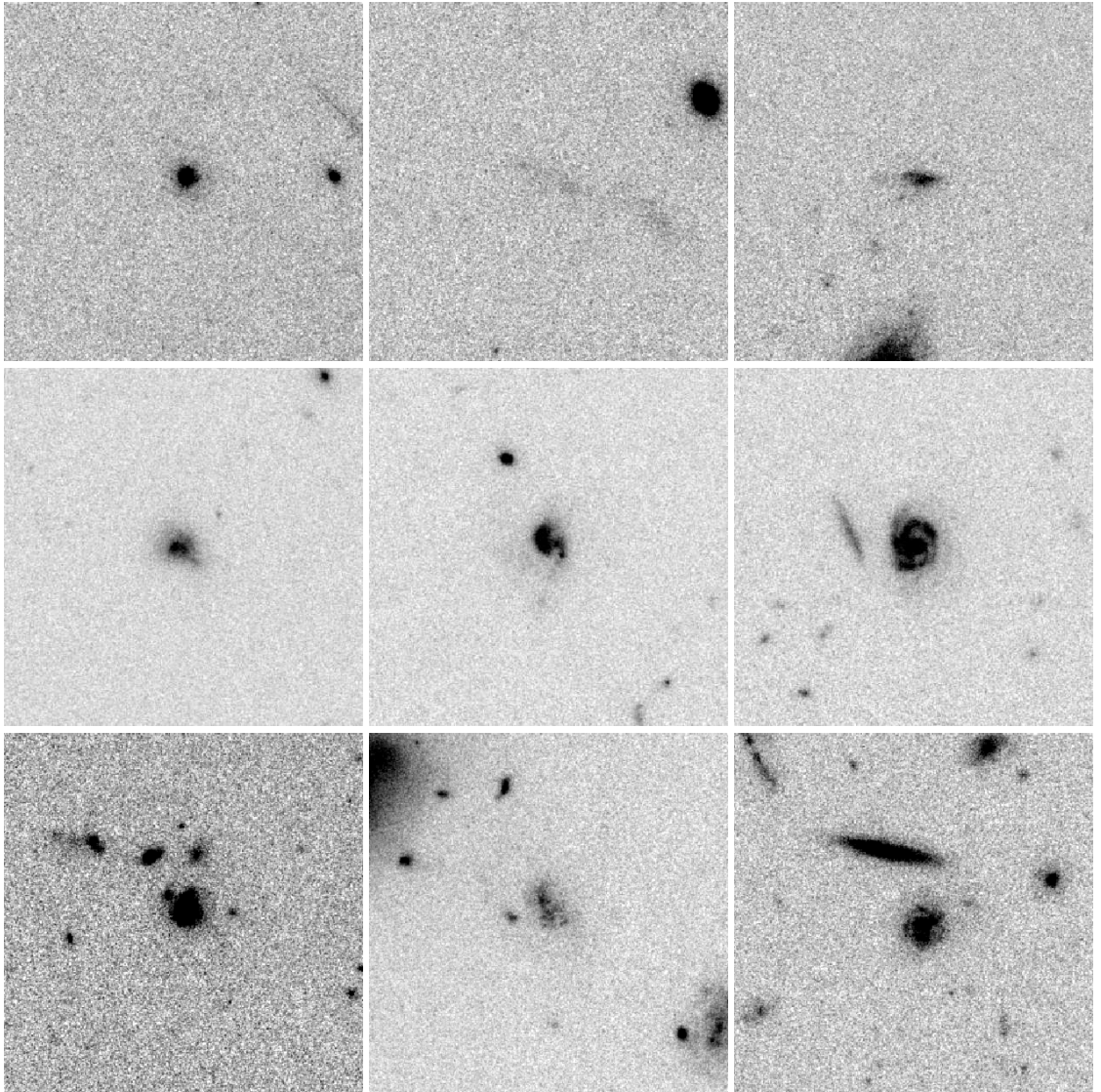


Figure 3.7: The ACS F850LP band cutouts for SPIRE sources at redshifts $1.2 < z < 1.6$. The images are all $10''$ across. Top to bottom, left to right: SPIRE33, 41, 43, 46, 95, 112, 98, 97, 76.

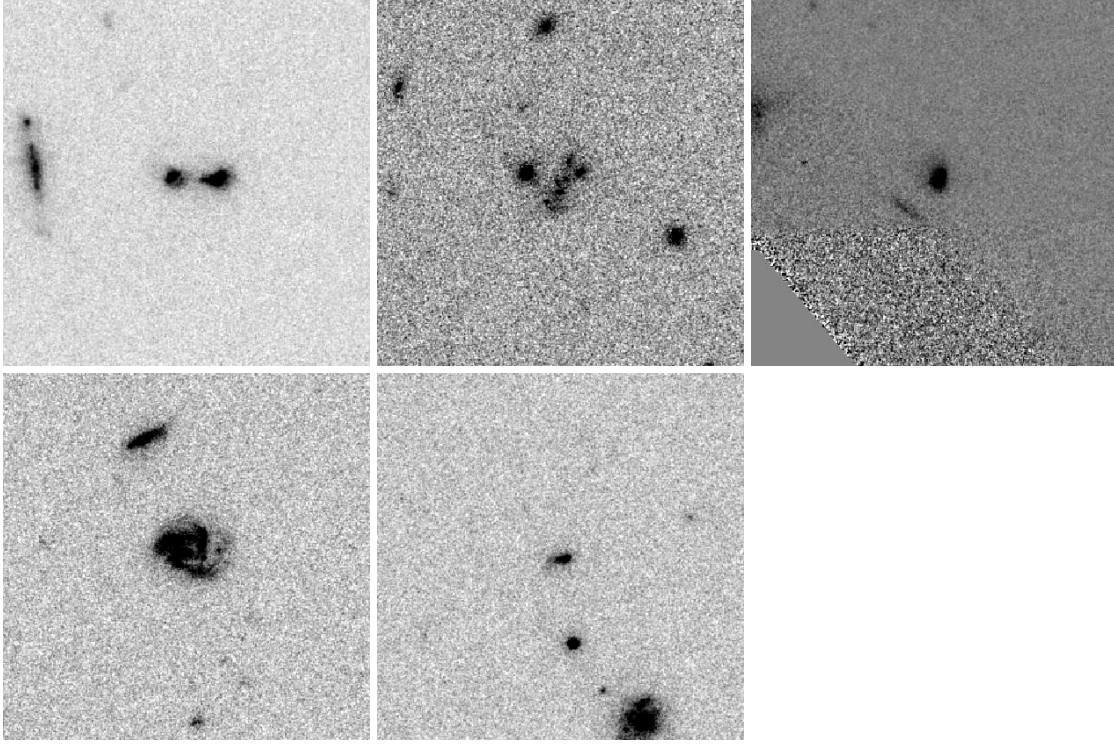


Figure 3.7: *cont.* Top to bottom, left to right: SPIRE110, 75, 73, 70, 62.

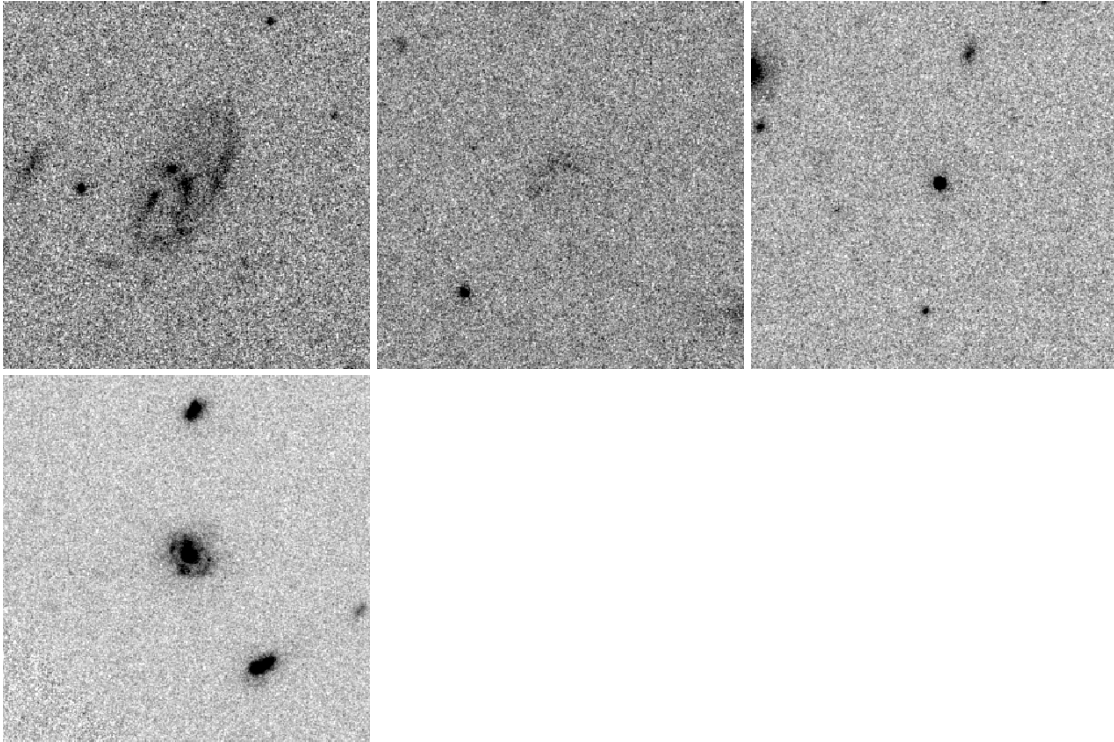


Figure 3.8: The ACS F850LP band cutouts for SPIRE sources at redshifts $1.6 < z < 2.0$. The images are all 10'' across. Top to bottom, left to right: SPIRE23, 36, 58, 74.

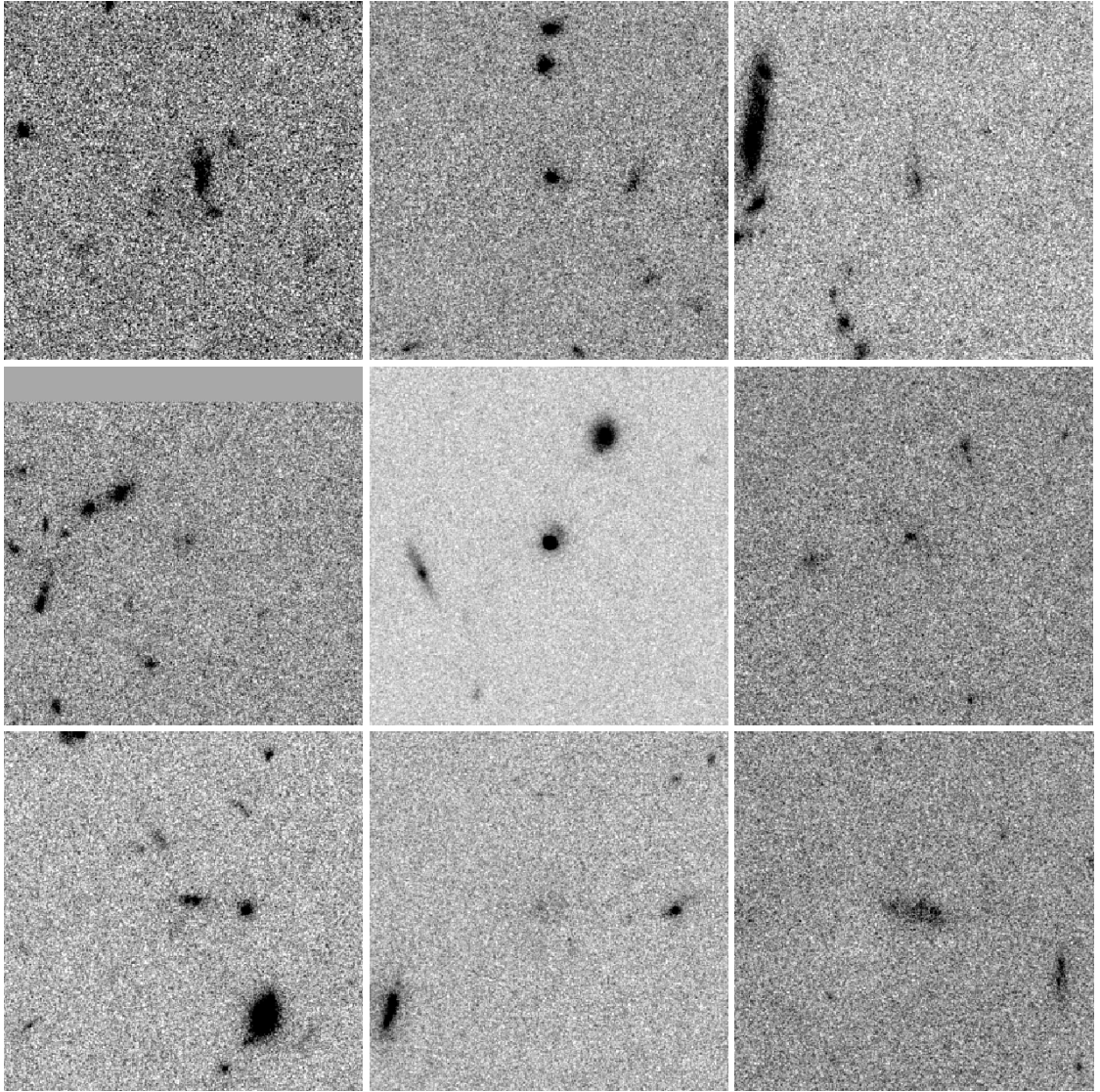


Figure 3.9: The ACS F850LP band cutouts for SPIRE sources at redshifts $z > 2.0$. The images are all 10'' across. Top to bottom, left to right: SPIRE21, 24, 27, 31, 37, 39, 42, 45, 48.

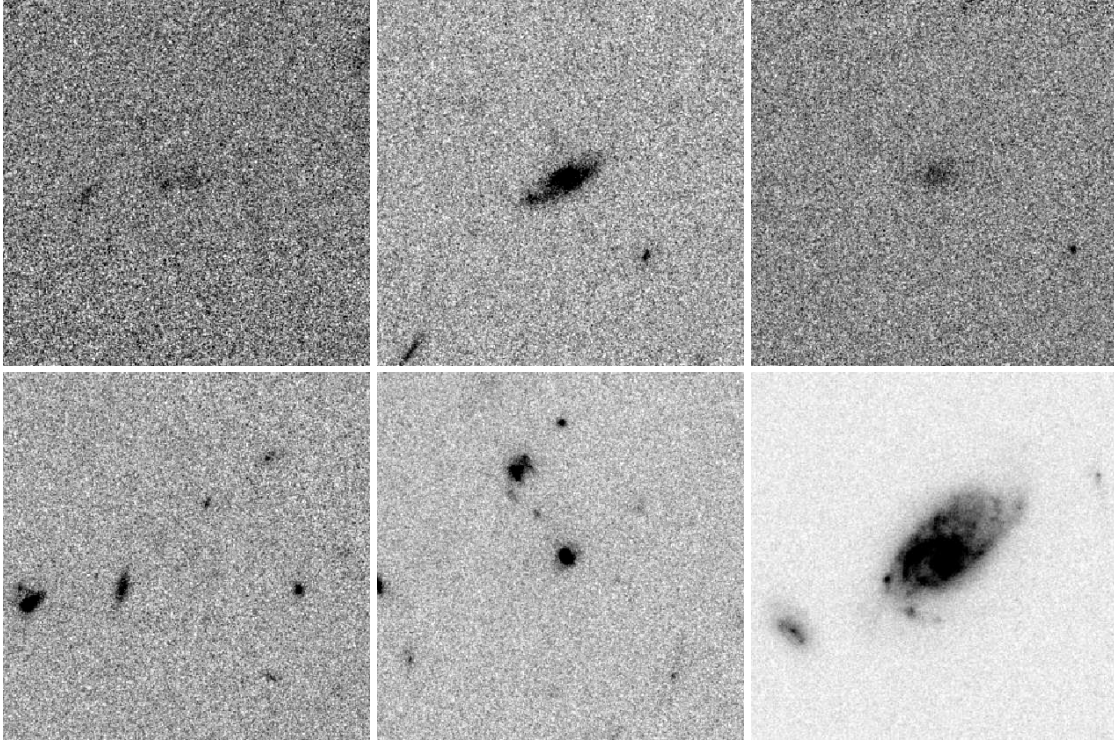


Figure 3.9: *cont.* Top to bottom, left to right: SPIRE49, 50, 53, 38, 96, 71.

of the number of contaminants in the possible merger set in each redshift band is given in table 3.5.

Also shown in table 3.5 are the percentages of mergers (corrected for contamination) and isolated spirals that lie in each of the redshift bands. The percentage of mergers in each band appears to increase with redshift up to the $1.6 < z < 2.0$

Redshift Band	Contaminants	% Mergers (Corrected)	% Spiral
$z < 0.4$	1-2	4	54
$0.4 < z < 0.8$	2-3	11	30
$0.8 < z < 1.2$	4-5	26	24
$1.2 < z < 1.6$	1-2	40	7
$1.6 < z < 2.0$	0-1	0	0
$z > 2.0$	1-2	0	7

Table 3.5: My estimated number of contaminants, the percentage of mergers (corrected for contamination) and the percentage of isolated spirals that lie in the redshift bands $z < 0.4$, $0.4 < z < 0.8$, $0.8 < z < 1.2$, $1.2 < z < 1.6$, $1.6 < z < 2.0$ and $z > 2.0$.

band. The drop beyond this redshift may not be a real effect as the sources at these redshifts are very faint and thus in a merger system the companion galaxy may be too faint to detect.

The percentage of isolated spirals drops with redshift up until $z = 1.6$ and stays approximately constant beyond (ignoring the results for the $1.6 < z < 2.0$ band as the sample size is too small to draw any reliable conclusions from). Similarly to mergers, the morphological classification of spirals becomes more difficult with increasing redshift, thus the total number of isolated spiral galaxies is very possibly underestimated, particularly in the higher redshift bands. Additionally, a large number of the optical counterparts appear as though they may be edge on, and this may result in an underestimation of the number of spiral galaxies across all the redshift bands.

I do not find direct evidence for as many spiral galaxies at $z \sim 1$ as has been found in previous work (e.g., Bell et al., 2005; Elbaz et al., 2007), which estimate that as many as half of all LIRGs at these redshifts show the optical morphology of spirals. However, my total number of spirals is highly likely to have been underestimated due to lack of sensitive optical imaging and the large number of possible edge-on galaxies. Thus, it appears as though more of the SPIRE galaxies at $z \sim 1$ may be being powered by spiral galaxies than by major mergers.

In the $0.8 < z < 1.2$ band, which is centered on $z = 1$, the epoch since which the cosmic SFR has apparently dramatically declined, only $\sim 1/4$ of the SPIRE sources present evidence of being powered by a major merger. Even at higher redshifts than this, at most only $\sim 2/5$ of SPIRE sources appear as they they could be being powered by a major merger. This result is in agreement with mounting evidence (e.g., Bell et al., 2005; Zheng et al., 2004; Melbourne et al., 2005; Elbaz et al.,

2007) that the drop in the rate of major mergers since this era is not the primary cause of the sharp decline of the cosmic SFR.

There are 10 possible mergers which could not be included in the redshift banding sample, as they don't have a spectroscopic redshift and I cannot estimate a photometric redshift for them. Given that the majority of sources with no spectroscopic redshift are more likely to lie in the more distant redshift bands, these additional sources probably wouldn't have a strong effect on the results from the $0.8 < z < 1.2$ band if they could be included. However, they may have a stronger effect on the results for the higher redshift bands if included. In addition the 3 sources that appear to be missing in the EIP catalogue are optically very faint, and therefore probably also lie in the higher redshift bands. The SPIRE single source XID whose IRAC emission is heavily confused may lie in this redshift band, but the addition of one extra source to the sample shouldn't effect the results too adversely.

More important, however, is that my sample only accounts for $\sim 15\%$ of the CIB (Oliver et al., 2010; Eales et al., 2010). If the majority of sources making up the CIB lie at moderate redshifts similar to those investigated in this work, as implied by the stacking analysis of BLAST data by Pascale et al. (2009), then my sample should be representative of the CIB as a whole. However, if a large fraction of sources comprising the unresolved part of the CIB lie at redshifts greater than this, then the SPIRE observations may not be sensitive enough to gather a sample which is truly representative of the total population of galaxies making up the CIB.

3.6 Conclusions

I find in this chapter that only $\sim 1/4$ of SPIRE sources at $z \sim 1$ are showing evidence of undergoing major mergers. This may actually be an upper limit because even though some of the apparently merging systems may be gravitationally bound, they are not necessarily physically interacting. The ACS imaging in this redshift range is not sensitive enough to look directly for visible physical interaction between the component galaxies. Therefore further work would benefit from deeper optical imaging of this region.

This work suggests that the drop in major mergers since $z \sim 1$ is not the primary cause of the sharp decline in the cosmic SFR since this epoch. Other possible explanations for the decline in cosmic SFR include physical processes that do not strongly effect the galaxy's optical morphology, eg. minor mergers, weak tidal interactions with small satellite galaxies and cold gas exhaustion. However, the true physical cause of the decline in the cosmic SFR since $z \sim 1$ has yet to be identified.

CANDELS (Cosmic Assembly Near infrared Deep Extragalactic Legacy Survey - candels.ucolick.org), a new deep NIR imaging survey of galactic evolution between $z = 1.5 - 8$ is being carried out using WFC3/IR and ACS onboard the HST . This may provide imaging sensitive enough to reliably classify the morphology of higher redshift sources, which could help further constrain the total number of SPIRE sources being powered by major mergers and spiral galaxies at these redshifts.

Chapter 4

Star Formation Rates of Herschel Galaxies in the GOODS-N Field

4.1 Introduction

The link between galaxy mass and star formation rate (SFR) is of fundamental importance in understanding the process of galaxy formation. Early hierarchical galaxy formation models predicted that star formation started in low-mass galaxies, which then built up through sequential mergers to form high-mass galaxies (Baugh et al., 1996; Cole et al., 2000). However, studies have found a large population of massive galaxies ($M > 10^{11} M_{\odot}$) at redshifts $z > 1$ (Elston et al., 1988; Hughes et al., 1998b; Franx et al., 2003; Glazebrook et al., 2004), with passively evolving stellar populations (Daddi et al., 2004; Reddy et al., 2005; Kriek et al., 2006, 2008; Cimatti et al., 2008). These results seem to support a “downsizing” scenario (Cowie et al., 1996; Heavens et al., 2004; Juneau et al., 2005; Pérez-González et al., 2005; Bundy et al., 2006) where the most massive galaxies form first.

The specific SFR ($\text{sSFR} = \text{SFR}/\text{mass}$) of a galaxy is of particular interest as it measures how important the galaxy's current star formation is compared with the overall star formation history of the galaxy (e.g., da Cunha et al., 2010). Similar results regarding the redshift evolution of sSFR as a function of stellar mass have been found in a number of studies over a wide range of redshifts ($0 \leq z \leq 3$) (e.g., Feulner et al., 2005; Erb et al., 2006; Damen et al., 2009; Daddi et al., 2007; Elbaz et al., 2007; Noeske et al., 2007; Pérez-González et al., 2008; Dunne et al., 2009; Pannella et al., 2009). The most significant results appear to be that sSFR increases with redshift for all masses and that the sSFR of massive galaxies is lower at all redshifts.

However, there still remains a great amount of uncertainty regarding the exact shape and slope of these relations. Work based on radio stacking analyses of K-band selected galaxies in the redshift range $1.5 < z < 2$ found little or no correlation between sSFR and mass, with some evidence at higher redshifts for sSFR decreasing with increasing mass, and this relationship steepening at higher redshifts still (Pannella et al., 2009; Dunne et al., 2009). In contradiction to this, work using SFR tracers across UV to MIR wavelengths had clear results showing sSFR decreasing with increasing mass (Feulner et al., 2005; Erb et al., 2006; Noeske et al., 2007; Cowie & Barger, 2008). These discrepancies between the estimates using radio data and those using UV to MIR data could, in part, be explained by some of the assumptions and corrections that have to be made in estimating star formation rates from data in the different bands. UV/optical data requires dust extinction corrections, and in using the MIR data to calculate IR luminosity and SED shape, large extrapolations from the $24 \mu\text{m}$ flux have to be made.

New data from the *Herschel* Space Observatory allows for more robust derivation of the IR luminosity of galaxies, as it directly samples the peak of IR emission of

galaxies up to redshifts $z \sim 3$. Recent work by Rodighiero et al. (2010) (hereafter referred to as R10) investigates the relationship between SFR, sSFR and stellar mass, based on PACS observations and ancillary data ranging from the UV to the MIR.

They found that the sSFR-mass relationship was almost flat at redshifts $z < 1$, and that at redshifts beyond this sSFR tended to decrease with increasing mass, with the relation steepening at higher redshifts still. They also found that the mean sSFR of massive galaxies ($M > 10^{11} M_{\odot}$) increases as a function of redshift, out from $z = 0$ to $z = 2$, and that this relationship flattened out beyond $z > 1.5$. Additionally, the most massive galaxies had the lowest sSFR at any redshift, implying that they formed their stars earlier and more rapidly than lower mass galaxies.

In this work I use the model of da Cunha et al. (2008) to obtain median likelihood estimates of SFR, sSFR, stellar and dust mass for my sample of SPIRE 250 μm selected galaxies in the GOODS-N field, the full details of which are described in chapter 3. Using these estimates I investigate how SFR and sSFR vary as both a function of redshift and stellar mass. Additionally, my galaxy sample contains only isolated galaxies, which allows me to separate out the effects of mergers on these observed correlations. Given the mounting evidence (as has been previously described) that the drop in the rate of major mergers is likely not to be the main cause of the decline in SFR for galaxies since $z \sim 1$, I also investigate how SFR and sSFR vary as a function of dust mass - assuming dust mass to be a reasonable proxy for the gas mass of the ISM - in order to determine whether this could explain, at least in part, the cause of this decline.

4.2 The da Cunha et al. (2008) Model

da Cunha et al. (2008) (hereafter referred to as D08) present a model to interpret the MIR/FIR SEDs of galaxies in a manner consistent with their emission at UV, optical and NIR wavelengths. This simple model uses combined UV, optical and IR photometry to compute statistical estimates of the physical parameters of the galaxy, such as star formation rate, stellar mass, dust content and dust properties.

They use the stellar synthesis code of Bruzual & Charlot (2003) to compute the light output by stars in galaxies. The code predicts the spectral evolution of the stellar populations of galaxies from UV to IR wavelengths at ages between 1×10^5 and 2×10^{10} yrs. Calculations are made for a number of different initial mass functions (IMFs) and star formation histories (SFHs).

The attenuation of the starlight is estimated using the two component model of Charlot & Fall (2000), which computes the luminosity absorbed by dust in stellar birth clouds (SBCs) and in the ambient interstellar medium (ISM). This model accounts for the fact that stars are born in dense stellar birth clouds (SBCs) which typically dissipate on timescales of the order of 10^7 yrs. Therefore the light from stars younger than this is more attenuated than that from older stars.

The final part of computing the SED is to determine the distribution of the IR emission from starlight being absorbed and re-emitted by dust in SBCs and the ambient ISM. The IR emission from SBCs is split into three components: the emission from PAHs; the MIR continuum emission from hot dust with temperatures in the range 130 - 250 K; the emission from warm dust in thermal equilibrium with adjustable temperature in the range 30 - 60 K. The IR emission of the ambient ISM is reproduced through fixing the relative proportion of these components and

adding a component of cold dust in thermal equilibrium with adjustable temperature in the range 15 - 25 K .

The model contains a minimum number of adjustable parameters required to account for the observed relations between the observed spectral properties of galaxies: age, star formation history, stellar metallicity, attenuation of dust due to SBCs and the ambient ISM and the four contributors to the total IR emission. A library of model SEDs is built through varying each of these physical parameters and computing the resulting SED from each possible combination. Given an observed galaxy, a likelihood distribution is built for each adjustable physical parameter, based on the how well each model in the library can fit the observed SED. It is in this way the physical parameters are estimated for each observed galaxy.

4.3 Data

For this work - using the D08 model to interpret the observed SEDs of a set of galaxies in terms of statistical constraints on their physical parameters - I used the same sample of SPIRE 250 μm selected galaxies as was described in the previous chapter. This is a clean sample of 74 isolated galaxies with 250 μm flux > 10 mJy, where the optical counterpart of the SPIRE source is clearly and uniquely identifiable and shows no evidence of undergoing a merger.

The D08 modelling is extremely sensitive to having accurate redshift estimates for the galaxy sample. Therefore, I only include sources which have either a spectroscopic redshift, or a photometric redshift estimate less than $z = 2$, as photometric estimates beyond this appear to be less reliable (see figure 3.2 of chapter 3). Including these requirements leaves a sample of 59 galaxies.

The D08 modelling code was run on the complete set of photometry for my galaxy catalogue: GALEX NUV and FUV; KPNO/MOSAIC U band; HST/ACS F435W, F606W, F775W and F850LP; SUBARU/MOIRCS JK bands; Spitzer IRAC 3.5 μm , 4.5 μm , 5.8 μm and 8.0 μm ; Spitzer MIPS 24 μm ; SPIRE 250 μm , 350 μm and 500 μm .

4.4 Results & Discussion

I ran the D08 modelling code over the complete set photometry for each of the 59 sources in my sample with either a spectroscopic redshift or a photometric redshift estimate $z_{\text{phot}} < 2$. Visual examination shows that for chi-squared fits $\chi^2 > 150$ there are extreme outliers in the observed photometry from the best fit SED. Physical parameter estimates from fits worse than this are therefore probably unreliable, so I only include estimates from model SED fits better than this, which results in a set of estimates for 57 galaxies.

Some examples of the best fit model SEDs to the observed photometry of my galaxy set are shown in figure 4.1.

A peculiarity of my results is that a number of galaxies show evidence of being extreme outliers, either with very low star formation rates, or with very low stellar mass. On first inspection it may appear as those these are erroneous results. A likely cause of this could be the method finding multiple solutions with similar probability fits. However, inspection of the probability distributions across the parameter spaces for the outlying results finds that the majority of the results are fairly well constrained, as can be seen in figure 4.2. Therefore it seems that these results may in-fact be reliable.

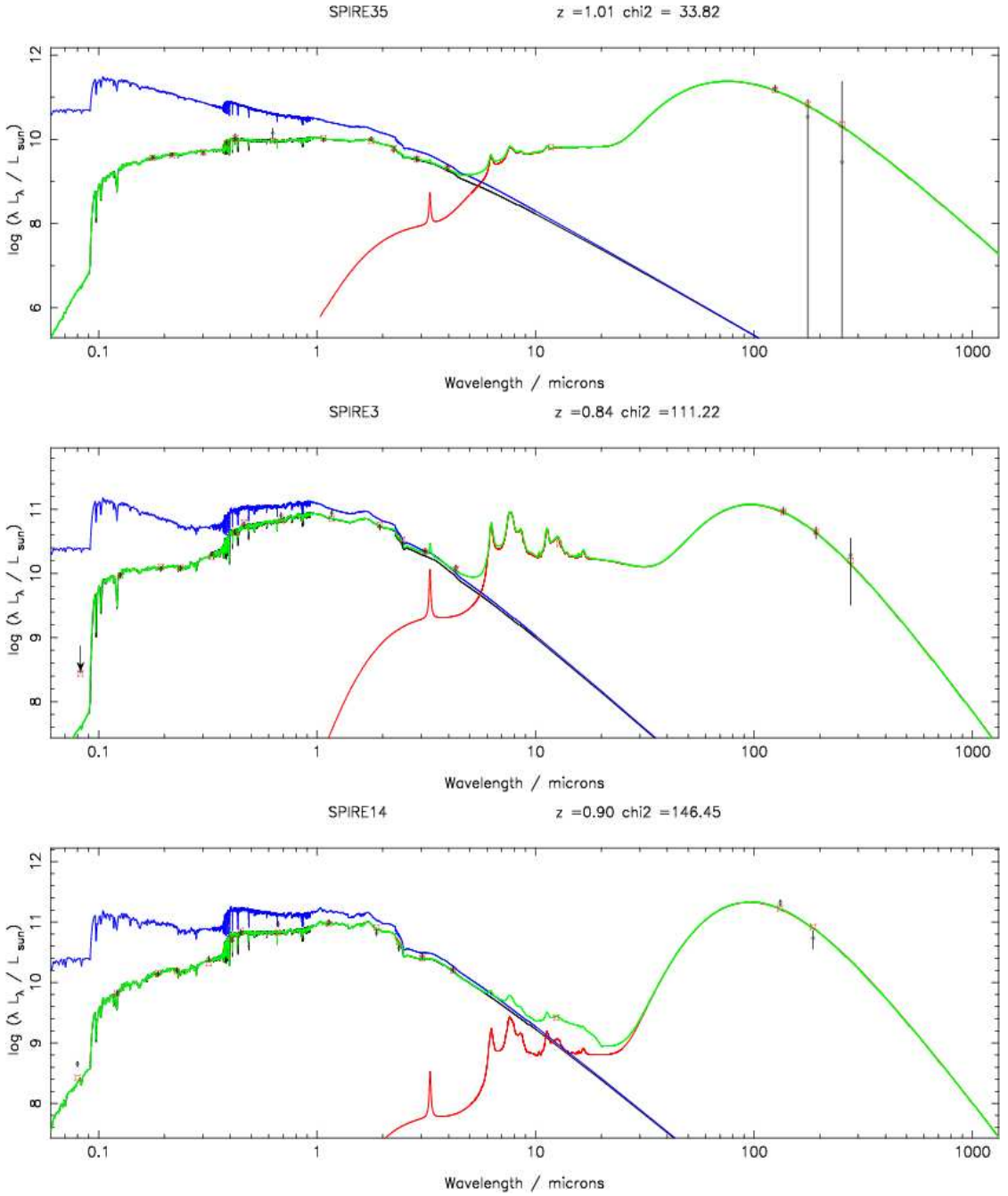


Figure 4.1: Some example best fit model SEDs for my data set. The names of the galaxies, their redshifts (z) and the fits' χ^2 values are given above each plot. The black bars show the observed fluxes and the red boxes show the predicted fluxes from the best fit model SED. The blue line is the unattenuated stellar spectrum, the red line is the emission from dust and the green line shows the total emission from the galaxy (i.e. the sum of the stellar and dust emission).

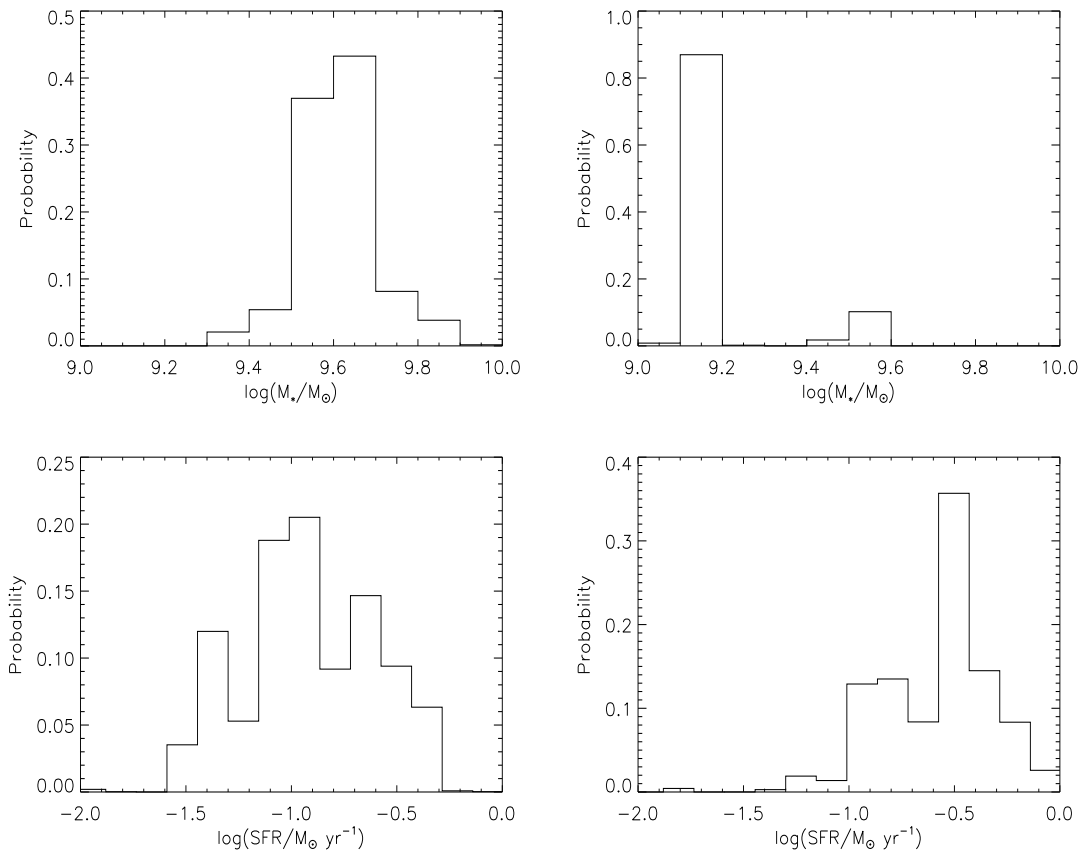


Figure 4.2: Probability distributions for two of the outlying galaxies. Examples are shown for extreme outliers in M_{star} and in SFR.

4.4.1 Star Formation Rate as a Function of Redshift

Figure 4.3 shows how the median likelihood estimates of the SFRs of my galaxy sample vary with redshift. This plot shows a reasonably tight correlation, with SFR increasing with redshift. This is to be expected as, typically, more highly star forming galaxies should be more luminous. As redshift increases the IR luminosity of the galaxies we can detect must increase, therefore their SFR should increase also.

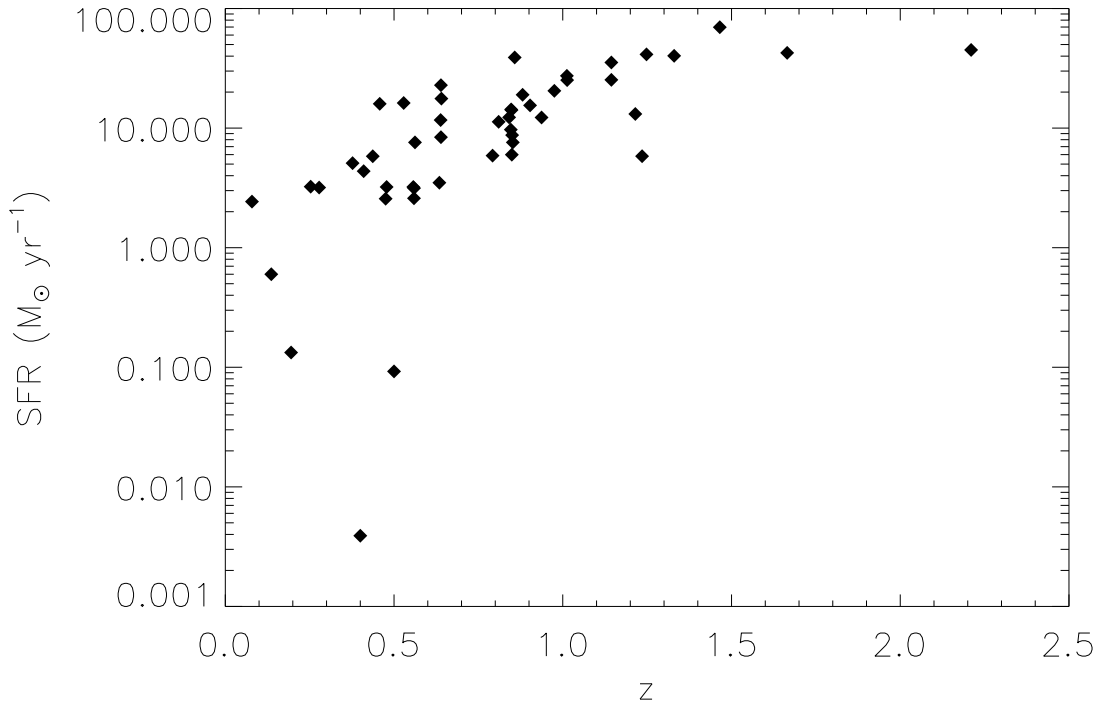


Figure 4.3: Median likelihood estimations of star formation rate (SFR) as a function of redshift (z). Results shown are for the 57 SPIRE galaxies where the best fit SEDs from the D08 modelling fit to the observed photometry with $\chi^2 < 150$.

My SFRs appear to be relatively modest, comparable locally to LIRGs rather than ULIRGs. Comparing these values to those determined for BLAST galaxies (Monceli et al., 2011), the SPIRE galaxy SFRs appear to be approximately an

order of magnitude weaker. However, both these sets of data show a rather large amount of scatter, therefore it is difficult to determine whether or not there is any fundamental difference between the results sets.

Figure 4.4 shows how the median likelihood estimates of the sSFRs of my galaxy sample vary with redshift. The plot shows a weak correlation, with some evidence of sSFR increasing with redshift. Only approximately half of the galaxy sample lie above the $1/\tau$ line (where τ is the age of the universe at that redshift). This implies that only about a half of the galaxies in my sample are undergoing significant bouts of star formation. This is in contrast to the sample presented in R10, which has the majority of their sample lying above this line, implying that the majority of those galaxies are undergoing an era of intense star formation, and that they have built up the bulk of their stellar mass in their more recent past. The relative fraction of galaxies that lie above this line does seem to go up with redshift, but the sample size also drops with this increasing redshift. Therefore I lack a statistically significant enough sample to draw any robust conclusions about the higher redshift galaxies.

4.4.2 Star Formation Rate as a Function of Stellar Mass

Figure 4.5 shows the median likelihood estimates of SFR versus stellar mass for my galaxy sample. The plot doesn't appear to show any clear correlation. This may be explained, at least in part, by the range in stellar mass of my results. For example, the results in R10 offer a range in stellar mass of $\sim 10^9 - 10^{11.5} M_{\odot}$, whereas my own results have a range of $\sim 10^{10} - 10^{11.5} M_{\odot}$, with the majority of sources lying in the range $\sim 10^{10} - 10^{11} M_{\odot}$. Constricting the data in R10 to my own stellar mass range would greatly weaken their evidence for a correlation. Therefore it is not unexpected that my data should not show any clear correlation. Additionally,

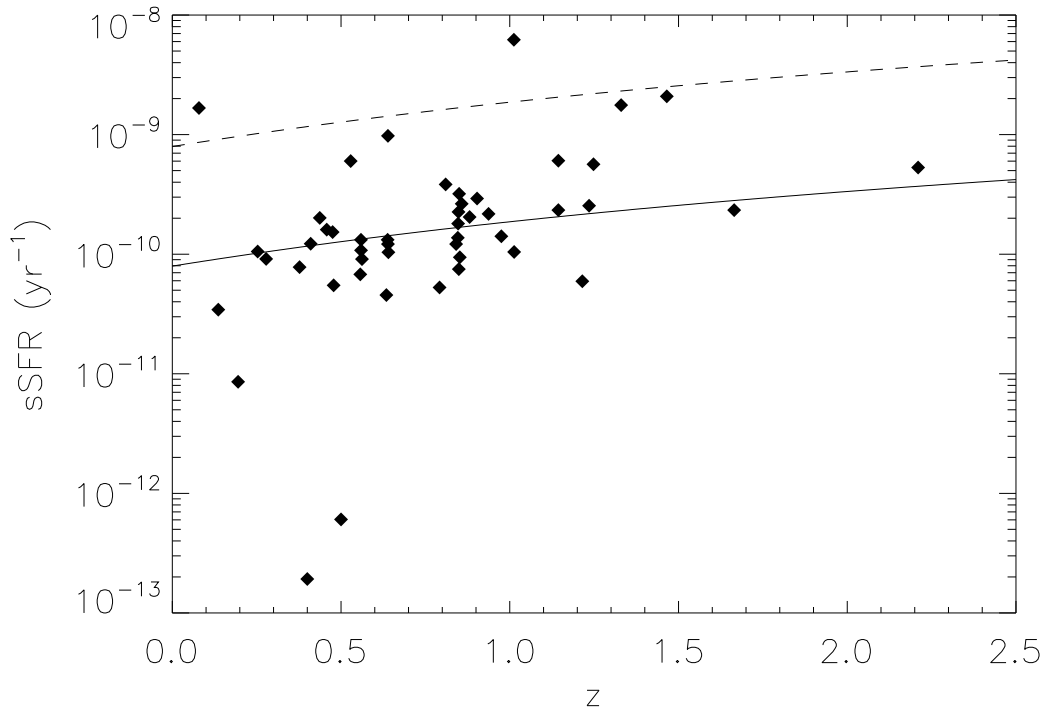


Figure 4.4: Median likelihood estimations of specific star formation rate ($sSFR = SFR/M_*$) as a function of redshift (z). Results shown are for the 57 SPIRE galaxies where the best fit SEDs from the D08 modelling fit to the observed photometry with $\chi^2 < 150$. The solid and dashed lines show $1/\tau$ and $10/\tau$ as a function of redshift, respectively, where τ is the age of the universe at that redshift.

the sample of galaxies in this work (57) is considerably smaller than the sample in R10 (4500). Therefore the lack of a clear result may also just be due to the lack of a statistically significant sample.

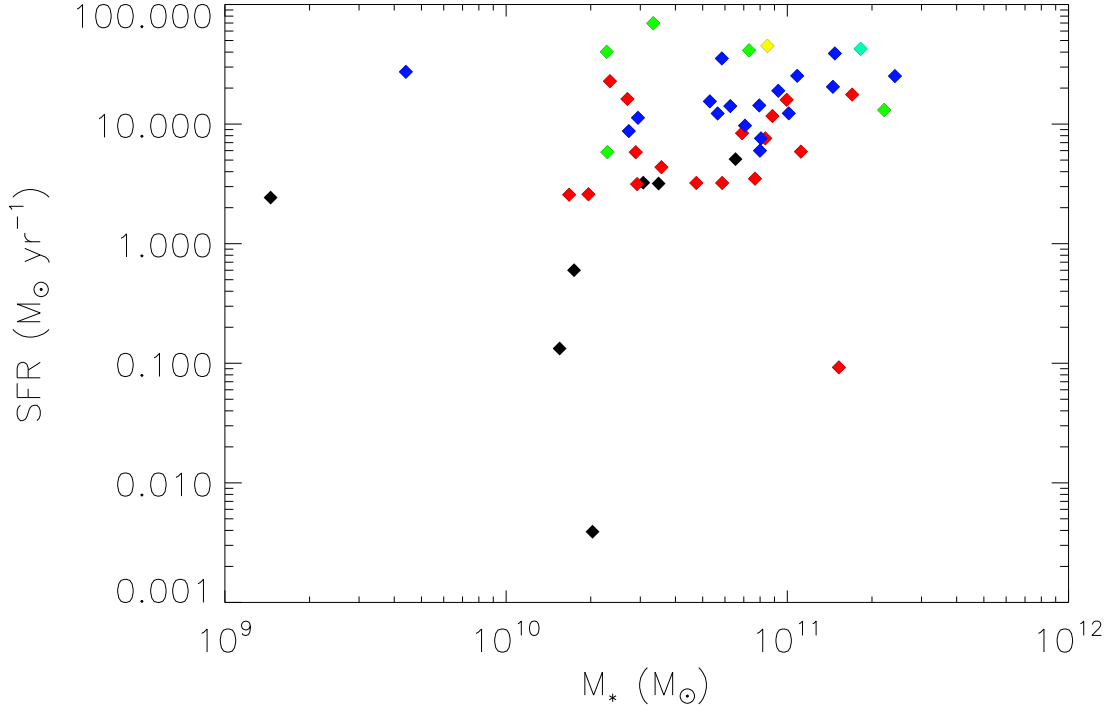


Figure 4.5: Median likelihood estimates of star formation rate (SFR) versus stellar mass (M_*). Results shown are for the 57 SPIRE galaxies where the best fit SEDs from the D08 modelling fit to the observed photometry with $\chi^2 < 150$. Redshift bands $z < 0.4$, $0.4 < z < 0.8$, $0.8 < z < 1.2$, $1.2 < z < 1.6$, $1.6 < z < 2.0$ and $z > 2.0$ are shown in black, red, blue, green, cyan and yellow respectively.

Figure 4.6 shows the median likelihood estimates of sSFR versus stellar mass for my galaxy sample. This plot shows some evidence for a loose correlation between sSFR and stellar mass, with sSFR decreasing with increasing stellar mass, albeit with a large scatter. This is consistent with the results found in R10.

The distribution of sources does not appear to vary with redshift. This implies that across all redshifts, galaxies with larger stellar masses have already undergone the a greater amount of their star formation, which is in agreement with much of the

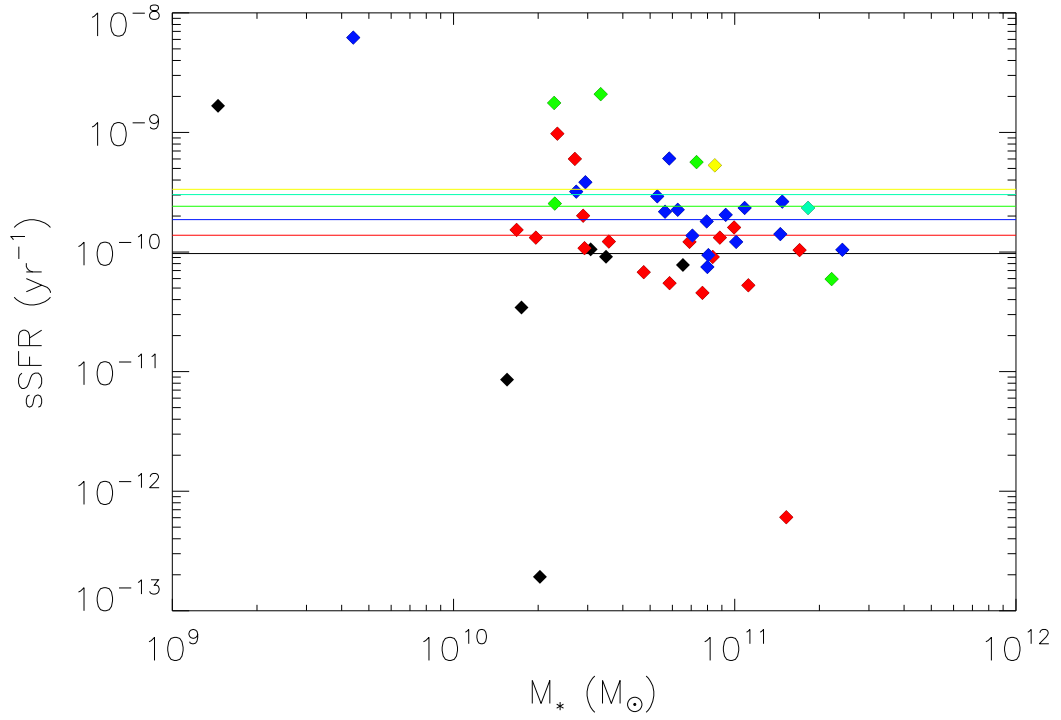


Figure 4.6: Median likelihood estimates of specific star formation rate ($sSFR$) versus stellar mass (M_*). Results shown are for the 57 SPIRE galaxies where the best fit SEDs from the D08 modelling fit to the observed photometry with $\chi^2 < 150$. The horizontal lines show $1/\tau$ for the centre of each redshift band, where τ is the age of the universe at that redshift. Redshift bands $z < 0.4$, $0.4 < z < 0.8$, $0.8 < z < 1.2$, $1.2 < z < 1.6$, $1.6 < z < 2.0$ and $z > 2.0$ are shown in black, red, blue, green, cyan and yellow respectively.

existing literature.

4.4.3 Star Formation Rate as a Function of Dust Mass

As the galaxy sample for this work is a clean set of isolated, non merging sources, it is possible to uniquely test what the origin of the drop in SFR since $z \sim 1$ is, whilst separating out the effect of mergers. This is interesting due to the mounting evidence that the drop in SFR is not primarily due to the corresponding drop in the rate of major mergers (as discussed in chapter 3).

Broadly speaking, the dust content of a galaxy should be roughly proportional to both the column density of gas (e.g., Chini et al., 1986) as well as the metal abundance of the galaxy (e.g., Zaritsky et al., 1994). However, for this work I shall expect the metallicity of the galaxies to only increase the scatter of the distribution. I therefore assume that the dust content of the galaxies should have a reasonable correlation with the gas content of the galaxies.

Figure 4.7 shows the median likelihood estimates of SFR versus dust mass for my galaxy sample. The plot shows some evidence for a scattered correlation, with SFR increasing with increasing dust mass. Thus the decrease in SFR since $z \sim 1$ could be due in part to a decrease in the dust, and therefore gas mass, since that era.

Figure 4.8 shows the median likelihood estimates of sSFR versus dust mass for my galaxy sample. The plot shows a very scattered correlation. This could imply that the dust and therefore gas mass of a galaxy does not tell us anything about when the bulk of the galaxy's stellar population was formed. However, the lack of a statistically significant data set does not allow us to draw any real conclusion

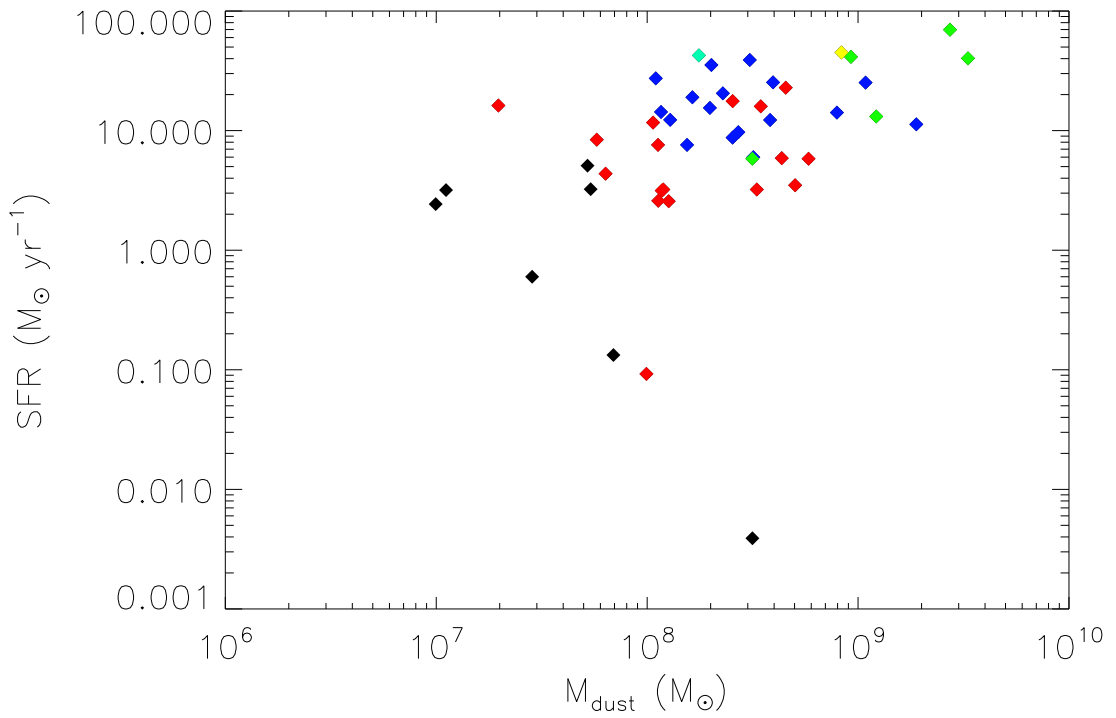


Figure 4.7: Median likelihood estimates of star formation rate (SFR) versus dust mass (M_{dust}). Results shown are for the 57 SPIRE galaxies where the best fit SEDs from the D08 modelling fit to the observed photometry with $\chi^2 < 150$. Redshift bands $z < 0.4$, $0.4 < z < 0.8$, $0.8 < z < 1.2$, $1.2 < z < 1.6$, $1.6 < z < 2.0$ and $z > 2.0$ are shown in black, red, blue, green, cyan and yellow respectively.

regarding the relationship.

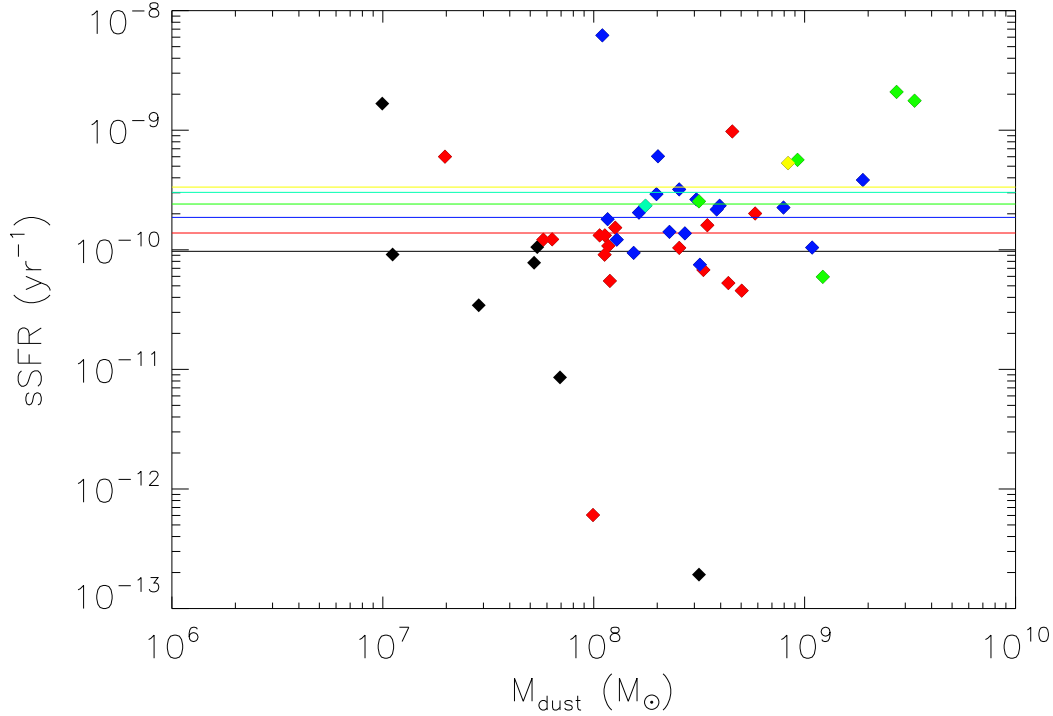


Figure 4.8: Median likelihood estimates of specific star formation rate ($sSFR$) versus dust mass (M_{dust}). Results shown are for the 57 SPIRE galaxies where the best fit SEDs from the D08 modelling fit to the observed photometry with $\chi^2 < 150$. The horizontal lines show $1/\tau$ for the centre of each redshift band, where τ is the age of the universe at that redshift. Redshift bands $z < 0.4$, $0.4 < z < 0.8$, $0.8 < z < 1.2$, $1.2 < z < 1.6$, $1.6 < z < 2.0$ and $z > 2.0$ are shown in black, red, blue, green, cyan and yellow respectively.

4.5 Conclusions

Where any correlation is found, my results agree with the existing literature. I find a weak correlation with $sSFR$ increasing as a function of redshift. The results show some evidence to suggest that the relative fraction of sources with $sSFR > 1/\tau$, i.e. undergoing a more recent burst of star formation, goes up with increasing redshift. This implies that at higher redshifts galaxies were undergoing more recent bursts of

star formation, whereas local galaxies have already formed the bulk of their stellar populations. I also found a loose correlation between sSFR and stellar mass, with sSFR decreasing with increasing mass. This makes sense as it implies that galaxies with more massive stellar populations have already formed the bulk of their star formation, whereas galaxies with less massive stellar populations are still forming stars.

This evidence is agreement with a “downsizing” scenario of galaxy evolution (Cowie et al., 1996). The most massive galaxies in my sample have already undergone the majority of their star formation - implying that they formed at higher redshifts. This is in agreement with my result that the galaxies at higher redshifts are undergoing bursts of more recent star formation, compared to low redshift galaxies which appear to have already formed the bulk of their stellar population.

I do not find any evidence for a correlation between SFR and stellar mass as has been seen in previous work. However, I find no evidence to dispute the existence of a relationship either. This is likely due, in part, both to my results having a small range of stellar masses, as well as the small size of my galaxy sample.

It is possible that some of these SPIRE sources are lensed objects, and that the optical counterparts are therefore miss-identified. A redshift estimate can be determined from the SPIRE fluxes alone, as shown in Amblard et al. (2010). Using the S_{500}/S_{350} and S_{250}/S_{350} flux ratios to estimate redshift, I find that some of the SPIRE sources may be at higher redshifts than given by the optical spectroscopic measurements. Discrepancies in these redshift values could imply that these are lensed objects. Typically, lenses are elliptical galaxies (e.g. Faure et al., 2008), which could explain some of the low SFR estimates.

As my galaxy sample presents a set of isolated, non-merging galaxies, I am also able to investigate the possible causes of the steep decline in SFR since $z \sim 1$ free from the physical effects of merging systems. Assuming that the gas mass of a galaxy correlates reasonably well with its dust mass, I find that SFR appears to increase with gas mass, albeit with a large amount of scatter. Therefore it is possible that the drop in SFR since $z \sim 1$ could be due to a coincident drop in the average gas mass of galaxies since that era.

The *Herschel* Space Observatory allows for a much more robust estimation of the IR luminosity of galaxies than has previously been possible. This in turn allows for more stringent constraints on the SFRs and dust masses of galaxies. Therefore, future *Herschel* surveys, implementing robust methods of determining the physical parameters of the galaxies, should shed much more light on the true nature of the physical processes controlling galaxy formation.

Chapter 5

The Effectiveness of MIR/FIR Blind, Wide Area, Spectral Surveys in Breaking the Confusion Limit

The work presented in this chapter has been previously published as Raymond et al. (2010).

5.1 Introduction

Source confusion may be defined as the degradation of the quality of photometry of sources clustered on a scale to the order of the telescope beam size (e.g. Scheuer (1957)). The confusion limit sets the useful depth to which large-area extra-galactic

surveys should be taken. For example, the *Herschel* mission (Pilbratt, 2004), successfully launched in May 2009, has a 3.5 m diameter mirror which realizes an angular resolution of 8'' at 120 μm . At these wavelengths, the confusion limit for such a mirror is estimated to be around $\sim 5 \text{ mJy}^1$ (e.g. Dole et al., 2004; Jeong et al., 2006)). Surveys at 24 μm suggest that at these flux levels one will only be able to resolve at most $\sim 50\%$ of the CIB (Dole et al., 2004). It is possible to reduce the confusion limit through making observations with a larger diameter mirror. However, due to the practical limitations of high angular resolution FIR imaging there is a limit on how much one can reduce confusion noise.

One way to break through the confusion limit makes use of the extra dimension of wavelength, to which one has access in spectroscopic surveys. Discrete sources can be identified by relatively bright, narrow-band emission lines; thereby allowing redshifts to be determined. A preliminary study to explore the efficacy of blind, wide area spectroscopic surveys in resolving FIR sources is described in Clements et al. (2007) (hereafter referred to as CO7). In their work an artificial ‘sky’ was populated using template FIR SEDs of a selection of different types of galaxy, to which were added FIR emission lines of strengths derived from ISO-LWS observations (e.g. Negishi et al., 2001). The sources were redshifted and assigned luminosities according to the evolutionary models of Pearson (2005), Pearson et al. (2007) and Pearson & Khan (2009). Observations of the ‘sky’ were made using the instrumental parameters (e.g. sensitivity/noise levels, spectral resolution, FoV, beam size) of SAFARI (SpicA FAR-infrared Instrument), a FIR imaging Fourier Transform spectrometer concept for the proposed JAXA-led SPICA (Space Infrared Telescope for Astronomy and Astrophysics) (Nakagawa, 2010) mission. It will offer the large FoV and high spectral resolution required to break the confusion limit using

¹The confusion noise for *Herschel*’s SPIRE instrument has now been measured to be 5.8 mJy/beam at 250 μm (Nguyen et al., 2010).

spectroscopy. According to its current specifications (see appendix A) SPICA will have a 3.2 m diameter mirror, and therefore will be subject to approximately the same confusion noise as *Herschel*. The primary mirror will, however, be cooled to <6 K and so will offer a great leap in sensitivity over *Herschel*. SAFARI will cover the waveband 35 to 210 μm with varying resolving power, including $R \sim 1000$ - (at 120 μm , $\Delta\lambda = 0.176 \mu\text{m}$) - which matches the typical width of an extragalactic MIR/FIR emission line. However, the work presented in C07 assumed the original specifications of SPICA/SAFARI which has a dish size of 3.5 m and a waveband of 30 to 210 μm , with a 5σ 10 hour sensitivity of 1.7 mJy.

C07 made estimates of source redshift by eye, by locating the position of the strongest emission line in each spectrum. The strongest lines typically observed in the FIR are the [OI] and [CII] lines at 63.18 and 157.74 μm respectively. If one assumes a typical dust temperature of 35 K, then the strongest lines shortward and longward of the peak of the SED will be [OI] and [CII] respectively (the limiting temperatures where this is no longer true being 18 and 46 K), as is illustrated in the example spectrum shown in figure 5.1. Beyond $z = 2.5$ these lines are shifted out of SAFARI's waveband, therefore the redshifts of more distant sources than this cannot be retrieved using these lines alone. If the only emission lines present were the ones in the FIR, then by comparing the evaluated source redshifts with the model input redshifts one can assess the efficiency of this blind-line method. C07 found that when looking at a patch of simulated 'sky' equal to one SAFARI FoV, it was possible to retrieve accurate redshifts for sources with 120 μm continuum fluxes as much as a factor of ~ 10 below the traditional continuum confusion limit. Sources with 120 μm flux $S_{120\mu\text{m}} > 1$ mJy and at redshifts $z < 2.5$ were retrieved with 100% accuracy.

The use of blind spectral line surveys to resolve FIR sources is not without its

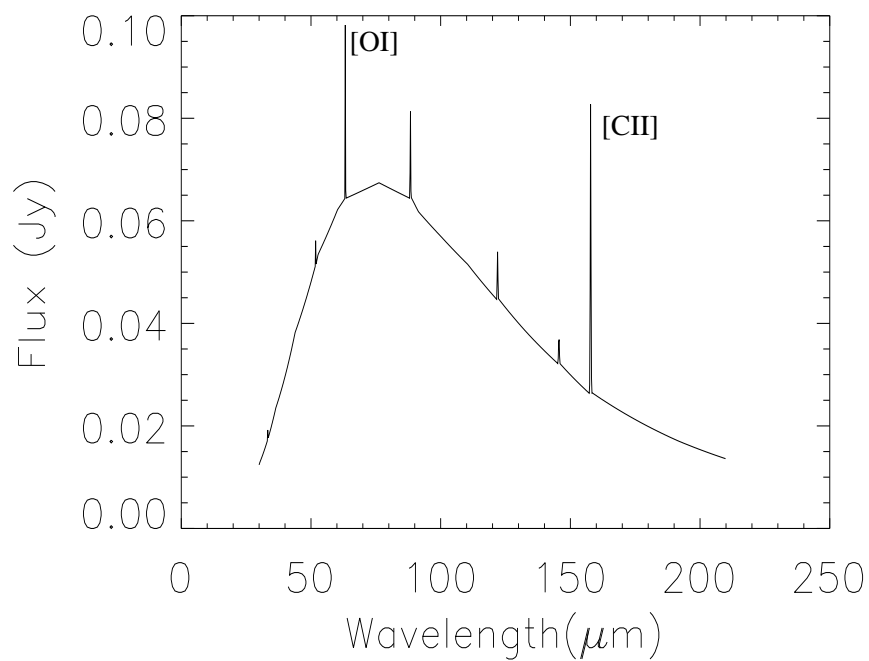


Figure 5.1: An example spectrum with an approximate dust temperature of 35K, with the strong [OI] and [CII] lines shortward and longward of the SED peak, respectively.

own limitations and type of confusion. Line, or spectral confusion occurs when multiple sources are observed in a single telescope beam: the spectra from two or more objects are effectively scrambled, and it can become difficult to determine which lines are emitted by which objects. As a result, source redshift estimations can become inaccurate. The work described in C07 made use of model spectra with FIR emission lines only. To assess the true viability of using spectral line surveys to break through the confusion limit requires the inclusion of MIR emission lines in the ‘sky’ model, as sources will, in general, have both FIR and MIR emission lines. Inclusion of these shorter wavelength lines will enable the recovery of sources with redshifts of $z > 2.5$, beyond which the [OI] and [CII] emission lines at 63.18 and 157.74 μm , respectively, are shifted out of the SAFARI waveband. By including MIR lines, however, one increases the problem of line confusion, and so assigning lines to individual, but spatially unresolved, sources becomes more problematic.

In this chapter I examine a much larger model ‘sky’ populated with more realistic template spectra with both FIR and MIR emission lines and employ a new automated method of evaluating source redshifts in a time efficient manner. I also implement a method to extract the redshifts of multiple sources clustered in a single spatial bin. Through the implementation of this method I investigate how effectively I can break through the traditional photometric confusion limit.

5.2 Extracting Redshifts From an Artificial Sky

Deep, blind-field imaging spectroscopy could potentially enable discrete sources, at fluxes below the traditional continuum confusion limit, to be extracted. Using imaging spectroscopy, it is theoretically possible to extract redshifts for all

sources (with emission lines) present in the instrument’s FoV, allowing all sources to be discretely resolved, as long as the instrument is sufficiently sensitive. In this work this is done using an automated redshift-determination algorithm. In order to best test the efficiency (number of sources for which I determine redshifts, inversely weighted by how many sources I inaccurately determine redshifts for) of this method I generate an artificial sky in the form of a datacube, populated with realistic spectra taken from nearby galaxies, and redshifted according to the bright-end and burst mode galaxy evolution models of Pearson (2005), Pearson et al. (2007) and Pearson & Khan (2009). Running the program through the datacube I compare the fitted redshifts with their input values in order to determine the method’s precision, accuracy and efficiency.

5.2.1 Generating an Artificial Sky

I create an initial set of two 1 square degree artificial skies with 1” spatial resolution, populated by galaxies with redshifts, spectral types and 40 μm continuum fluxes based on the bright-end and burst mode evolutionary models of Pearson (2005), Pearson et al. (2007) and Pearson & Khan (2009). I do not include any physically based spatial distribution modelling (e.g. clustering, etc.) and in this work the skies are populated with sources uniformly distributed in random positions. It should also be noted that I do not include any cirrus contribution. These cubes act as my master ‘skies’ which I later crop and re-bin to create the SAFARI footprints.

The bright-end and burst mode evolutionary models are backward evolution formulations where observed galaxy source counts are used to constrain the model parameters. The model components consist of a luminosity function to represent the number density of sources as a function of luminosity, a library of SEDs to

model the extragalactic source population emission as a function of wavelength and an assumption on the type-dependent evolution of the extragalactic population (in luminosity and number density). Both evolutionary models utilize the IRAS infrared local luminosity function defined at $60\mu\text{m}$ (Saunders et al., 2000) or $12\mu\text{m}$ (Rush et al., 1993) for the galaxy and AGN (Seyfert) populations respectively. Although various other, more recent luminosity functions are available, the IRAS functions have the advantage of being defined at or around the peak of the population emission spectrum and are free of contamination by mid-infrared features. The $60\mu\text{m}$ galaxy luminosity function is segregated into cool (normal galaxy) and warm (star-forming) components, defined by *IRAS* colours where cool $100\mu\text{m}/60\mu\text{m}$ cirrus-like colours (Efsthathiou & Rowan-Robinson, 2003) represent the normal quiescent galaxy population and the warmer $100\mu\text{m}/60\mu\text{m}$ colour component is representative of star-forming galaxies with activity increasing as a function of luminosity for M82-like Starburst $L_{IR} < 10^{11}L_{\odot}$, luminous (LIRG) $L_{IR} > 10^{11}L_{\odot}$ and ultraluminous (ULIRG) $L_{IR} > 10^{12}L_{\odot}$ infrared galaxies. Thus the model framework includes five general evolutionary population classes (Normal, Starburst, LIRG, ULIRG, AGN) of extragalactic object defined by luminosity, colour and subsequent evolution.

The bright-end model assumes evolution in the galaxy population in both density and luminosity, modeled by simple power laws of the form $f(z) = (1+z)^k$, where k is the type dependent evolutionary strength parameter. The evolutionary model is an updated framework of that first presented in Pearson & Rowan-Robinson (1996), with modest starburst galaxies rather than ULIRGs dominating in $15\mu\text{m}$ selected source counts. The burst mode evolutionary model predicts that the upturn of emission at $15\mu\text{m}$ (Elbaz et al., 1999) and peak at $24\mu\text{m}$ (Papovich et al., 2004) is to due the emergence of a new population of U/LIRGs. The original burst mode

evolutionary model presented by Pearson (2001) has power law evolution similar to the bright-end model for the starburst and AGN sources and an initial violent exponential evolutionary phase of the form, $f(z) = 1 + f.exp[-\frac{(z-z_p)^2}{2\sigma^2}]$, from $z = 0$ to $z_p = 1$, where k and σ are the type dependent evolutionary strength parameters, followed by a power law evolutionary phase for the U/LIRGs. Both the bright-end and burst mode evolutionary models have non-evolving normal galaxy populations. Throughout this work, values regarding the different evolution models are written in the form bright-end(burst mode).

Each of the five general evolutionary population components (Normal, Starburst, LIRG, ULIRG, AGN) are represented by a small set of galaxy spectral energy distributions from the libraries of Efstathiou & Rowan-Robinson (2003), Efstathiou et al. (2000) and Efstathiou & Rowan-Robinson (1995) for the normal, starburst, U/LIRG and AGN types respectively. The selected SEDs are representative of the SED libraries from which they have been drawn and have been shown to be consistent with the colours of sources detected in the European Large Area ISO Survey (Oliver et al., 2000). Rowan-Robinson et al. (2004) showed that the ISO infrared galaxy population could indeed be divided into four general spectral classes: normal quiescent galaxies; starburst (M82-like) galaxies; luminous and ultraluminous infrared galaxies (which in this work have been taken to be two separate spectral classes) and AGN. Rowan-Robinson et al. (2004) found that the normal, quiescent population of ISO galaxies were well modelled with the templates of Efstathiou & Rowan-Robinson (2003), with far/mid-infrared ratios of $\nu S_\nu(100\mu\text{m})/\nu S_\nu(12\mu\text{m}) \sim 6 - 7$ whilst in contrast, IRAS galaxies were often modelled with templates with ratios of ~ 5 (Rowan-Robinson & Crawford, 1989). Therefore, the normal galaxy component of the population consist of 2 SEDs each of $\nu S_\nu(100\mu\text{m})/\nu S_\nu(12\mu\text{m}) \sim 5.8$ and 6 referred to as a normal and cold normal

type respectively. For the star forming population (e.g. starburst, U/LIRG) 7 SEDs were selected from the template libraries to ensure a variation in the the mid-infrared features in an attempt to avoid artefacts caused by a particular choice of SED for all sources. The SEDs in the template libraries have a broad correlation between model optical depth and galaxy luminosity. 2/7 of these SEDs are selected for the starburst component ($\tau_V \sim 50$ of which one is a model for the archetypal star-forming galaxy M82). 3/7 of these SEDs are selected with increasing optical depths ($\tau_V \sim 50-100$) for the LIRG component (assuming a corresponding increase in luminosity for each SED of $10^{11}L_\odot$, $10^{11.5}L_\odot$ and a colder SED of $L > 10^{11.5}L_\odot$ referred to as a cold-LIRG) and the remaining 2/7 SEDs selected for the ULIRG component correspond to the best template model fits for the archetypal ULIRGs Arp220 (cold ULIRG) and Mk231 (hot ULIRG) respectively. Given the relatively featureless infrared spectra of AGN, the AGN component SED corresponds to a single tapered disc dust torus model. Emission lines are then added to each of the template spectra, taken from ISO-LWS observations of nearby galaxies (e.g. Negishi et al., 2001).

I use the same FIR emission line strengths as were used in C07. MIR emission line strengths are taken, where possible, from the same sources as are used for the FIR emission lines. In some cases data were not currently available at these shorter wavelengths, in which case sources with similar FIR characteristics as the original template spectra are used. The galaxies from which I take the MIR emission line strengths are listed in table 5.1. The model spectra are shown in figure 5.2 and are added to the master ‘sky’ at a spectral resolution of $\Delta\lambda = 0.08 \mu\text{m}$ ($R = 2500$ at $200 \mu\text{m}$) in the waveband from 1 to $400 \mu\text{m}$. As per the method used in C07, it was assumed that an emission line would fit into a single spectral channel. However, when re-interpolating a spectrum from the native resolution of the master ‘sky’

into the lower resolution of a SAFARI observation, a situation sometimes occurs where an emission line is spread over more than once channel.

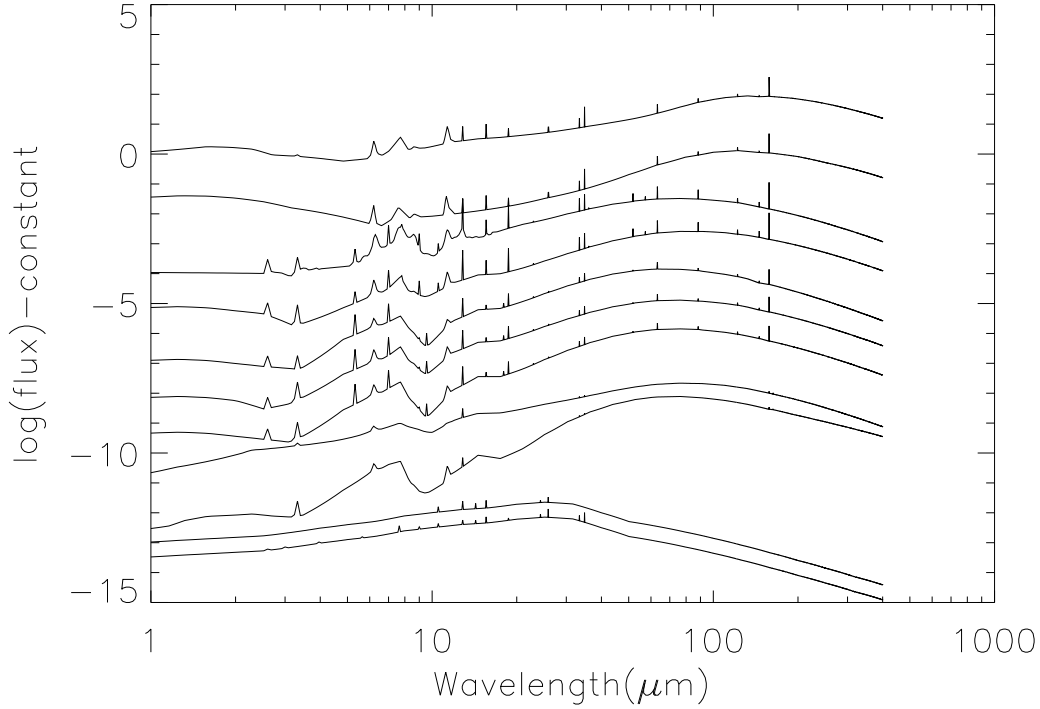


Figure 5.2: Template spectra which were used to populate the datacube. From the top downwards are the SED templates for: normal cold, normal, starburst M82, starburst, $10^{11}L_{\odot}$ LIRG, $10^{11.5}L_{\odot}$ LIRG, cold LIRG, hot ULIRG, cold ULIRG, Seyfert 1 and Seyfert 2.

The flux and redshift distributions for each SED type for the bright-end and burst mode evolution models are shown in figure 5.3. These figures show the distribution of SED type with $120\mu\text{m}$ flux² and redshift over a 1 square degree region of sky. In these regions of sky there are a total of 25596(38975) sources with $S_{120\mu\text{m}} > 0.342\text{ mJy}$ ³ (the 1σ , 10hr sensitivity of SAFARI in its original specifications). Of these sources 33(58)% have $S_{120\mu\text{m}} > 1\text{ mJy}$. The burst mode evolution

²Throughout this chapter, the $120\mu\text{m}$ flux is used for the purposes of comparison etc., as it is the central wavelength of the SAFARI waveband.

³The reason this flux value is used for comparison purposes is explained in the results section of the chapter.

Component	Galaxy Type	Line Template	Reference
Normal	Cold/Normal	NGC 7331	Smith et al. (2004)
Starburst	M82/Starburst	M82	Förster Schreiber et al. (2001)
LIRG	$10^{11/11.5} L_{\odot}$ /Cold LIRG	NGC 253	Sturm et al. (2000)
ULIRG	Hot/Cold ULIRG	Arp 220	Sturm et al. (1996)
AGN	Seyfert 1	Mrk 1014	Armus et al. (2004)
AGN	Seyfert 2	NGC 1068	Lutz et al. (2000)

Table 5.1: Sources used for the addition of MIR lines to the template spectra that populate the data cube.

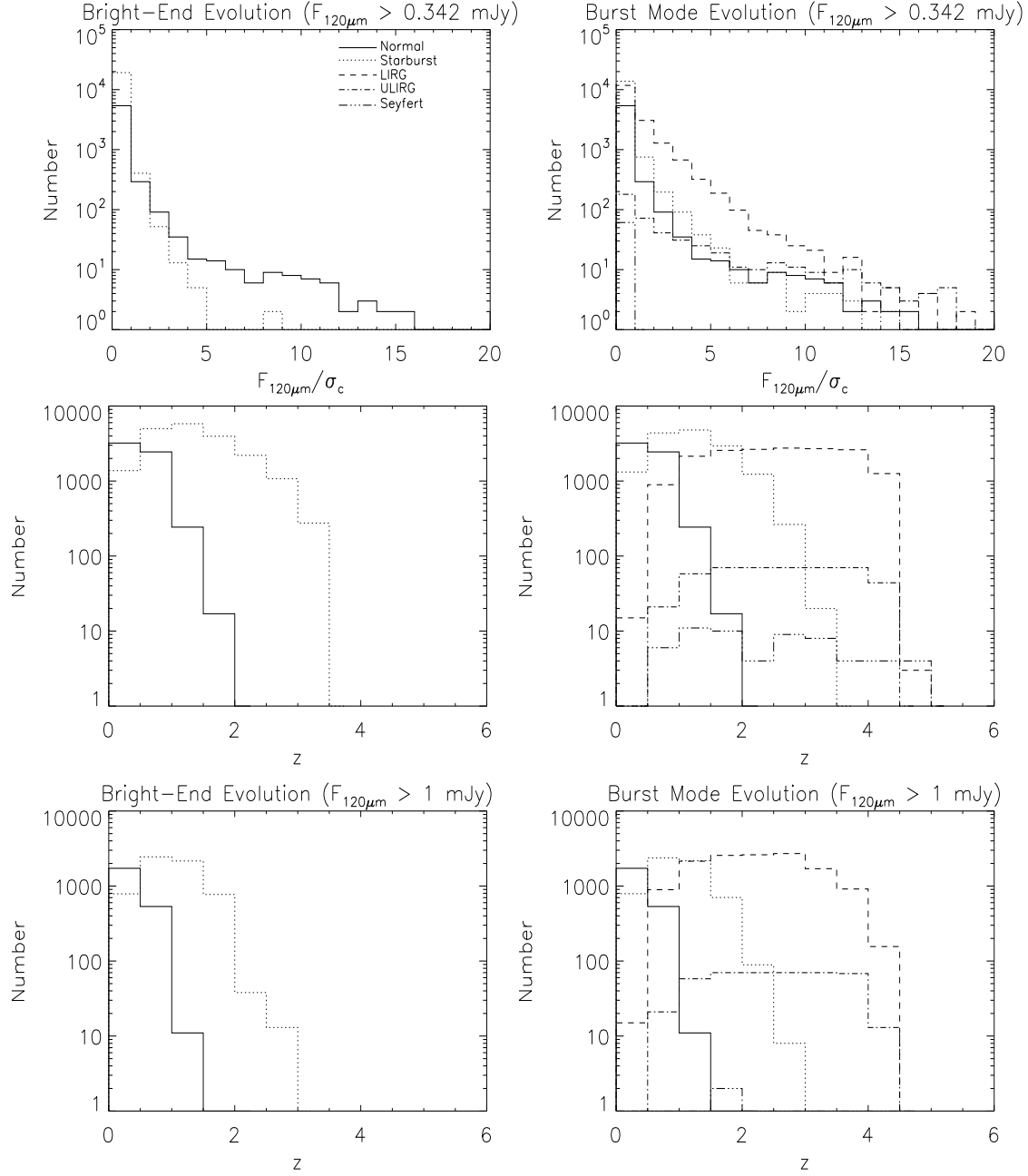


Figure 5.3: A plot of the flux (top row) and redshift (bottom two rows) distributions, for each SED type, of the sources that populate the bright-end and burst mode evolution data cubes respectively. The top two rows are for sources with $120\ \mu\text{m}$ flux, $S_{120\mu\text{m}} > 0.342$ mJy and the bottom row is for sources with $S_{120\mu\text{m}} > 1$ mJy. Values are for a 1 square degree region of sky. Flux is measured as a fraction of the $120\ \mu\text{m}$ confusion limit, $\sigma_c = 4.3$ mJy

model includes more high flux sources as well as more high redshift sources than the bright-end model. The burst mode model also includes the more extreme luminous/ultraluminous and Seyfert spectral types, which tend to dominate at higher redshifts. 100(75)% of sources with $S_{120\mu m} > 1$ mJy have redshifts $z < 2.5$, however setting $S_{120\mu m} > 0.342$ mJy these values drop to 95(74)%.

5.2.2 Generating Datacubes/Source Catalogs

In this chapter I assume the original specifications of SAFARI, which has a $2' \times 2'$ FoV with a diffraction-limited angular resolution of $8''$ at $120 \mu m$. According to its current specifications the instrument will cover the waveband from 35 to $210 \mu m$ at varying spectral resolution ($R \sim 1000$ at $120 \mu m$). However, in this work, in order to compare my results to those of C07, I use the original waveband covering from 30 to $210 \mu m$. In order to ease computations I also assume a slightly larger FoV of $128'' \times 128''$. Thus to generate datacubes representative of the sky as would be seen by SAFARI I take $128'' \times 128''$ sections of my artificial skies and re-bin to a angular resolution of $8''$ (to simplify I have assumed a wavelength independent angular and spectral resolution). This re-binning allows for the possibility of two or more sources in a single spatial bin. In these cases I refer to the brightest source with $S_{120\mu m} > 0.342$ mJy as the primary source and the second brightest source also with $S_{120\mu m} > 0.342$ mJy as the secondary source. Assuming the angular resolution of SAFARI means that 6(8)% of all pixels have two or more sources present. If there are multiple sources present in a spatial pixel only the two brightest will be investigated as examination of the evolutionary models shows that the vast majority of other sources will be too faint relative to the primary and secondary sources to detect. I create the spectra by cropping the waveband of the artificial

sky to between 30 and 210 μm with and smoothing them to a fixed resolution of $\Delta\lambda = 0.176 \mu\text{m}$ (assuming a constant spectral resolution matched to SAFARI's resolving power of $R = 1000$ at 120 μm). As I use the original wavelength range SAFARI, rather than its current specification, I have a slightly larger waveband to pick up emission lines from. I then add Gaussian noise with a standard deviation of $\sigma = 0.342 \text{ mJy}$ and a zero mean along each spectrum⁴. A datacube representing a single SAFARI footprint is therefore 16x16x1024 pixels in size.

A 'truth' catalog is simultaneously generated which tracks the location of each source in a datacube, as well as the redshift, SED type and 120 μm flux. This allows a later comparison between input redshift and those retrieved using my redshift estimation algorithm. This is the same method by which the datacube and 'truth' catalog were generated by C07.

Datacubes are generated for both burst mode and bright-end evolutionary models. For each evolutionary model 100 different datacubes are investigated (i.e. taken from different regions of the larger 1 square degree cube) in order to account for variance in the random spatial distributions, each of a size equivalent to $128'' \times 128''$. For each cube the noise ($1\sigma = 0.342 \text{ mJy}$) along the spectra is added by creating 10 differently seeded randomly generated Gaussian noise arrays in order to account for the variance of results due to noise. I therefore have a total of 1000 datacubes for each evolutionary model. By way of comparison, a figure of $\sigma_c(\lambda = 120 \mu\text{m}) = 4.3 \text{ mJy}$ is adopted for the confusion limit, based on Dole et al. (2004), assuming 20 beams per source.

⁴The is the 1σ noise value commensurate with the original sensitivity of SAFARI, for a 10hr integration time.

5.2.3 Detecting Sources and Extracting Their Redshifts

Redshifts are determined using a pseudo-cross-correlation (PCC) method and stored - however, first the presence of a source must be confirmed. This is done by checking the 120 μm flux, $S_{120\mu\text{m}}$, of each spatial pixel in the cube against a limiting value. This action is performed before any other operations take place, thereby saving processing time on analysing non-existent or too-faint sources. I assume that if any spatial pixel has $S_{120\mu\text{m}} > 0.342$ mJy then a source is present and I attempt to determine its redshift. This was chosen as my continuum cutoff value as empirically⁵ it is found that if a source has 120 μm flux less than this then typically the emission lines are too faint to reliably use with the PCC method. A flow diagram illustrating the sequence of this method is shown in figure 5.4.

Each spectrum is preprocessed prior to redshift-determination in the following way:

a) Each spectrum is fit with a fourth order polynomial which is taken to represent the continuum emission of the source; b) the $S_{120\mu\text{m}}$ value of the spectrum is checked against a limiting value: if $S_{120\mu\text{m}} <$ the limiting value, the source is considered too faint to determine its redshift, and no further analysis is conducted on the spectrum; c) The polynomial continuum fit is subtracted from the spectrum, leaving an array containing only emission lines and noise (see figure 5.5). The 6 highest channels (with $S_\lambda > 2\sigma$) in the array are then initially considered to be emission lines and are taken to be the observed lines in my observed line array (*OLA*). Empirically it has been found that if the ratio of the strongest to weakest (continuum subtracted) line fluxes present in *OLA* is less than 1.5 then these lines most likely arise from noise and I therefore consider such an array to contain no genuine emission lines. Further analysis is only conducted on spectra with higher

⁵Wherever a value has been determined empirically, it has simply been determined via numerous iterations of variations of the code, as being the value which most favourably effects the results.

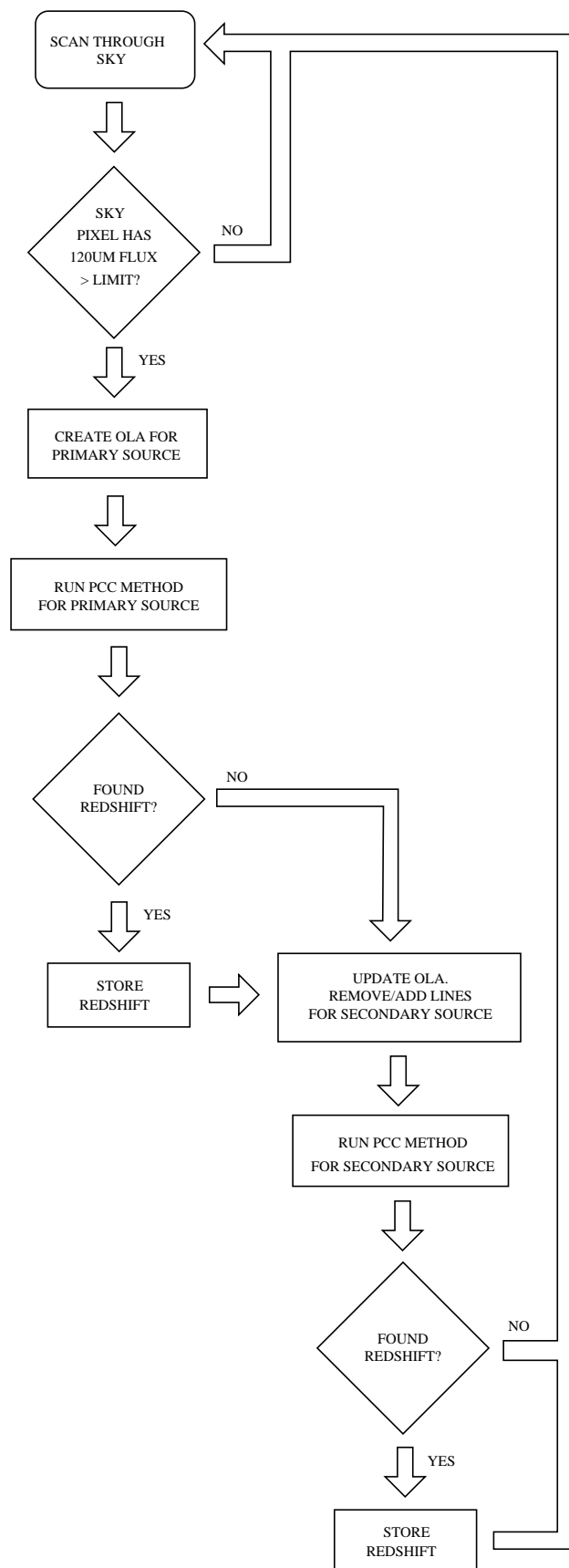


Figure 5.4: A flowchart of the order in which the sources are observed and then the redshift-determination method implemented.

ratio values than this.

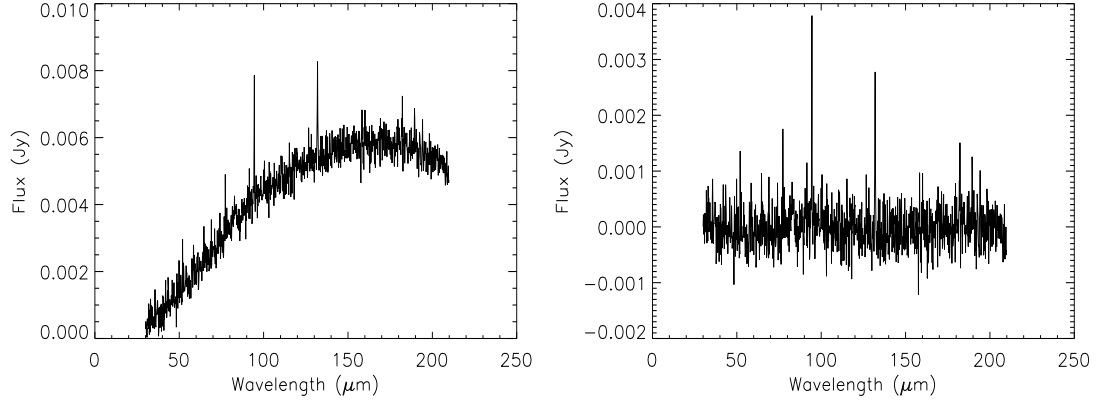


Figure 5.5: Shown in the left panel is a sample spectrum as can be found in my artificial ‘skies’. In the PCC redshift determination algorithm the continuum of this spectrum is fit with a fourth order polynomial. This fit is then subtracted from the spectrum, leaving an array containing only emission lines and noise. The right panel shows the example spectrum after the continuum fit has been subtracted.

OLA is 1024 spectral channels in extent (i.e. identical to the spectral extent of my data cube), and contains the continuum-subtracted flux of the 6 observed possible emission lines at the appropriate spectral channels corresponding to the wavelengths of those lines, and zero elsewhere. In the case of an emission line stretching across multiple pixels, the line is compressed into a single channel and there is a built in tolerance in the redshift fitting routine to allow for this. The brightest channel present in *OLA* is assumed to hold a genuine emission line. The wavelength of this emission line is then compared to the set of template wavelengths compiled from a list of the strongest emission lines typically seen in galactic spectra in the MIR/FIR. This template line array (TLA) is equal to one at the appropriate spectral channels corresponding to the wavelengths of the template emission lines, and zero elsewhere. This comparison then provides a table of possible redshifts the source may lie at.

If the strongest line in *OLA* lies at $\lambda_{\text{brightest}}$, and the template emission lines lie at

wavelengths $\lambda_{template_j}$, where j is the indexing of the line in the template (e.g. for [OIII]@51.82 μm $j = 1$, for [NIII]@57.32 μm $j = 2$ etc.), then an array of possible redshifts at which the source may lie can be determined from:

$$z_k = \frac{\lambda_{brightest}}{\lambda_{template_j}} - 1 \quad (5.1)$$

Where $k = 1, 2, \dots, l$, where l is the total number of lines in TLA and thus the total number of possible redshifts. The array of template emission lines, TLA , which was used to determine the set of possible redshifts is now also used to fit to the observed possible emission lines, OLA . Thus in order to find the redshift at which TLA most closely matches OLA , TLA is shifted to each of the possible source redshifts, as in;

$$\lambda_{template_{jk}} = \lambda_{template_j}(1 + z_k) \quad (5.2)$$

I now have l binary redshifted template line arrays (TLA_k), each of which are 1024 spectral channels in extent and are defined by;

$$(TLA)_{ik}(\lambda_i = \lambda_{template_{jk}}) = 1 \quad (5.3)$$

$$(TLA)_{ik}(\lambda_i \neq \lambda_{template_{jk}}) = 0 \quad (5.4)$$

where i is the spectral channel corresponding to a given wavelength. The strength of the correlation between the observed line array and each template line array is given by;

$$C_k = \sum_{i=0}^{i=1023} (OLA)_i (TLA)_{ik} \quad (5.5)$$

The value of z_k which gives the highest value of C_k is then assigned as the best estimate of the source redshift. In this way the strength of the match depends

both on the strength of the continuum subtracted emission lines that are coincident between the observed spectrum and the redshifted line templates, and the number of matches between lines of the observed and template emission line arrays.

To improve the accuracy of the PCC method, use is made of additional, a-priori information (determined from a visual inspection of the model spectra). Redshifts which produce template/observed array emission line matches for strong, commonly observed emission line pairs are weighted more heavily. The additional weighting values for C_k when a characteristic pair is found are determined empirically to give the most favourable ratio of accurate to inaccurate source redshift evaluations⁶ ⁷. E.g. one of the strongest line combinations in the MIR is the [SIII]/[SiII] pair at rest wavelengths of 33.42 and 34.82 μm respectively. If a match is made between the observed line array and this line pair, then C_k is weighted by an extra factor of 2. Two other, weaker, line combinations included in my template array are the [OIII]/[NIII] and [OIII]/[NII] pairs at rest wavelengths of 51.82, 57.32, 88.36 and 121.90 μm respectively. If a match is made between the observed line array and either of these line pairs, then C_k is weighted by an extra factor of 1.5.

I include an additional criterion (which, again, have been found empirically to improve the efficacy of the PCC method) that, as the strengths of the members of the [OIII]/[NIII] and [OIII]/[NII] lines pairs are typically comparable, any value of z_k which gives a match in the observed line array with one member of either of these pairs, but not its partner, is rejected. This relationship holds for all the

⁶An evaluated source redshift is defined as being accurate if it differs from the input model redshift by less than 0.1, i.e. $|z_{\text{evaluated}} - z_{\text{catalog}}| = \Delta z < 0.1$

⁷Taking as an example three different weighting values: A , B and C . A outputs 3 accurate redshifts and 0 inaccurate redshifts. B outputs 20 accurate redshifts and 10 inaccurate redshifts. C outputs 15 accurate redshifts and 3 inaccurate redshifts. Of these weighting values I would use C as this outputs a high number of accurate redshifts, while limiting the number of inaccurate redshifts.

model spectra used in this work, however it may not always hold in practice when encountering genuine spectra as observed in extragalactic surveys.

In contrast to the work described in C07, I can no longer assume that the strongest emission line in the spectrum shortward of the continuum emission peak (determined from the position of the peak of the polynomial fit) is the [OI] line at $63.18 \mu\text{m}$, as I now have strong MIR lines present in the spectra. I can, however, still assume that the strongest line longward of the continuum emission peak is the [CII] line at $157.74 \mu\text{m}$. This is true as long as the reasonable assumption that $T_{\text{dust}} \gtrsim 20 \text{ K}$ holds, as [CII] is then typically the only strong line longward of the SED peak. Thus, if no single redshift is able to map the line template onto the observed line array, but the strongest line in the spectrum lies longward of the SED peak, and has a line to continuum ratio > 3 (found empirically to be the lowest value to reliably use to identify the [CII] emission line at $157.74 \mu\text{m}$ in this circumstance), I assume it to be the [CII] line and, from this, calculate a redshift.

An evaluated redshift is recorded along with the position of the source on the sky. The redshift is referred to as the primary redshift and is considered to be that of the brightest, or primary, source in the given spatial bin. A slightly modified redshift extraction algorithm is then run a second-time through the spectrum, to determine whether there is a second potential source of lower flux present: the secondary source. When attempting to extract a redshift for the secondary source in any spatial bin I first zero the lines in *OLA* which I have already associated with the primary source. I then add to *OLA* the 3 strongest lines in the spectrum that have not yet been used in redshift fitting to the spectrum, with flux $S_\lambda > 3.5\sigma^8$. This line selection process is used as a) I find empirically that 6 is the

⁸E.g. defining a line as any spectral channel which has $S_\lambda > 2\sigma$, if a spectrum contains 20 spectral channels with $S_\lambda > 2\sigma$, I populate *OLA* with the brightest 6 of these lines, leaving 14 unused lines in the spectrum. In order to determine a secondary redshift I zero the lines in the

optimum number of emission lines required to accurately fit a primary redshift (i.e. the maximum amount of lines the algorithm is able to use before encountering significant degeneracies) b) By definition the secondary source is fainter than the primary, thus I expect noise to be more of a significant hindrance in redshift fitting - therefore the method needs more stringent requirements on the strength of the emission lines used c) 3 is found to be the optimum number of lines to add to the previously selected lines which are not found to be associated with the primary source - if all 6 lines of the initially selected lines are found to be associated with the primary source then 3 emission lines is the minimum number that can be used to reliably fit a redshift, and any more than this can results in significant degeneracies in redshift fitting if a large number of the initially selected lines remain unassociated with the primary source. The algorithm now runs in a manner very similar to before, however (1) by definition I expect the continuum-subtracted emission lines from the secondary source to be of lower flux than those of the primary, and so the requirement on the ratio of the strongest to the weakest emission line in the observed array is dropped to 1.3, and (2) also by definition I am looking at sources of fainter continuum flux, and thus are more susceptible to picking up spurious emission lines: I therefore no longer weight more heavily redshifts which give matches for characteristic MIR/FIR emission line pairs, and no longer allow redshifts to be determined from the single [CII] emission line. Both these changes in the algorithm for secondary as opposed to primary redshift-determination are implemented because empirically they are found to give the most reliable results.

The PCC method works by moving through each spectrum in the cube and cross-

OLA which I have already associated with the primary source. If, for example, 4 lines in the *OLA* contributed to the highest value of C_k then these are zeroed, leaving 2 lines remaining in *OLA* which can be used to determine a secondary redshift. Of the 14 remaining unused lines above 2σ in the spectrum, 10 of these for example may have fluxes $S_\lambda > 3.5\sigma$, the 3 brightest of which I add to *OLA*. The *OLA* used to attempt to determine a secondary redshift therefore contains a total of 5 lines.

correlating MIR/FIR line templates at a discrete rather than continuous set of redshifts, and therefore attempts to fit far fewer redshifts to the spectrum. This means I am less likely to encounter a pixel with a high noise level which could be miss-identified as an emission line. I am therefore able to use weaker emission lines for redshift-determination, which enables the algorithm to probe more deeply into the noise. This is particularly powerful when looking at secondary sources which typically will have weaker line fluxes than primary sources

FIR Emission Lines Only :

As a first test of my automated redshift-determination I compare how efficiently my PCC method works in comparison to that described in C07. C07 made use of spectra containing FIR emission lines only, therefore a direct comparison of this original method, and my PCC method described in section 5.2.3 can only be made when using exactly the same spectra. To do this I use a variant of my PCC method which uses FIR emission lines only. The lines are listed in table 5.2. In addition, only the [OIII]/[NIII] and [OIII]/[NII] pairs at 51.82/57.32 and 88.36/121.90 μm respectively are used to additionally weight C_k , as these are the only characteristic pairs which lie in the FIR waveband as defined by C07.

Emission Line	OIII	NIII	OI	OIII	NII	OI	CII
Wavelength (μm)	51.82	57.32	63.18	88.36	121.90	145.53	157.74

Table 5.2: Lines used in source redshift-determination through template fitting for the FIR emission line only method.

MIR and FIR Emission Lines :

The general version of my method by default uses both MIR and FIR lines in my template array, which are listed in table 5.3. The version of the method also allows us to make use of all of the characteristic emission line pairs.

Emission Line	NeII	SIII	SIII	SiII	OIII	NIII	OI
Wavelength (μm)	12.81	18.71	33.42	34.82	51.82	57.32	63.18
	OIII	NII	OI	CII			
	88.36	121.90	145.53	157.74			

Table 5.3: Lines used in source redshift-determination through template fitting for the method using both FIR and MIR emission lines.

5.3 Results

All results given in this section were determined by taking the averaged values for each of 100 FoVs ($\times 10$ differently seeded noise arrays = 1000 SAFARI FoVs) for both bright-end and burst mode evolution. When quoting results from this work I give the number of accurate redshifts retrieved as a percentage of the total number of sources within a given flux and redshift range in the datacube. However the number of inaccurate redshifts are given as a percentage of the total number of redshifts output by the algorithm under the same constraints⁹.

5.3.1 Results From Clements et al. (2007)

The work described in C07 made use of spectra containing FIR emission lines only, and results were only determined for the burst mode evolution model. They found that all sources with redshifts at $z \leq 2.5$ with $S_{120\mu\text{m}} \geq 1$ mJy could be retrieved. Redshifts higher than this could not be determined, as beyond $z = 2.5$ the [OI] and [CII] lines are redshifted out of the SAFARI waveband.

Sources with $S_{120\mu\text{m}} \sim 0.4$ mJy (i.e. as much as 1/10th of the continuum confusion limit at $120 \mu\text{m}$) were also retrieved, albeit with lower efficiency.

⁹E.g. a datacube has 100 sources within the specified redshift and flux range and the algorithm outputs 50 redshifts; 40 accurate and 10 inaccurate. The results statement would then be given in the following form; I retrieve 40% of sources in my flux and redshift range accurately, with 20% of redshifts output by the algorithm under the same constraints being inaccurate.

5.3.2 Analysis Using FIR Emission Lines Only

Primary Sources :

Using the FIR emission line only version of my PCC method, as outlined in section 5.2.3, I find that I recover accurate redshifts for 85(46)%¹⁰ of all primary sources with $S_{120\mu m} \geq 1$ mJy, with 5(10)% of all primary redshifts output by the algorithm under the same constraints being inaccurate. The aforementioned recovery values are given as a percentage of all sources, including those at $z > 2.5$, but by definition this method is unable to retrieve redshifts for sources at $z > 2.5$. Beyond $z = 2.5$ the redshift recovery rate drops to zero for both evolutionary models. For sources with $S_{120\mu m} \geq 1$ mJy lying at $z < 2.5$ the recovery of redshifts for primary sources is $\sim 85(64)\%$. Under the same constraints C07 retrieved accurate redshifts for 100% of the sources. However in that work redshifts were determined manually for each source whereas in this work they are determined automatically. Unlike C07 I am unable to assess each spectrum on a case by case basis. Therefore in attempting to minimize the number of inaccurate redshifts output by the algorithm I am forced to limit the maximum possible efficiency of the accurate redshift recovery of the algorithm.

By dropping my 120 μm flux cutoff to $S_{120\mu m} \geq 0.342$ mJy, I find that I recover accurate redshifts for 36(33)% of all primary sources with $S_{120\mu m} \geq 0.342$ mJy, with 12(13)% of all redshifts output by the algorithm under the same constraints being inaccurate. Taking into account only sources at $z < 2.5$ my accurate recovery percentage becomes 45(39)%. By dropping the cutoff flux from 1 mJy to 0.342 mJy I have increased the total number of accurate redshifts recovered by 22(15)%, as the majority of sources have $S_{120\mu m} < 1$ mJy.

¹⁰Bright-end(Burst mode)

Secondary Sources :

Using the FIR emission line only PCC method I retrieve accurate redshifts for $\sim 30(27)\%$ of all secondary sources when using a flux cutoff of $S_{120\mu m} > 0.342$ mJy with $\sim 6(4)\%$ of all secondary redshifts output by the algorithm under the same constraints being inaccurate.

5.3.3 Extending Analysis to MIR

By default, the full version of my PCC redshift-determination method uses both MIR and FIR emission lines, and it is this version which would be applied to real data. It is now possible to investigate sources at redshifts $z > 2.5$ which account for $5(26)\%$ of the population with $S_{120\mu m} > 0.342$ mJy. Accurate redshifts are retrieved for $\sim 75\%$ of primary sources with $S_{120\mu m} \geq 1$ mJy, for both bright-end and burst mode evolution, with respectively $6(8)\%$ of all primary redshifts output by the algorithm under the same constraints being inaccurate.

I see here that using both MIR and FIR emission lines is less efficient in recovering accurate redshifts than only using FIR emission lines (while employing a $S_{120\mu m} \geq 1$ mJy cutoff), if $z < 2.5$. This is because most sources with $S_{120\mu m} \geq 1$ mJy lie at redshifts $z < 2.5$ in both evolution models, and I am subject to the disadvantage of significantly more degeneracies in redshift fitting due to a higher number of emission lines. Dropping the cutoff to $S_{120\mu m} \geq 0.342$ mJy, $38(54)\%$ of all primary sources with $S_{120\mu m} \geq 0.342$ mJy are retrieved (see figure 5.6), with $14(9)\%$ of all redshifts output by the algorithm under the same constraints being inaccurate.

Secondary Sources :

Employing a $120 \mu m$ cutoff of 0.342 mJy, I find that I am able to determine

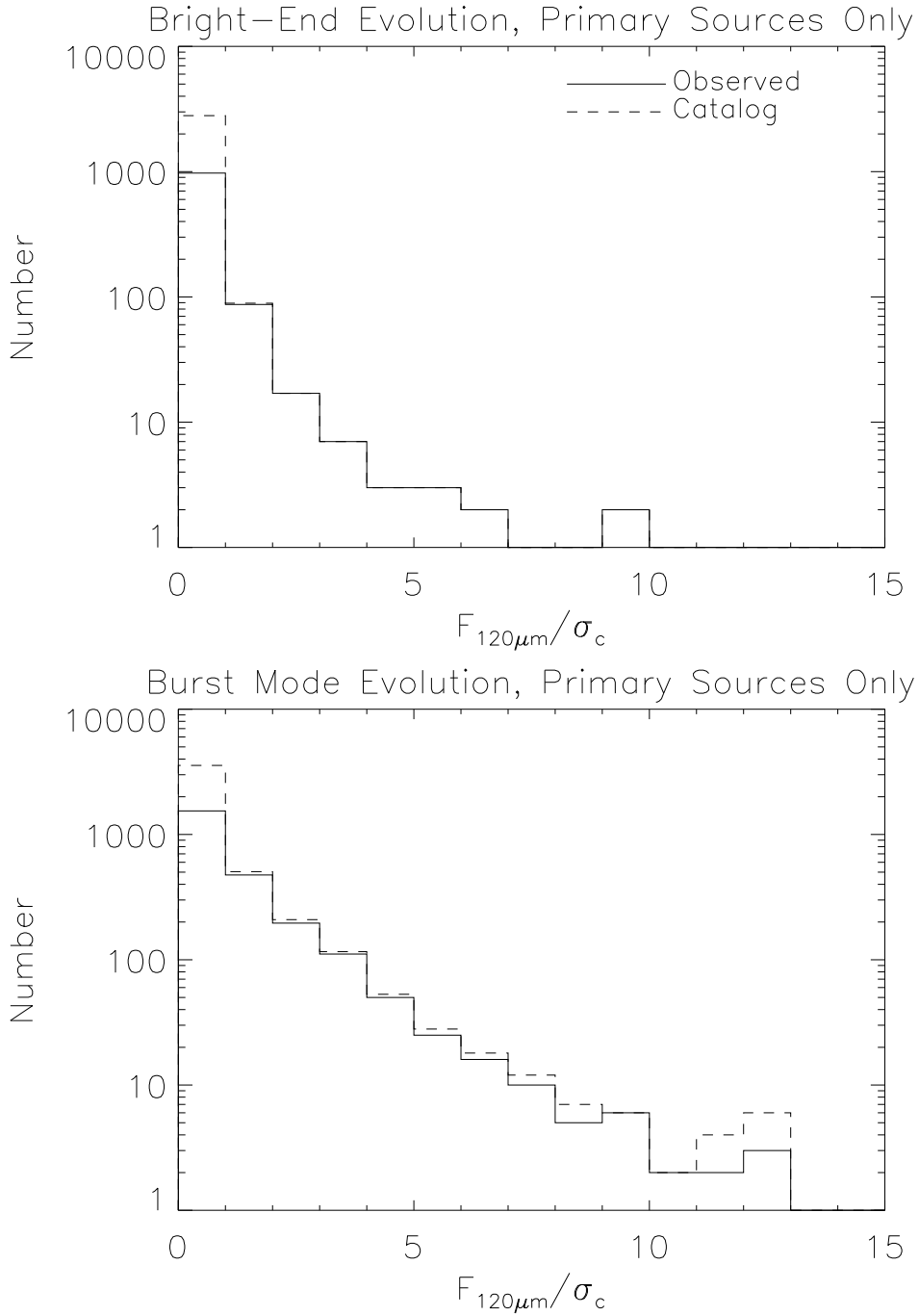


Figure 5.6: Plots of the $120\ \mu\text{m}$ continuum flux distribution (with flux measured as a fraction of the $120\ \mu\text{m}$ continuum confusion limit, $\sigma_c(\lambda = 120\mu\text{m}) = 4.3\ \text{mJy}$) for both the total input primary sources (dashed) and primary sources with accurately determined redshifts (solid). Shown in the top and bottom panels are the results for the bright-end and burst mode evolution models respectively. Results are for 100 SAFARI FoVs.

accurate redshifts for $\sim 38(29)\%$ of secondary sources with $S_{120\mu m} \geq 0.342$ mJy (see figure 5.7), with 11(18)% of all redshifts output by the algorithm under the same constraints being inaccurate.

5.4 Discussion

A summary of the most important results of this chapter can be seen in table 5.4. I find that using the PCC method as described in this work, I can recover redshifts for sources as much as 10 times below the traditional continuum confusion limit. I also find I am able to successfully retrieve redshifts from line confused spectra caused by multiple sources separated by smaller scales than the size of the SAFARI beam on the sky. However, using the burst mode and bright-end evolutionary models of Pearson (2005), Pearson et al. (2007) and Pearson & Khan (2009), I find very few spatial bins contain more than two sources with $S_{120\mu m} \geq 0.342$ mJy and therefore I do not test whether or not my method would be able to disentangle more sources than this.

	Primary Sources		Secondary Sources
Cutoff Flux	$S_{120\mu m} > 1$ mJy	$S_{120\mu m} > 0.342$ mJy	$S_{120\mu m} > 0.342$ mJy
FIR Only	85(46)%	36(33)%	30(27)%
MIR+FIR	75(75)%	38(54)%	38(29)%

Table 5.4: The percentage of sources with accurately recovered redshifts for primary and secondary sources, using FIR emission lines only as well as both MIR and FIR emission lines, and employing cutoff fluxes of $S_{120\mu m} > 0.342$ mJy and $S_{120\mu m} > 1$ mJy.

Shown in figure 5.8 is the cumulative recovery (fraction of sources accurately recovered with $S_{120\mu m}$ less than that defined by the x-axis) efficiency with increasing flux. All source populations (the primary and secondary sources of both bright-end and burst mode evolution) have a strongly increasing cumulative recovery fraction at low fluxes which then levels off at fluxes higher than the confusion limit. This

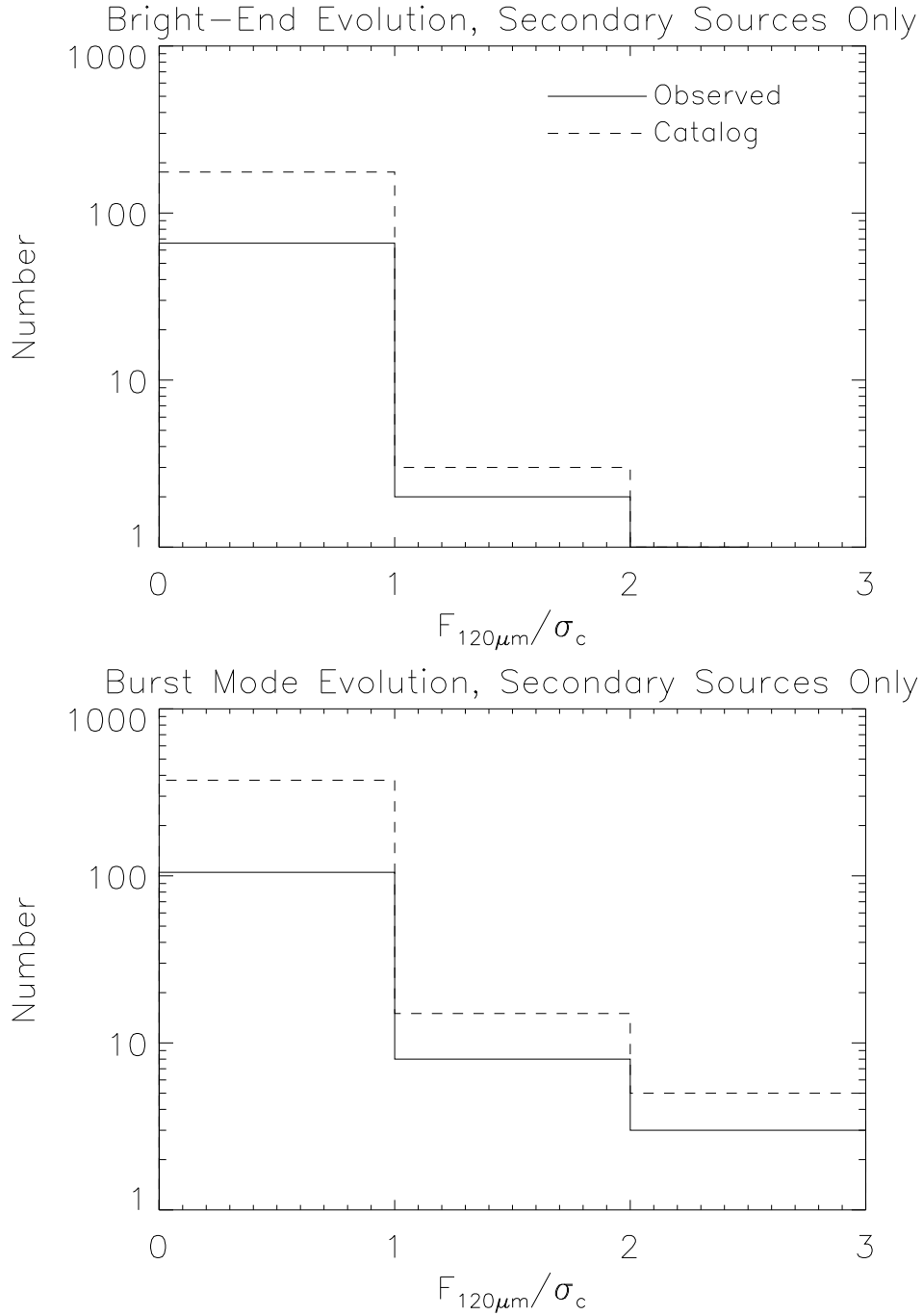


Figure 5.7: Plots of the $120 \mu m$ continuum flux distribution (with flux measured as a fraction of the $120 \mu m$ continuum confusion limit, $\sigma_c(\lambda = 120\mu m) = 4.3 \text{ mJy}$) for both the total input secondary sources (dashed) and secondary sources with accurately determined redshifts (solid). Shown in the top and bottom panels are the results for the bright-end and burst mode evolution models respectively. Results are for 100 SAFARI FoVs.

is because the bulk of their populations lie at very faint fluxes, therefore a small increase in efficiency of redshift-determination for faint sources greatly increases the total number of sources recovered over all fluxes.

The bright-end evolution model has a larger fraction of low flux sources, whereas the burst mode evolution model has a similar population of low flux sources, but also a larger number of brighter sources. The efficiency of my method falls off with decreasing flux (as illustrated in figure 5.6), therefore I retrieve the redshifts for the burst mode evolution model more efficiently than for the bright-end evolution model.

At higher fluxes the redshift-determination efficiency for both populations approaches 100%, however at these higher fluxes there are relatively fewer sources. Even at 10% of the confusion limit, I am still retrieving redshifts for $\sim 10\%$ of sources, and given that the number of sources at these fluxes is so large I am gaining information about a significantly larger number of galaxies than would be the case if I were confusion limited.

The percentage of retrieved redshifts which are in error is higher for secondary sources than for the primary sources. This is to be expected because by definition the secondary sources are fainter than the primary. I am thus more likely to confuse noise with emission lines. Another difficulty encountered when attempting to retrieve secondary redshifts is that I am unable to set a continuum flux limit to consider the source to be viable. Therefore I am most often attempting to estimate a redshift for a galaxy which is either fainter than the cutoff flux, or non-existent, significantly increasing the likelihood of retrieving an erroneous redshift. This problem is lessened somewhat by the introduction of more stringent criteria in other areas when attempting to retrieve secondary redshifts, but it remains the

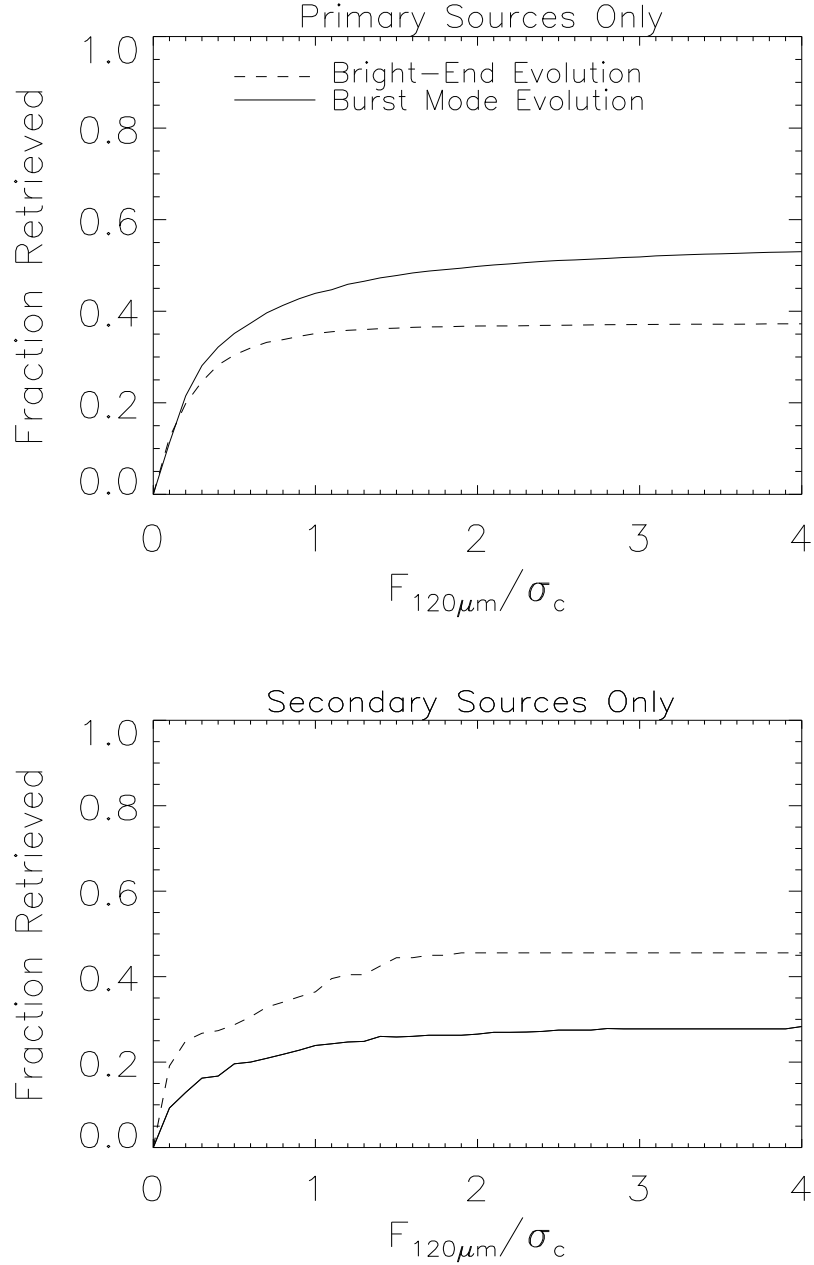


Figure 5.8: Plots of the cumulative fractional recovery of sources (fraction of sources accurately recovered with $S_{120\mu m}$ less than that defined by the x-axis) with increasing $120\mu m$ flux, measured as a fraction of the traditional $120\mu m$ continuum confusion limit, $\sigma_c(\lambda = 120\mu m) = 4.3$ mJy. The top panel shows my results for primary sources and the bottom panel shows my results for secondary sources. The results for burst mode evolution are plotted as a solid line, and for bright-end evolution as a dashed line.

cause of a large percentage of the inaccurate secondary redshift recoveries.

I find that by employing a cross correlation method for redshift determination, where I am only considering a very discrete set of redshift possibilities, I am able to reduce the $S_{120\mu m}$ cutoff value without drastically decreasing the efficiency of the method and thus am able to dig deeper into the instrumental noise. Employing the full MIR and FIR emission lines version of my method I find that I can retrieve accurate redshifts for a total of 38(52)% of all (i.e. both the primary and secondary sources) sources with $S_{120\mu m} \geq 0.342$ mJy for bright-end and burst mode evolution respectively. Their respective frequency of occurrence of inaccurate redshifts as a percentage of all redshifts output by the algorithm under the same constraints is 15(10)%.

A limitation of the PCC method is the possibility of sources with anomalous line strengths (such as Arp220) which can, for example, result in a misidentification of the [CII] line. The possibility of such occurrences has not been taken in to account here. Further improvement to my PCC method would aim to decrease the total number of erroneous redshifts output for reasons such as this.

Additional spectral features that can be used for finding redshift are those associated with the PAHs. These features are much broader than the emission lines I have been using, thus observations could be made at lower spectral resolution, with a corresponding increase in instrument sensitivity. In this work I have modeled angular resolution as being constant over the full SAFARI band. If I were to employ a more realistic model for angular resolution I may observe sources which are clustered in a single spatial bin in my current 8" binning, as being separable (visible in different spatial bins) at shorter wavelengths. This could significantly decrease the fraction of erroneous redshifts output for secondary sources.

As discussed earlier, the sources from the bright-end evolution model are mostly at low fluxes whereas the burst mode has in addition a smaller population of high flux sources. This accounts for the difference in my recovery rates for the two models. It is therefore important to further test the efficacy of my technique, and of this deep observing mode of SAFARI spectral imaging on a number of different evolutionary models.

Using a Kolmogorov-Smirnov test I am able to determine whether a set of recovered redshifts are from different parent populations. Thus by comparing redshift distributions recovered from datacubes of different sizes I can determine what area of sky is required for SAFARI to be able to reliably distinguish between different evolutionary models. I compare the maximum deviation between the cumulative distributions (Wall, 1996) of the redshifts output from my PCC method for skies populated with the burst mode evolution model and with the bright-end evolution model. I perform this comparison for increasing numbers of SPICA FoVs. Using my PCC redshift-determination method I find I am able to reliably distinguish (probability that the sources from the two models are drawn from the same distribution, $P = 0.01\%$) between the bright-end and burst mode evolution models with a sky survey area equal to 8 SAFARI FoVs, each of 10 hrs integration time.

5.5 Conclusions

I have found that my PCC redshift-determination method is capable of resolving sources (i.e. determining a unique redshift) more than an order of magnitude fainter than the traditional continuum confusion limit, however the efficacy of my method is higher for brighter sources. The total percentage of sources, accurately

recovered, with 120 μm flux greater than one tenth of the traditional continuum confusion limit ($S_{120\mu\text{m}} > \sigma_c/10$) is ~ 45 and 56% for the bright-end and burst mode galaxy evolution models, respectively.

In this work I have used the PCC method on models based around the SAFARI instrument for SPICA, however the same technique could be used on any sensitive imaging spectrometer. The bright-end and burst mode evolution models include sources up to redshifts of $z \sim 4$ and 5 respectively. At these redshifts I am still able to determine redshifts for sources using the PCC method. I have not yet tested to see at which redshift the PCC method begins to fail, this may be the subject of future work.

The evolutionary models I have investigated in this work have the bulk of their populations at fluxes fainter than the traditional continuum confusion limit for a 3.5 m telescope at 120 μm . The use of wide-area, spectroscopic surveys, as well as redshift estimation techniques should, through enabling us to extract extra information from the observed regions of sky, allow one to break through the confusion limit. This presents us with a better statistical sample with which to compare observed source counts and redshift distributions with those presented in different evolutionary models, therefore increasing the potential to reliably distinguish different evolutionary models and observations with much smaller area surveys, and therefore within shorter observing times.

Future work should include the following: 1) Use of the PAH features to identify sources and determine their redshifts. This will allow us to decrease the spectral resolution, thus increasing instrument sensitivity. 2) Investigation of the viability of taking into account sources with atypical line strengths. 3) More realistic angular resolution modeling where spatial resolution varies across the waveband. 4)

Investigation of the efficiency of the method when implemented on a wider range of evolutionary models. 5) A more quantitative analysis of where the ability to retrieve redshifts from single and combined spectra begins to break is discussed in chapter 6. 6) It should also be noted that since the work described in this paper was conducted the technical specifications of SAFARI have changed somewhat (e.g. waveband, sensitivity), therefore the results should be re-checked with more up to date modeling of the SAFARI instrument.

Chapter 6

Spectral Line Confusion in SAFARI Surveys

6.1 Introduction

In this chapter I concentrate in more detail on the impact of spectral confusion - the effective scrambling of spectra from multiple sources. For this work I will use the current specifications of SPICA/SAFARI (see appendix A), with a 3.2 m dish diameter, waveband coverage of 35 - 210 μm and a 5σ 10 hour sensitivity of 2 mJy. Simulations as described in the previous chapter have shown that, depending on the evolutionary model, as many as 8% of observed spectra with 120 μm flux, $S_{120\mu\text{m}} > 0.4$ mJy (equivalent to the up to date, predicted 1σ noise of SAFARI after 10 hours of integration, assuming a resolving power of $R = 1000$), are confused.

In order to maximize the amount of information a deep, wide-area spectral survey

can extract from each observation, it is necessary to overcome both spatial and spectral confusion, as much as possible. However, the ability to resolve spectral confusion is much more dependent on a number of various properties of the component galaxies than spatial confusion. Therefore in order to fully constrain our ability to retrieve the redshifts of spectrally confused galaxies, it is necessary to investigate the effectiveness of the method described in chapter 5 (hereafter simply referred to as ‘the method’) as a function of the various combined properties of the confused spectra. The key properties’ effects to investigate are:

- The relative flux contributions of the component sources: There are two effects to consider when assessing the sensitivity of the method’s effectiveness to the flux of the observed spectrum: 1) The unique flux of each of the component sources, i.e. how distinguishable the emission lines are from instrumental noise; 2) The relative flux of the component sources, i.e. are the emission lines from one source still detectable over the continuum emission of the other source.
- The sensitivity of the method to spectral type (i.e. the strength and number of emission lines present in a spectrum) - The method should be extremely reliant on the number of emission lines observable in SAFARI’s waveband, as well as the intrinsic brightness of these lines.
- Whether there are any emission line wavelength degeneracies for particular spectral type/redshift combinations, as well as if there are any redshift intervals for particular spectral combinations where the method breaks down.
- Beyond what redshift does the method begin to break down?

In this chapter I will present the results of a set of simulations investigating the

reliance of the effectiveness of the method on these properties. I generate a set of confused spectra made up of the sum of two galaxy spectra, covering combinations across the dimensions of redshift, luminosity and spectral type (there are 5 basic classes of galaxy used in this work to make the spectral templates; the justification for this, as well as a discussion of the nature of the galaxy templates, can be found in chapter 5). I then run the redshift extraction algorithm on all of these generated spectra, therefore determining the method's effectiveness over each of these parameter spaces.

6.2 The Model Spectra

Throughout this work I will concentrate on a subset of the spectra used in chapter 5. These have been chosen to be representative of the 5 main types of galaxy as discussed previously: Normal, Starburst, LIRG, ULIRG and Seyfert. The emission line templates added to the model continuum emission have been updated to match up with more recently published work using higher sensitivity observations (where available) from those used previously.

The selection criteria for FIR and MIR emission lines was simply that they are detected in the referenced (below) spectroscopic observations of the prototypical galaxies.

The Normal galaxy template's emission lines are based on the prototypical galaxy, NGC 7331. MIR emission line luminosities are taken from Smith et al. (2004) and FIR emission line luminosities are taken from Brauher et al. (2008). The prototypical galaxies from which the MIR emission line luminosities for LIRG and ULIRG templates are taken are NGC 253 (Sturm et al., 2000) and Arp 220 (Sturm

et al., 1996), respectively. The MIR emission line luminosities for the Starburst and Seyfert templates are taken from the work presented in Spinoglio et al. (2011), in which the averaged correlation between the emission lines in the MIR/FIR and infrared luminosity for active and starburst galaxies are calculated from a number of spectroscopic surveys. The FIR emission line luminosities (calculated as a fraction of the total FIR luminosity, $L_{8-1000\mu m}$, of each galaxy) for all galaxy templates other than Normal are also taken from Spinoglio et al. (2011). The continuum emission models remain unchanged.

There are some differences in the emission line strengths of the models used in this chapter compared to those used previously. In the cases of the MIR and FIR emission lines for Starburst and Seyfert type spectra, and the FIR emission lines for LIRG and ULIRG type spectra, in this chapter the line luminosities have been taken from the averaged results of a number of spectroscopic surveys (Spinoglio et al., 2011), whereas in the previous chapter they were taken from the results of spectroscopic observations of specific prototypical galaxies. These updated values were chosen for inclusion in the models simply because they provided a more ‘generic’ representation of the average emission line properties of the various spectral types. For the Normal model, the FIR emission line strengths have changed a little, due to the values having been taken from more recent results, however the differences are minimal (the maximum difference in line luminosity being approximately $\times 1.6$ for [OI]@63.18 μm). All other emission line fluxes remain the same as were used in the previous chapter.

The emission lines and their luminosities as a percentage of the total IR luminosity, $L_{1-1000\mu m}$, are listed in table 6.1. When adding the emission lines to the template SED, a rotational velocity of 500 km s⁻¹ is assumed in determining the width of the lines.

	Line ID $\lambda(\mu m)$	Br α 4.05	$H_2S(5)$ 6.91	$H_2S(2)$ 12.28	[NeII] 12.81	[NeV] 14.32	[CIII] 14.38	[NeIII] 15.55	$H_2S(1)$ 17.03	[PIII] 17.89	[FeII] 17.95
Galaxy Type L_{line}/L_{IR} ($10^{-2}\%$)	Normal	0.03	0.14	0.01	0.07
	Starburst	0.32	0.02	0.07
	LIRG	0.07	3.11	...	0.03	0.22	0.07	0.03	0.03
	ULIRG	0.34	0.39	...	0.85	0.38
	Seyfert	3.96	2.61	...	4.29	1.21

Table 6.1: Emission lines included in the model spectra for the template galaxies. Line luminosity is given as a percentage of the total IR luminosity, $L_{1-1000\mu m}$, of the galaxy.

	Line ID $\lambda(\mu m)$	[SIII] 18.71	[FeIII] 22.93	[NeV] 24.31	[OIV] 25.89	[FeII] 25.98	$H_2S(0)$ 28.22	[SIII] 33.48	[SiII] 34.82	[OIII] 51.81	[NIII] 57.32
Galaxy Type L_{line}/L_{IR} ($10^{-2}\%$)	Normal	0.06	0.01	0.02	0.04	0.22	0.51
	Starburst	0.68	0.01	2.88	2.47	4.48	3.14
	LIRG	0.73	0.13	...	0.09	0.27	...	1.69	2.64	4.87	3.41
	ULIRG	2.13	1.59	4.90	3.43
	Seyfert	5.07	...	1.57	21.84	3.37	2.55	2.91	2.04

Table 6.1: *cont.*

	Line ID $\lambda(\mu m)$	[OI] 63.18	[OIII] 88.36	[NII] 121.90	[OI] 145.53	[CII] 157.74
Galaxy Type L_{line}/L_{IR} ($10^{-2}\%$)	Normal	2.42	...	0.79	...	4.94
	Starburst	11.21	4.48	1.79	0.67	11.21
	LIRG	12.17	4.87	1.95	0.73	12.17
	ULIRG	12.24	4.90	1.96	0.73	12.24
	Seyfert	7.28	2.91	1.16	0.44	7.28

Table 6.1: *cont.*

The rest frame template spectra for all of the spectral types used in this work are shown in figure 6.1. Also shown is a plot of their 40 μm flux as a function of redshift, which is calculated employing a concordance cosmological model with $\Omega_{total} = 1$, $\Omega_m = 0.3$, $\Omega_\Lambda = 0.7$ and $H_0 = 75 \text{ kms}^{-1}\text{Mpc}^{-1}$.

6.3 Simulations

Each spectrum run through the algorithm is made up of the sum of two component spectra. A confused spectrum was generated for all possible combinations of spectral type, redshift and luminosity. Redshifts vary in the range $z = 0.2, 0.4 \dots 0.6$. Luminosities vary in the range $\log(L_{IR}/L_\odot) = 10, 10.5 \dots 12$. Spectra were binned to the resolving power of SAFARI at 120 μm of $R = 1000$, and unlike in previous work, the wavelength binning now varies as a function of wavelength.

The instrumental noise added to observed spectra has been modified to agree with the most recent technical specifications of SAFARI (see appendix A). Thus a randomly seeded noise array at a mean flux level of 0.4 mJy (equivalent to the 1σ noise of SAFARI after 10 hours of integration, assuming a resolving power of $R = 1000$) was added to each confused spectrum, before it was then run through the algorithm. A redshift estimate is taken to be accurate if $\frac{z_{input} - z_{output}}{z_{input}} < 0.1$.

6.3.1 Modifications to the Algorithm

The algorithm used in this chapter works in largely the same way it did as described in the previous chapter. However, due to some of the changes made to the template spectra, and the now varying wavelength binning along each spectrum, some minor

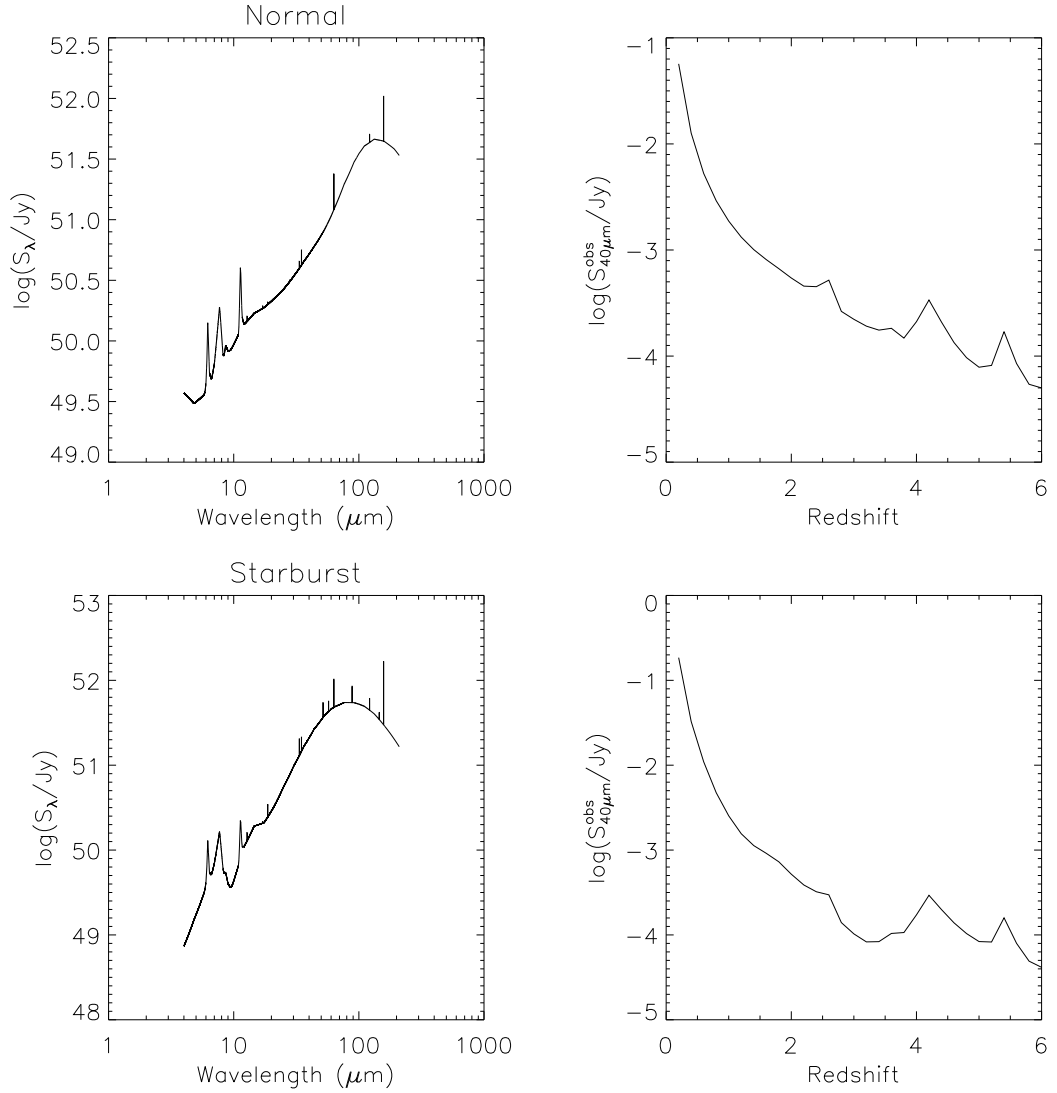
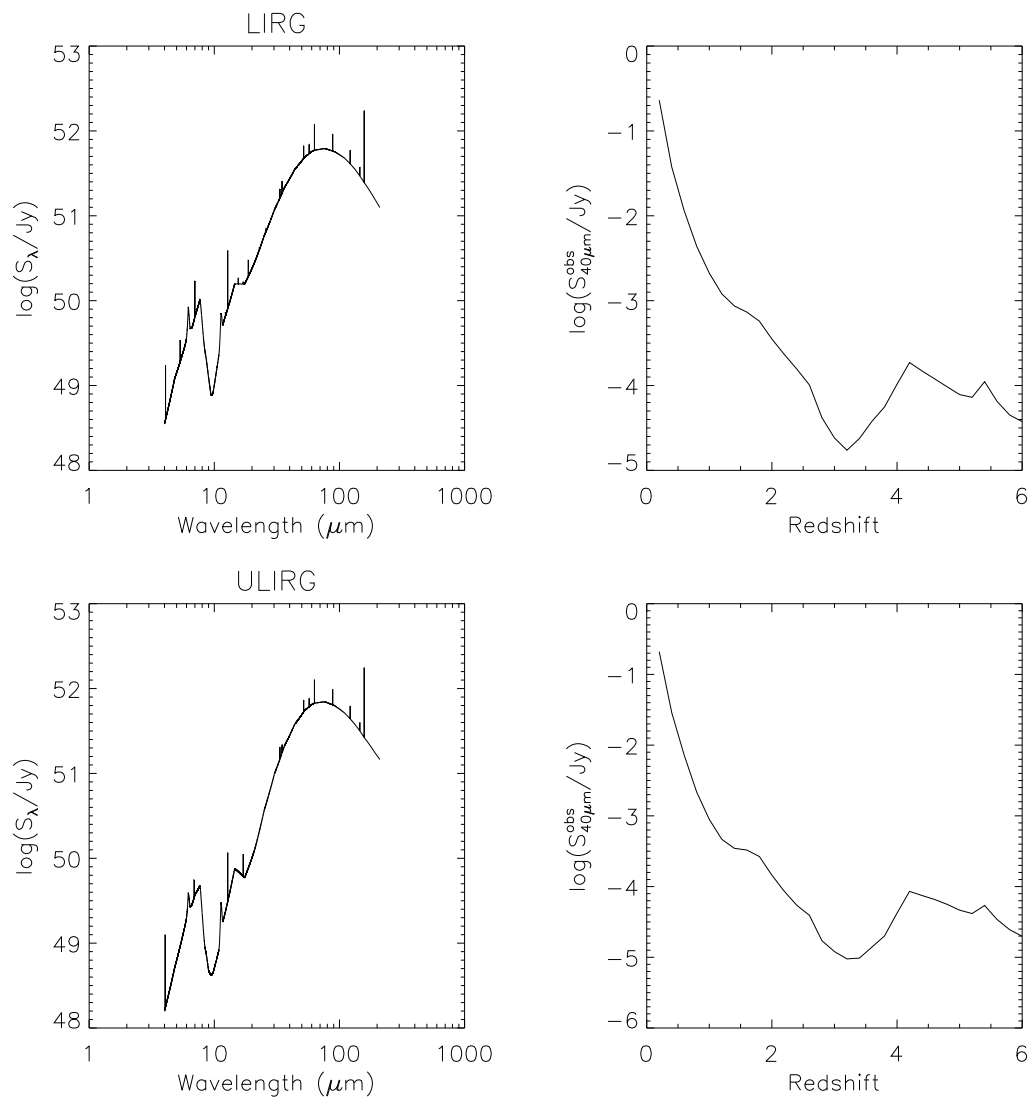
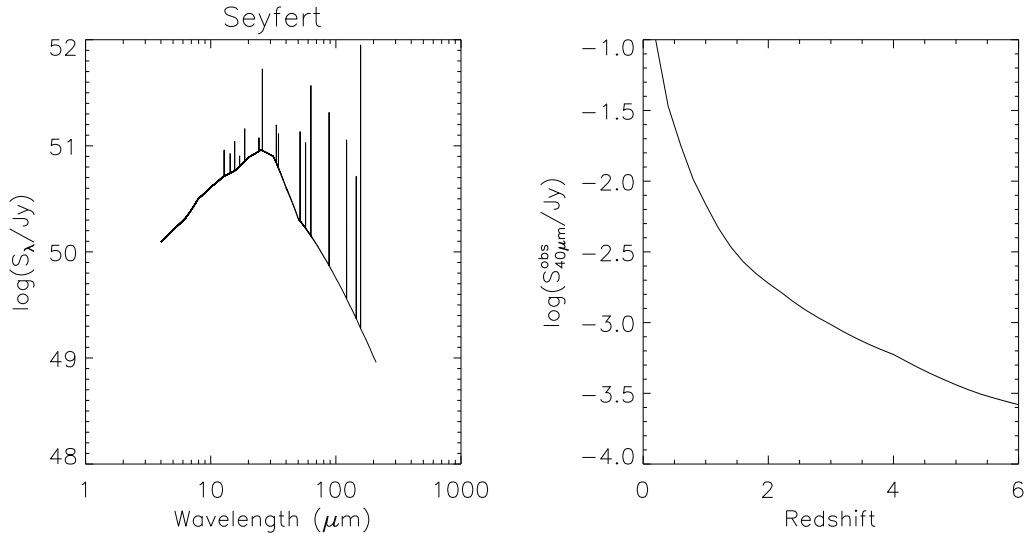


Figure 6.1: The left panels show the rest frame template spectra used in this work and the right panels show their observed $40\ \mu\text{m}$ flux as a function of redshift. All templates are normalized so that in their rest frame, i.e. at $z = 0$, they have an infrared luminosity, $L_{\text{IR}} = 10^{12} L_\odot$. The broad features present in the shorter wavelength regime of the spectra are the PAH features at 3.3 , 6.2 , 7.7 , 8.6 , 11.3 , and $12.7\ \mu\text{m}$ as well as the silicate absorption feature at $10\ \mu\text{m}$. These are also the origin of the dramatic dips and bumps in the plots of flux versus redshift.

Figure 6.1: *cont.*

Figure 6.1: *cont.*

modifications have been made to the code:

1) - One of the main changes to the code is that the continuum fitting method is no longer performed using polynomials. This is because the algorithm now has to fit confused spectra showing unusual continuum shapes, e.g. continua with two strong peaks in emission where both the spectra are of comparable flux. These continuum emission shapes are not fit very well using polynomials, therefore they are fit using a new method. An example confused spectrum prior to any continuum fitting is shown in the top panel of figure 6.2, and the new continuum fitting method is outlined below:

- Stepping through the spectrum, the standard deviation is measured in bins 4 times the size of the expected width of an emission line at that wavelength.
- If the standard deviation in a bin is found to be $1.5\times$ than the average across the whole spectrum, then that bin is considered to contain a possible emission line.

- If a bin is considered to contain a possible emission line then the spectrum is linearly interpolated over that region. An example of a spectrum after all possible emission lines have been removed is shown in the middle panel of figure 6.2.
- The continuum fit is then subtracted from the spectrum. The resulting array should contain only possible emission lines and some of the remaining instrumental noise from the bins containing the possible emission lines. An example of this is shown in the bottom panel of figure 6.2.

2) - Due to the changes made to the strength of the emission lines in the spectral templates, the emission lines used by the algorithm to fit a redshift to the spectrum have changed. However, whereas some emission lines are fainter than in the previous chapter, an equal amount appear to be brighter. Therefore the results from the previous chapter should not be too, if at all, adversely effected. The new list of emission lines used is shown in table 6.2.

3) - In the previous chapter, the algorithm made use of commonly observed emission line pairs by weighting any redshift which had a match with a pair more heavily. However, as an effect of the changes in the template emission lines, the [NIII] line at $57.32 \mu\text{m}$ isn't as strong a feature as was previously used, in all the spectral types. Therefore the [OIII]/[NII] emission line pair is no longer used to additionally weight any redshift fits.

Emission Line	[NeII]	[NeIII]	[SIII]	[OIV]	[SIII]	[SiII]	[OIII]
Wavelength (μm)	12.81	15.55	18.71	25.89	33.48	34.81	51.81
	[NIII]	[OI]	[OIII]	[NII]	[OI]	[CII]	
	57.32	63.18	88.36	121.90	145.53	157.74	

Table 6.2: Template emission lines used in the redshift fitting procedure.

4) - Due to the change in value of the updated instrumental noise, the cutoff flux

(i.e. the minimum flux that the confused spectra must have for the algorithm to attempt to fit redshifts to it) is increased to 0.4 mJy.

5) - The cutoff flux is no longer checked against the spectrum's 120 μm continuum flux, instead it is checked against the averaged continuum emission across the whole spectrum. This is due to there being more unusual continuum emission shapes compared to those in the previous chapter. Thus the algorithm avoids, as much as is possible, unnecessarily rejecting spectra (i.e. rejecting spectra which have a faint 120 μm flux, but are otherwise bright enough for the algorithm to be effective on) for redshift fitting.

6.4 Results & Discussion

Two of the primary factors controlling the efficiency of the method are the line flux and redshift of the sources. Redshift controls which emission lines are visible in SAFARI's waveband, and the intrinsic line brightness controls how easy these lines are to detect. Important to also investigate is the spectral type of the galaxy, which will also have an effect on what emission lines are observable.

6.4.1 As a Function of Flux

Figure 6.3 shows how well I am able to accurately recover the redshifts for each component galaxy in a composite spectrum, as a function of their spectral type and flux.

The lowest recovery rates occur for Normal type galaxies. This is most likely due

to the fact that the Normal type spectral template has smallest number of strong emission lines. Normal type spectral templates are therefore the most adversely affected by instrumental noise, as the majority of its emission lines become indistinguishable from instrumental noise for a relatively small drop in flux. Therefore it is no surprise that the redshift recovery rate for Normal galaxies will drop-off at a higher flux than for other sources.

Conversely, the best recovery rates are seen in ULIRG, LIRG and Starburst type galaxies. All of these galaxies types have a large number of very bright emission lines, which are still observable even at very faint continuum emission.

For most sources I am able to accurately recover a redshift for at least one of the galaxies as long as that galaxy has $S_{40\mu m} > 0.1$ mJy. The absolute flux of each galaxy appears to be the most important factor regulating my ability to accurately estimate a redshift for a component galaxy. It seems that absolute flux of each component is even more important than their relative flux. An exception to this is for combinations of Normal and other type spectra. The differences in the shapes their continuum emission mean that the emission lines from the Normal type spectra are often difficult to detect against the strong continuum emission from the other spectrum. Additionally, the apparent ‘oblong’ shape of the plotted results is due to the total continuum emission from the combined spectra dropping below the cutoff flux of the algorithm once the contribution from the non-Normal spectrum decreases. Thus this observed result is an artificial construct of the way in which the redshift-determination algorithm works.

It is possible to accurately estimate redshifts for both of the component galaxies even when one of the galaxies has a $40\ \mu m$ flux 10 times that of the other (i.e. $0.1 < S(1)_{40\mu m}/S(2)_{40\mu m} < 10$), as long as they both have $S_{40\mu m} > 0.1$ mJy.

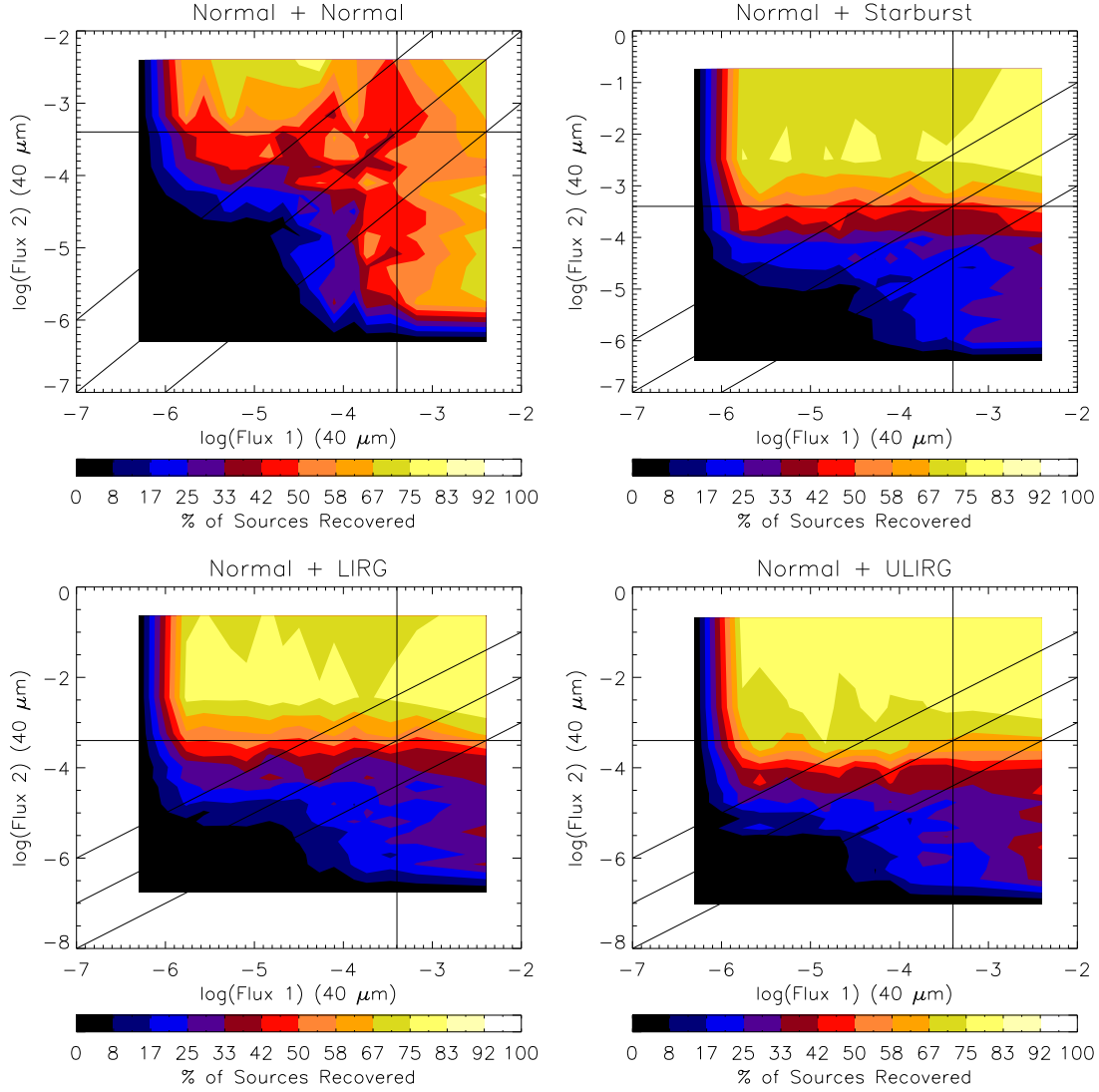


Figure 6.3: The average percentage of component sources with accurately estimated redshifts for spectra made up of two component sources, with redshifts in the range $z = 0.2, 0.4 \dots 6$ and IR luminosities in the range $\log(L_{\text{IR}}/L_{\odot}) = 10, 10.5 \dots 12$. Results are plotted as a function of the $40 \mu\text{m}$ flux of each of the component sources. In each plot the first spectral type named relates to Flux 1, and the second to Flux 2. The solid vertical and horizontal lines show $S_{40\mu\text{m}} = 0.4 \text{ mJy}$ for galaxy 1 and 2 respectively. The solid diagonal lines show $S_{40\mu\text{m}}(\text{Galaxy1})/S_{40\mu\text{m}}(\text{Galaxy2}) = 0.1, 1$ and 10 . Component sources are, from left to right, top to bottom: Normal and Normal; Normal and Starburst; Normal and LIRG; Normal and ULIRG.

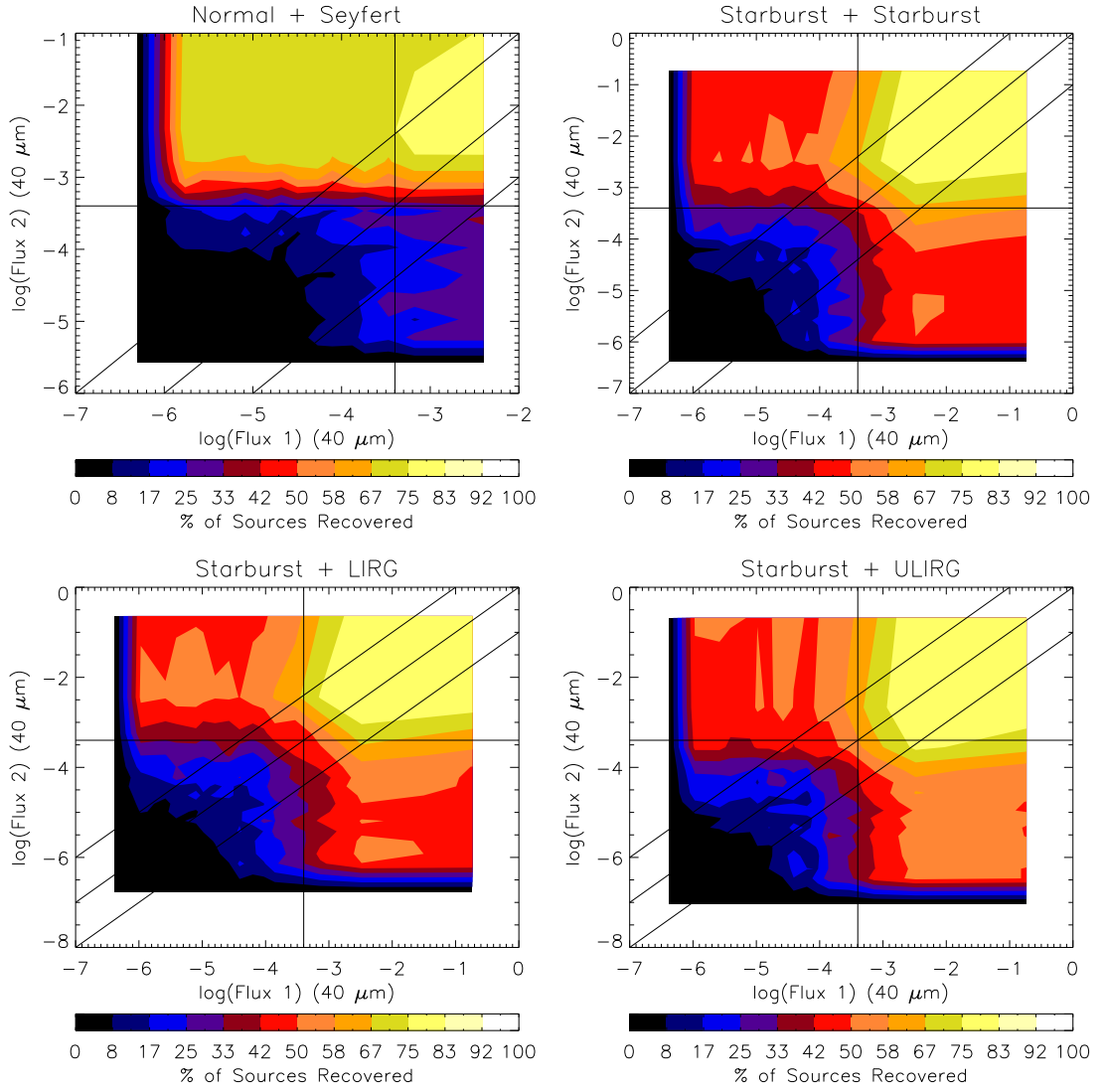


Figure 6.3: *cont.* Component sources are, from left to right, top to bottom: Normal and Seyfert; Starburst and Starburst; Starburst and LIRG; Starburst and ULIRG.

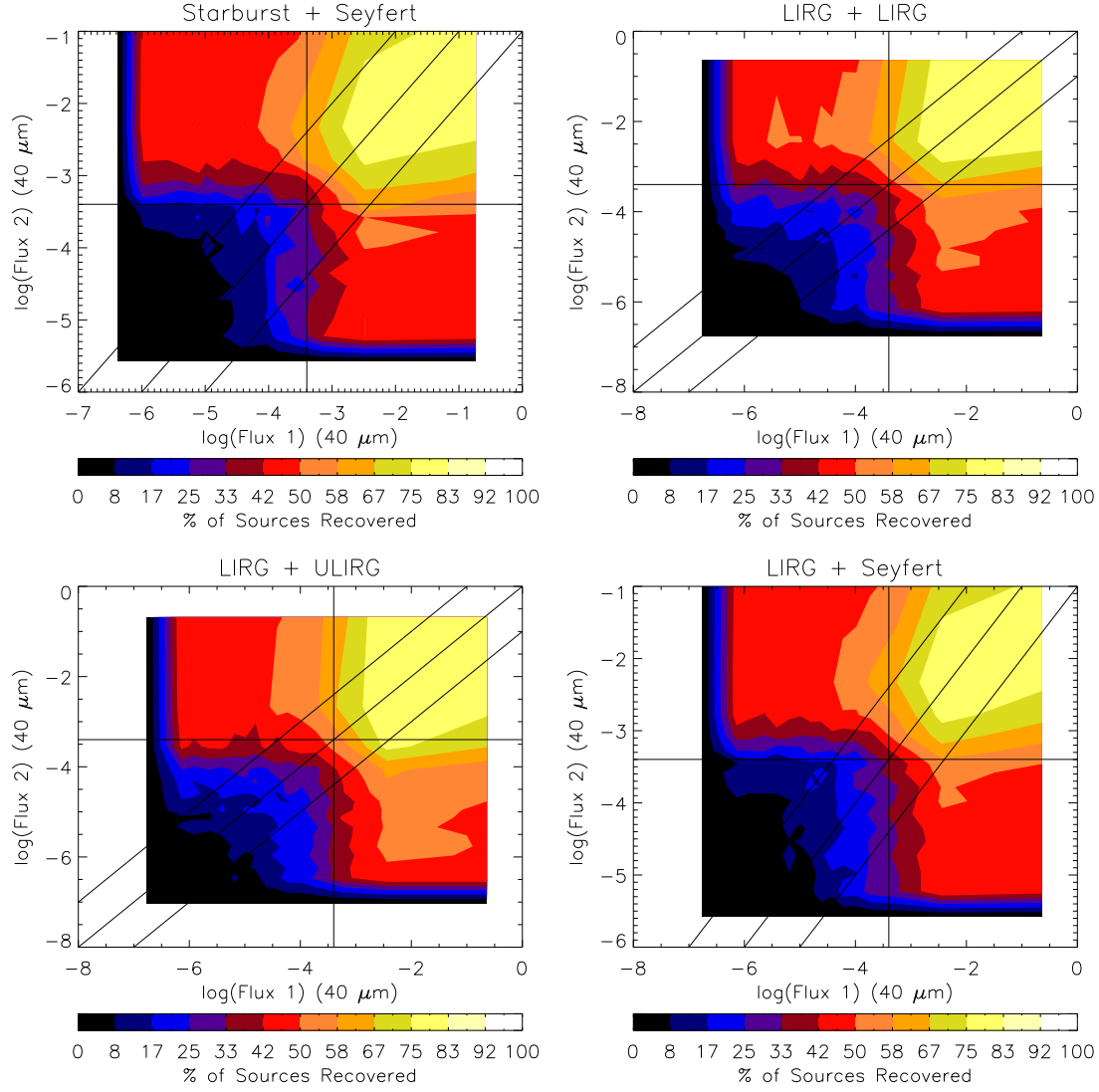


Figure 6.3: *cont.* Component sources are, from left to right, top to bottom: Starburst and Seyfert; LIRG and LIRG; LIRG and ULIRG; LIRG and Seyfert.

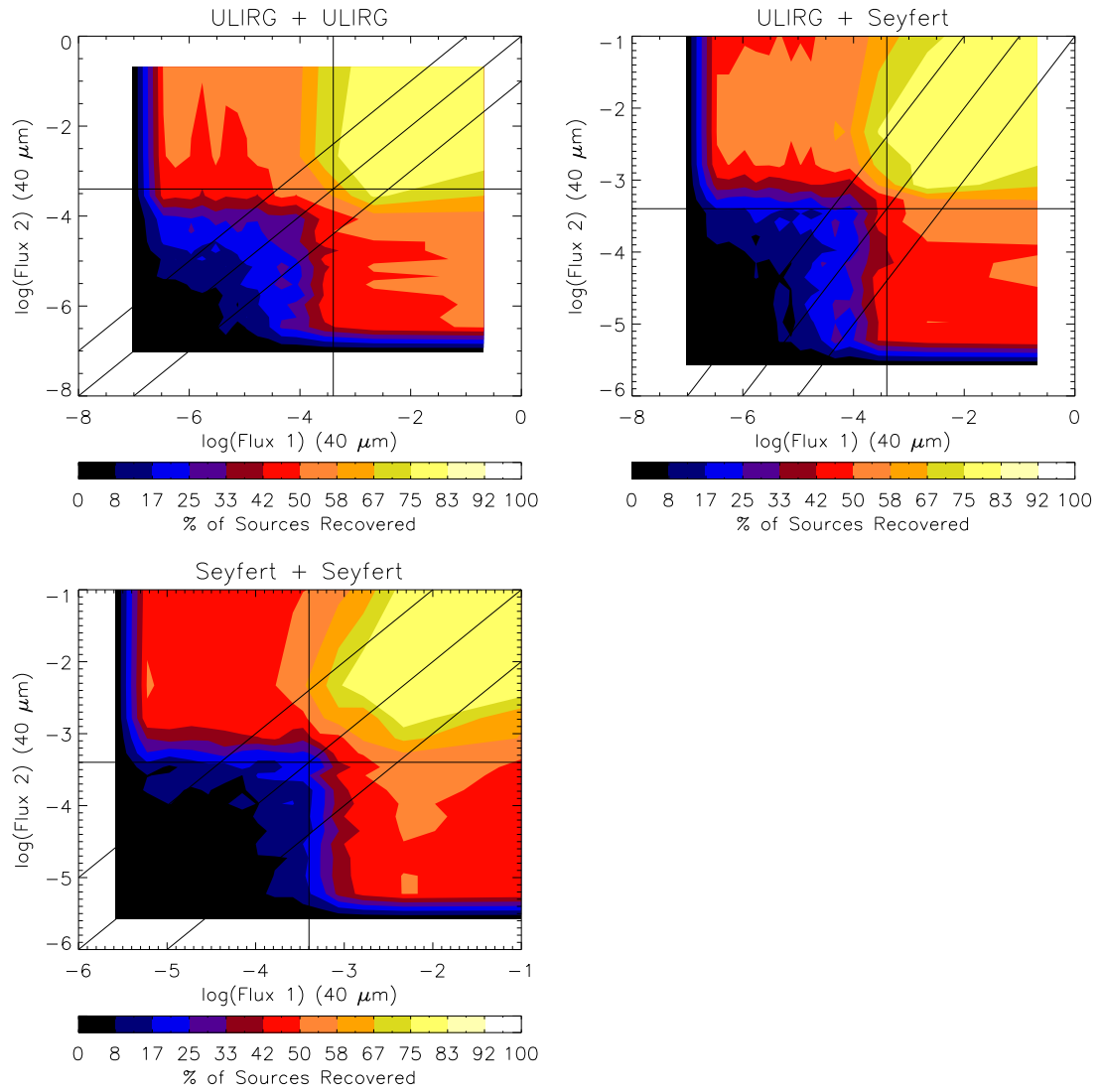


Figure 6.3: *cont.* Component sources are, from left to right, top to bottom: ULIRG and ULIRG; ULIRG and Seyfert; Seyfert and Seyfert.

An exception to this rule is Seyfert type galaxies, for which the redshift recovery does seem to be somewhat more controlled by the relative flux of the component sources. This can be seen when plotting the recovery of redshifts versus flux for Seyfert galaxies (figure 6.3); the contours seem to follow the bounding $S_{40\mu m}(\text{Galaxy 1})/S_{40\mu m}(\text{Galaxy 2})$ lines more closely than for other galaxy types. This is most likely due to the shape of the SEDs of Seyfert type galaxies, where the brightest emission lines lie on a continuum whose emission at wavelengths beyond its peak, drops off rapidly. Therefore these lines are more likely to be undetectable against brighter continuum emission from the other component spectrum.

6.4.2 As a Function of Redshift

Figure 6.4 shows how well I am able to accurately recover redshifts as a function of the spectral type and redshift of the two component galaxies. All of the component galaxies have IR luminosity, $L_{IR} = 10^{12}L_{\odot}$ (i.e. the maximum value used in the simulations), so as to minimize the effects of noise on the evaluation of recovery. A key result, observable at first glance, is that the highest recovery rates typically occur for galaxies with a distribution of bright emission lines over a wide range of wavelengths.

A key point of investigating the impact of redshift on the redshift recovery efficiency is isolating and separating out the effect of flux as much as possible. Clearly, the flux of each source will drop as a function of redshift. I have already investigated the effects of flux on the efficiency of redshift recovery in section 6.4.1, and determined an approximate critical flux, S_{crit} , where the redshift recovery efficiency begins to drop-off for each spectral type. By comparing S_{crit} with the plots shown in figure 6.1 I can then estimate the coincident critical redshift, z_{crit} , at which the

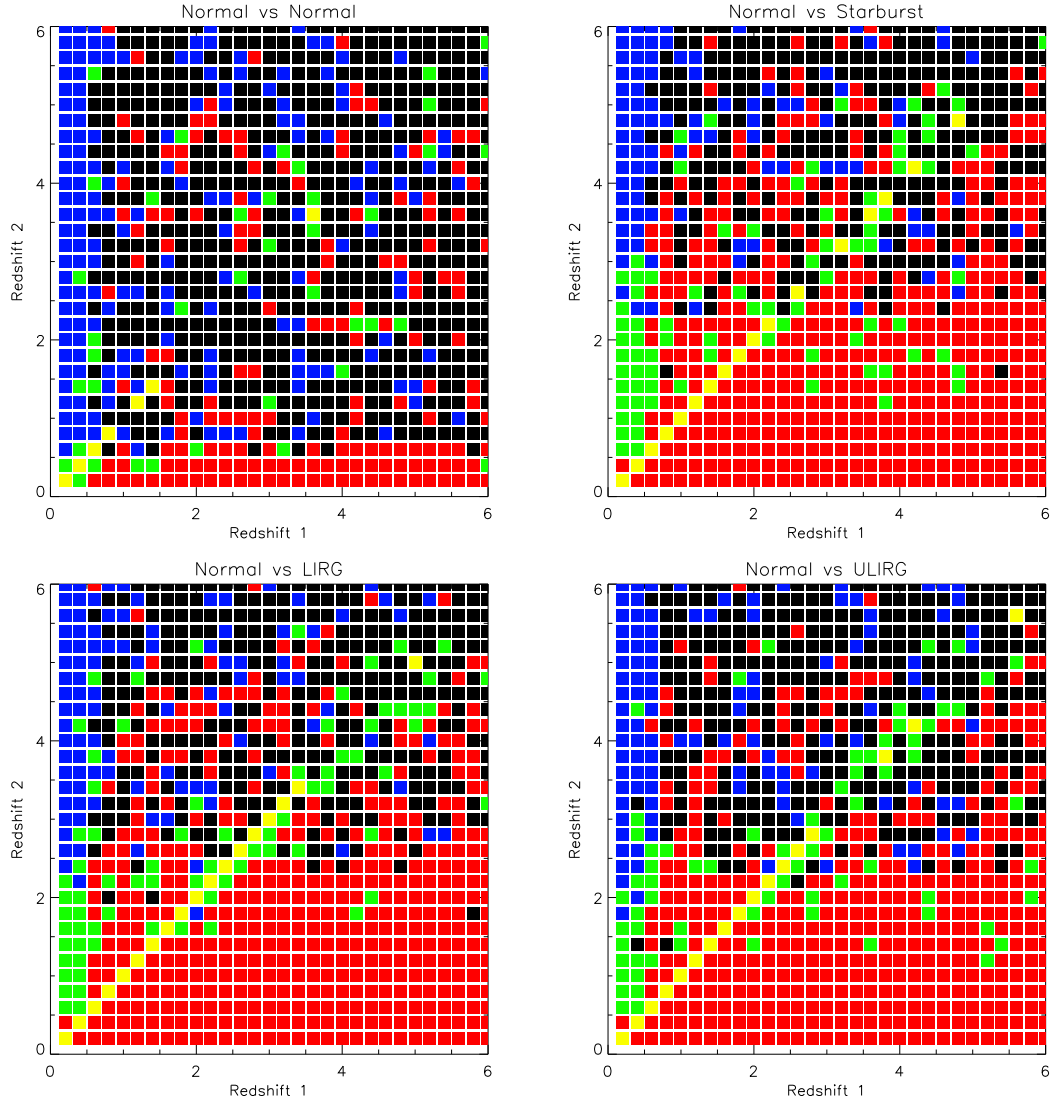


Figure 6.4: The distribution of sources with accurately estimated redshifts as a function of the redshift of each of the component galaxies. In each plot the first spectral type named relates to Redshift 1, and the second to Redshift 2. Blue and red squares show where an accurate redshift has been estimated for either component galaxy 1 or 2, respectively. Green squares show where accurate redshifts have been estimated for both of the component galaxies. Yellow squares show where an accurate redshift has been estimated when both of the galaxies are at the same redshift. Black squares show where no redshift has been accurately estimated for either source. All galaxies have IR luminosities, $L_{1-1000\mu m} = 10^{12}L_{\odot}$. Component sources are, from left to right, top to bottom: Normal and Normal; Normal and Starburst; Normal and LIRG; Normal and ULIRG.

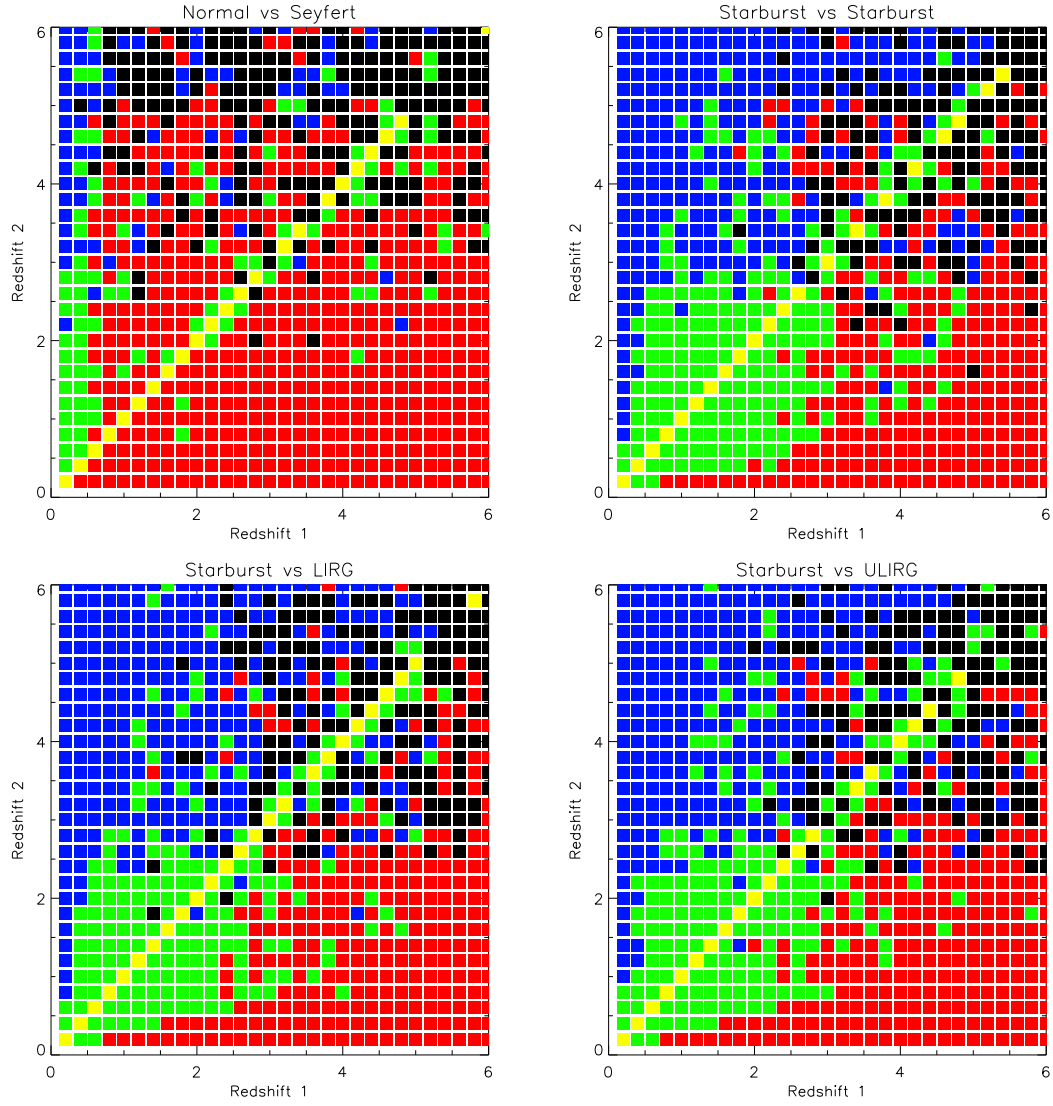


Figure 6.4: *cont.* Component sources are, from left to right, top to bottom: Normal and Seyfert; Starburst and Starburst; Starburst and LIRG; Starburst and ULIRG.

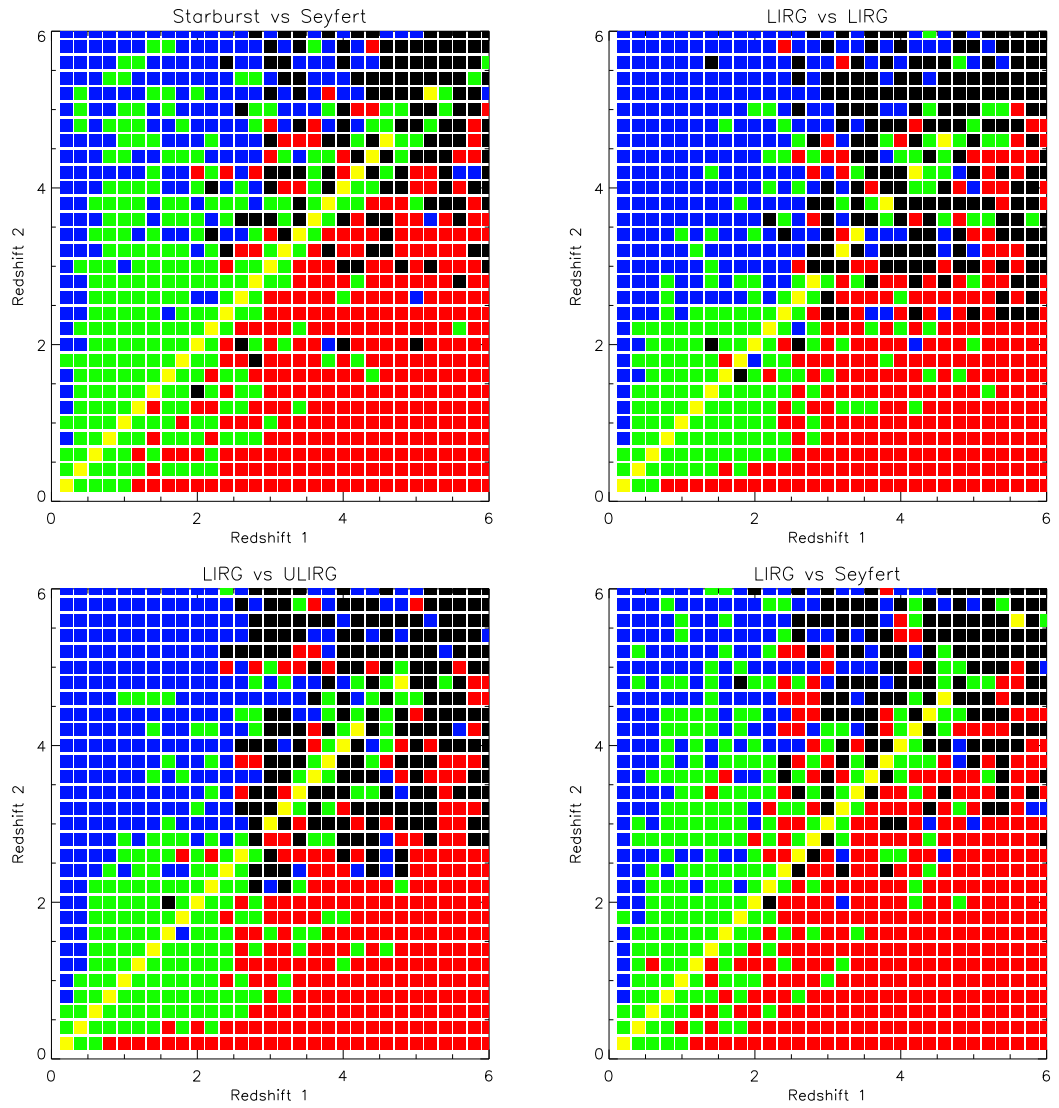


Figure 6.4: *cont.* Component sources are, from left to right, top to bottom: Starburst and Seyfert; LIRG and LIRG; LIRG and ULIRG; LIRG and Seyfert.

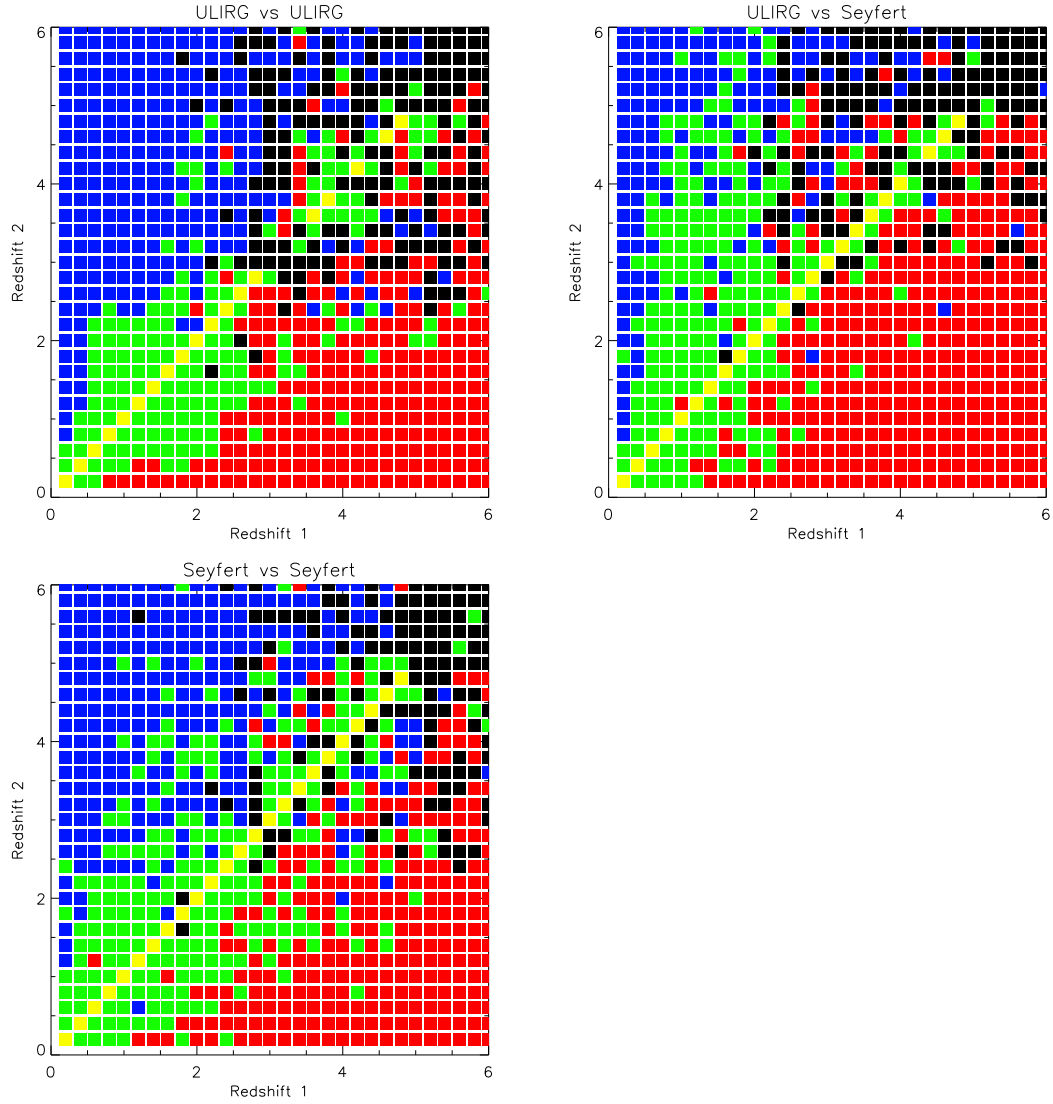


Figure 6.4: *cont.* Component sources are, from left to right, top to bottom: ULIRG and ULIRG; ULIRG and Seyfert; Seyfert and Seyfert.

template galaxy reaches this flux. Therefore, when investigating the redshift recovery efficiency purely in the redshift parameter space, of important note is whether the drop-off in recovery occurs at $z < z_{crit}$ or $z \gtrsim z_{crit}$. In the former case then the drop-off in recovery cannot be explained by flux, and therefore is likely an effect of the emission lines present in the waveband; in the latter case then the drop-off can be explained simply by the effects of noise.

It is worth noting that for all of the spectral types, the results appear to be constant irregardless of what the other component spectrums's spectral type is. In other words, the method is not reliant of the various combinations of spectral type, rather only the individual spectral type.

Normal Galaxies :

Normal galaxies show the weakest recovery as a function of redshift of all the spectral types. The drop-off in recovery rate of redshifts for Normal galaxies occurs at a redshift $z \sim 0.6$. This corresponds to a $40 \mu\text{m}$ flux, $S_{40\mu\text{m}} \sim 5.4 \text{ mJy}$, which is much higher than the observed cutoff flux for Normal galaxies, as seen in figure 6.3. This implies that it is the effect of redshift rather than flux that causes this drop-off - the most likely explanation being that all of the useful emission lines used for redshift fitting have been shifted out of the SAFARI waveband at greater redshifts than this. Examining table 6.1 to see what emission lines are observable in the SAFARI waveband beyond $z = 0.6$ reaffirms that this is most likely the case, as the majority of remaining emission lines are faint.

Starburst Galaxies :

The drop-off in redshift recovery efficiency for Starburst galaxies appears to begin at redshifts $z \sim 2.8$, which corresponds approximately to a $40 \mu\text{m}$ flux, $S_{40\mu\text{m}} \sim 0.14 \text{ mJy}$. This value is similar to the critical flux observed in figure 6.3,

which suggests that the key factor controlling the limit of the method's ability to accurately estimate redshifts for Starburst galaxies is the brightness of the galaxy, and the relative level of the instrumental noise.

LIRGs :

The drop-off in redshift recovery efficiency for LIRGs appears to begin at redshifts $z \sim 2.8$, which corresponds to $S_{40\mu m} \sim 0.04$ mJy. Comparing this to the critical flux observed in figure 6.3, again implies that the limiting factor controlling the recovery efficiency for this spectral template is the ratio of the brightness of the galaxy to the instrumental noise.

ULIRGs :

The drop-off in redshift recovery efficiency for ULIRGs appears to begin at redshifts $z \sim 2.8$, which corresponds approximately to $S_{40\mu m} \sim 0.02$ mJy. Comparing this to the critical flux observed in figure 6.3, again implies that the limiting factor controlling the recovery efficiency for this spectral template is the brightness of the galaxy/instrumental noise.

Seyfert Galaxies :

The drop-off in redshift recovery efficiency for Seyfert galaxies appears to occur roughly over the range $z \sim 3 - 4.4$, which corresponds to $S_{40\mu m} \sim 1 - 0.5$ mJy. The perceivable drop-off in recovery is far less steep than for other spectral types, with redshifts still being accurately recoverable at much higher redshifts. This is most likely due to the shape of the Seyfert SED, which has most of its luminosity at MIR wavelengths, and therefore the drop-off of observed $40 \mu m$ flux versus redshift at higher redshifts is much less steep than for other spectral types. Again, comparing these results with those observed in figure 6.3 implies that the main factor controlling the recovery efficiency for this spectral template is the brightness of

the galaxy relative to the instrumental noise. However, the distribution of sources from which we have accurate estimates for both component redshifts more closely follows the $z_1 = z_2$ line than for other galaxies. This is likely due to the effect discussed earlier, where the recovery of redshifts from Seyfert galaxies seem much more dependent on the relative brightness (i.e. $S_{40\mu m}(\text{Galaxy 1})/S_{40\mu m}(\text{Galaxy 2})$) of the component galaxies than the other spectral types are typically.

6.5 Conclusions

The dominating factors controlling the method's ability to accurately estimate redshifts for the component galaxies of spectrally controlled sources appears to be the brightness of the component galaxies and the number of observable emission lines present in each component spectrum. Investigation does not show any clear regions in the redshift parameter space where there appear to be degenerate redshift solutions for the observed positions of the emission lines. Providing individual galaxies are bright enough, the method only begins to fail once all of the emission lines bright enough to be detected against the other component spectrum's emission as well as the instrumental noise, have been redshifted out of SAFARI's observable waveband.

For galaxies in which there is a wide distribution of emission lines (i.e. those which have emission lines present in SAFARI's waveband over a wide range of redshifts), the efficiency of their recovery is dominantly dependant on their brightness relative to the instrumental noise. When plotting recovery as a function of flux there appears to be a critical flux - where the peak emission line fluxes drops to the same order as the 1σ value of the instrumental noise - beyond which the recovery

efficiency drops off steeply, with no redshifts accurately recovered beyond this.

Galaxies that do not have a wide spread in wavelength of bright emission lines show a much poorer recovery efficiency, with the dominant controlling factor being the source redshift. Unsurprisingly, the critical redshift (i.e. the source redshift beyond which the method starts to fail) occurs when the majority of the strongest emission lines (i.e. those most likely to be detectable by the method) are no longer visible in SAFARI's waveband.

Chapter 7

Conclusions

7.1 Selecting Galaxies at 1.1 mm

In chapter 2, I estimated redshifts for a statistically complete sample of seven sources selected at 1.1 mm. I estimated a mean photometric redshift of $z_{mean} \sim 2.57$ and a maximum of $z_{max} = 4.50$. In previous surveys carried out at 850 μm (Chapman et al., 2005; Pope et al., 2006; Dye et al., 2008; Clements et al., 2008) - with a collective sample of ~ 200 galaxies - only one galaxy is at a higher redshift than my two highest redshift sources. In addition to this, two of the selected at 1.1 mm sources are undetectable down to very faint optical magnitudes - implying that they might be at even higher redshifts. This agrees with Eales et al. (2003), who found that some SMGs have low 850 to 1200 μm flux ratios, and suggested that 1.1 mm observations may be more efficient at detecting high redshift SMGs than 850 μm surveys.

Re-investigating the evolution in space density of a sample of 38 850 μm selected

galaxies (Pope et al., 2006; Wall et al., 2008) I find some evidence for a redshift cutoff in the space density of sources at $z \sim 1$ assuming a ‘hot’ type SED, and marginal evidence when assuming a ‘cold’ type SED for a redshift cutoff at $z \sim 2$. These results are from a relatively small sample, however, and therefore may not be completely reliable. I also found evidence - in agreement with Wall et al. (2008) - for two separately evolving sub-populations, separated in luminosity.

All the samples investigated in this work are statistically complete - i.e. they do not require a radio identification, and are therefore not limited to redshifts $z < 3$. In this unbiased sample I find some evidence for a redshift cutoff between $z \sim 1-2$, suggesting that the deficit of high redshift SMGs is real. However, the sample sizes used in this work are relatively small - and therefore the results may not be robust. In order to more fully investigate whether or not there is a real redshift cutoff for SMGs, larger surveys need to be made in the future, with instruments such as *Herschel* and SCUBA2.

7.2 The Origin of the Decline in the Cosmic Star Formation Rate

In a sample of 102 galaxies detected by *Herschel* at $250 \mu\text{m}$, with either a spectroscopic or estimated photometric redshift, only $\sim 1/4$ of galaxies at $z \sim 1$ showed optical morphological evidence of undergoing a major merger. This implies that a drop in the number of major mergers since redshifts $z \sim 1$ is not responsible for the coinciding drop in the cosmic star formation rate.

There are a number of other processes, which do not have such a strong effect on a

galaxy's optical morphology, that could effect the star formation rates of galaxies. These include minor mergers, weak tidal interactions with small satellite galaxies, and the depletion of cold gas from star formation.

I used the da Cunha et al. (2008) model to estimate star formation rates (SFR) and specific star formation rates (sSFR), stellar and dust masses for the 74 isolated galaxies in this sample with either a spectroscopic redshift, or a estimated photometric redshift with $z < 2$ (as beyond this redshift my photometric estimates appear to be less accurate). Where any correlations are found, my results agree with the existing literature. I find evidence that galaxies at higher redshifts are undergoing more recent bursts of star formation, whereas local galaxies have already formed the majority of their stellar population. These results are in agreement with a 'downsizing' theory of galaxy formation (Cowie et al., 1996), where the most massive galaxies form at higher redshifts.

Of particular interest in my sample is that they are a clean set of isolated, non-merging systems. Therefore it possible to look for explanations for the steep decline in cosmic SFR since redshifts $z \sim 1$, in a sample in which merging is unlikely to have had an effect. Assuming that the gas mass of a galaxy correlates reasonably well with its dust mass, I find a - somewhat scattered - relationship with the SFR increasing with the gas mass of a galaxy. Therefore the drop in the cosmic SFR could be due to a coinciding drop in the average gas mass of a galaxy since $z \sim 1$.

7.3 Breaking Through the Confusion Limit

Sensitive imaging spectrometers could, in the future, provide a unique method by which we can break through the confusion limit of wide area continuum IR surveys -

allowing us to go much deeper in our observations. I find that I am able to estimate accurate redshifts for - and therefore uniquely resolve - spatially confused sources with $120\ \mu\text{m}$ flux as much as ten times below the traditional continuum confusion limit.

Additionally, I also find that I am able to uniquely identify spectrally confused sources down to very faint fluxes. However, the effectiveness of this method is very dependent on the spectral type of the galaxy, i.e. the number and distribution of strong emission lines across the spectrum.

In the evolution models used in this work, the majority of the galaxies lie at fluxes well below the traditional continuum confusion limit. Therefore the use of imaging spectrometers, and methods to automatically estimate redshifts for all sources, should allow us to glean information about a previously inaccessible population of IR galaxies.

7.4 Finally...

Currently operating instruments, such as the *Herschel* Space Observatory, are providing ever-increasing insights into the true nature of the Universe at IR wavelengths. Large-area surveys by *Herschel*, as well as the next generation of IR space telescopes, should help resolve a great number of the issues discussed in this thesis, such as the existence of a redshift cutoff in the space density of SMGs, and the main reason for the decline in the cosmic star formation rate since $z\sim 1$.

In the future, imaging spectrometers such as the SAFARI instrument on the proposed SPICA mission will provide an unprecedentedly sensitive view of the IR

Universe, and the spectral makeup of its extragalactic population. The ability to resolve emission lines in galaxies' spectra will enable us to diagnose the mechanisms by which the dust is heated - thus leading to understanding of the nature of the powering of the CIB. Additionally, the implementation of automated redshift estimation methods on deep, wide-area surveys will allow us to break through the continuum confusion limit by uniquely identifying sources via their redshifts. This in turn will allow us to extract new information about a population of previously inaccessible galaxies.

Our understanding of the make-up of the CIB - which, near its peak, has yet to be fully resolved into individual sources - is likely to develop greatly in the coming years, leading to an exciting age for IR astronomy.

Appendix A

The Instrumental Specifications of SAFARI

The proposed JAXA-led SPICA (Space Infrared Telescope for Astronomy and Astrophysics) mission and the SAFARI FIR imaging Fourier Transform spectrometer (Spica FAR-infrared Instrument) instrument concept are, to date (September 2011), still undergoing revisions regarding their technical specifications. The work described in this thesis makes use of a number of different revisions of these specifications, therefore for simplicity I will present the relevant details of these revisions in this appendix.

The original technical specifications of SAFARI (formerly named ESI - European Spica Instrument) are detailed in Swinyard et al. (2009). In this revision SPICA offered a 3.5 m dish, with a diffraction limited angular resolution of $8''$ and a field of view of $2' \times 2'$. The SAFARI instrument was proposed to cover the waveband 30 - 210 μm at resolving power varying from $R \sim 20$ - 2000. The 5σ 10 hour sensitivity of SAFARI was proposed to be 1.7 mJy.

Following this publication the wavelength coverage of SAFARI was revised to 35 - 210 μm (SPICA Study Team Collaboration, 2009).

Most recently, SPICA's physical dish size was decreased to 3.2 m Nakagawa (2010), which decreased SAFARI's 5σ 10 hour sensitivity to 2 mJy (SPICA Study Team Collaboration, 2010).

Bibliography

- Amblard, A., et al. 2010, *Astron. Astrophys.*, 518, L9+
- Armus, L., et al. 2004, *Astrophys. J. Suppl.*, 154, 178
- Barger, A. J., Cowie, L. L., & Wang, W. 2008, *Astrophys. J.*, 689, 687
- Barton, E. J., Geller, M. J., & Kenyon, S. J. 2000, *Astrophys. J.*, 530, 660
- Baugh, C. M., Cole, S., & Frenk, C. S. 1996, *Mon. Not. R. Astr. Soc.*, 283, 1361
- Bell, E. F., & de Jong, R. S. 2000, *Mon. Not. R. Astr. Soc.*, 312, 497
- Bell, E. F., et al. 2005, *Astrophys. J.*, 625, 23
- Blain, A. W., Smail, I., Ivison, R. J., Kneib, J., & Frayer, D. T. 2002, *Physics Reports*, 369, 111
- Bolzonella, M., Miralles, J., & Pelló, R. 2000, *Astron. Astrophys.*, 363, 476
- Bouwens, R. J., Illingworth, G. D., Franx, M., & Ford, H. 2007, *Astrophys. J.*, 670, 928
- Brauher, J. R., Dale, D. A., & Helou, G. 2008, *Astrophys. J. Suppl.*, 178, 280
- Bruzual, G., & Charlot, S. 2003, *Mon. Not. R. Astr. Soc.*, 344, 1000
- Bundy, K., et al. 2006, *Astrophys. J.*, 651, 120

- Bushouse, H. A., et al. 2002, *Astrophys. J. Suppl.*, 138, 1
- Calzetti, D., Armus, L., Bohlin, R. C., Kinney, A. L., Koornneef, J., & Storchi-Bergmann, T. 2000, *Astrophys. J.*, 533, 682
- Cameron, R. M. 1976, *Sky and Telescope*, 52, 327
- Carilli, C. L., & Yun, M. S. 1999, *Astrophys. J. Letters*, 513, L13
- . 2000, *Astrophys. J.*, 530, 618
- Cesarsky, D., Lequeux, J., Abergel, A., Perault, M., Palazzi, E., Madden, S., & Tran, D. 1996, *Astron. Astrophys.*, 315, L305
- Chapman, S. C., Blain, A. W., Smail, I., & Ivison, R. J. 2005, *Astrophys. J.*, 622, 772
- Charlot, S., & Fall, S. M. 2000, *Astrophys. J.*, 539, 718
- Chary, R., & Elbaz, D. 2001, *Astrophys. J.*, 556, 562
- Chini, R., Kreysa, E., Kruegel, E., & Mezger, P. G. 1986, *Astron. Astrophys.*, 166, L8
- Cimatti, A., et al. 2008, *Astron. Astrophys.*, 482, 21
- Clegg, P. E., et al. 1996, *Astron. Astrophys.*, 315, L38
- Clements, D. L., Isaak, K. G., Madden, S. C., & Pearson, C. 2007, *Astron. Astrophys.*, 465, 125
- Clements, D. L., et al. 2008, *Mon. Not. R. Astr. Soc.*, 387, 247
- Cole, S., Lacey, C. G., Baugh, C. M., & Frenk, C. S. 2000, *Mon. Not. R. Astr. Soc.*, 319, 168

- Combes, F. 2005, in American Institute of Physics Conference Series, Vol. 783, The Evolution of Starbursts, ed. S. Hüttmeister, E. Manthey, D. Bomans, & K. Weis, 43–49
- Conselice, C. J., Bershady, M. A., Dickinson, M., & Papovich, C. 2003, *Astron. J.*, 126, 1183
- Coppin, K., et al. 2010, *Astrophys. J.*, 713, 503
- Cowie, L. L., & Barger, A. J. 2008, *Astrophys. J.*, 686, 72
- Cowie, L. L., Songaila, A., Hu, E. M., & Cohen, J. G. 1996, *Astron. J.*, 112, 839
- da Cunha, E., Charlot, S., & Elbaz, D. 2008, *Mon. Not. R. Astr. Soc.*, 388, 1595
- da Cunha, E., Eminian, C., Charlot, S., & Blaizot, J. 2010, *Mon. Not. R. Astr. Soc.*, 403, 1894
- Daddi, E., Cimatti, A., Renzini, A., Fontana, A., Mignoli, M., Pozzetti, L., Tozzi, P., & Zamorani, G. 2004, *Astrophys. J.*, 617, 746
- Daddi, E., et al. 2007, *Astrophys. J.*, 670, 156
- Damen, M., Labbé, I., Franx, M., van Dokkum, P. G., Taylor, E. N., & Gawiser, E. J. 2009, *Astrophys. J.*, 690, 937
- de Graauw, T., et al. 1996, *Astron. Astrophys.*, 315, L49
- . 2010, *Astron. Astrophys.*, 518, L6+
- Devlin, M. J., et al. 2009, *Nature*, 458, 737
- Dole, H., et al. 2001, *Astron. Astrophys.*, 372, 364
- . 2004, *Astrophys. J. Suppl.*, 154, 93

- . 2006, *Astron. Astrophys.*, 451, 417
- Dudley, C. C. 1999, *Mon. Not. R. Astr. Soc.*, 307, 553
- Duley, W. W., & Williams, D. A. 1981, *Mon. Not. R. Astr. Soc.*, 196, 269
- Dunlop, J. S., & Peacock, J. A. 1990, *Mon. Not. R. Astr. Soc.*, 247, 19
- Dunne, L., & Eales, S. A. 2001, *Mon. Not. R. Astr. Soc.*, 327, 697
- Dunne, L., Eales, S. A., & Edmunds, M. G. 2003, *Mon. Not. R. Astr. Soc.*, 341, 589
- Dunne, L., et al. 2009, *Mon. Not. R. Astr. Soc.*, 394, 3
- Dye, S., Eales, S. A., Ashby, M. L. N., Huang, J., Egami, E., Brodwin, M., Lilly, S., & Webb, T. 2007, *Mon. Not. R. Astr. Soc.*, 375, 725
- Dye, S., et al. 2008, *Mon. Not. R. Astr. Soc.*, 386, 1107
- Eales, S., Bertoldi, F., Ivison, R., Carilli, C., Dunne, L., & Owen, F. 2003, *Mon. Not. R. Astr. Soc.*, 344, 169
- Eales, S., Lilly, S., Gear, W., Dunne, L., Bond, J. R., Hammer, F., Le Fèvre, O., & Crampton, D. 1999, *Astrophys. J.*, 515, 518
- Eales, S. A., et al. 2010, *Astron. Astrophys.*, 518, L23+
- Efstathiou, A., & Rowan-Robinson, M. 1995, *Mon. Not. R. Astr. Soc.*, 273, 649
- . 2003, *Mon. Not. R. Astr. Soc.*, 343, 322
- Efstathiou, A., Rowan-Robinson, M., & Siebenmorgen, R. 2000, *Mon. Not. R. Astr. Soc.*, 313, 734

- Elbaz, D., Cesarsky, C. J., Chanical, P., Aussel, H., Franceschini, A., Fadda, D., & Chary, R. R. 2002, *Astron. Astrophys.*, 384, 848
- Elbaz, D., et al. 1999, *Astron. Astrophys.*, 351, L37
- . 2007, *Astron. Astrophys.*, 468, 33
- Elston, R., Rieke, G. H., & Rieke, M. J. 1988, *Astrophys. J. Letters*, 331, L77
- Erb, D. K., Steidel, C. C., Shapley, A. E., Pettini, M., Reddy, N. A., & Adelberger, K. L. 2006, *Astrophys. J.*, 647, 128
- Farrah, D., et al. 2001, *Mon. Not. R. Astr. Soc.*, 326, 1333
- . 2007, *Astrophys. J.*, 667, 149
- Faure, C., et al. 2008, *Astrophys. J. Suppl.*, 176, 19
- Fazio, G. G., et al. 2004, *Astrophys. J. Suppl.*, 154, 10
- Feulner, G., Gabasch, A., Salvato, M., Drory, N., Hopp, U., & Bender, R. 2005, *Astrophys. J. Letters*, 633, L9
- Flores, H., et al. 1999, *Astrophys. J.*, 517, 148
- Förster Schreiber, N. M., Genzel, R., Lutz, D., Kunze, D., & Sternberg, A. 2001, *Astrophys. J.*, 552, 544
- Franx, M., et al. 2003, *Astrophys. J. Letters*, 587, L79
- Genzel, R., & Cesarsky, C. J. 2000, *Ann. Rev. Astron. Astrophys.*, 38, 761
- Genzel, R., et al. 1998, *Astrophys. J.*, 498, 579
- Glazebrook, K., et al. 2004, *Nature*, 430, 181
- Griffin, M. J., et al. 2010, *Astron. Astrophys.*, 518, L3+

- Haarsma, D. B., Partridge, R. B., Windhorst, R. A., & Richards, E. A. 2000, *Astrophys. J.*, 544, 641
- Hailey-Dunsheath, S. 2008, PhD thesis, Cornell University
- Hauser, M. G., & Dwek, E. 2001, *Ann. Rev. Astron. Astrophys.*, 39, 249
- Heavens, A., Panter, B., Jimenez, R., & Dunlop, J. 2004, *Nature*, 428, 625
- Hogg, D. W., Cohen, J. G., Blandford, R., & Pahre, M. A. 1998, *Astrophys. J.*, 504, 622
- Holland, W. S., et al. 1999, *Mon. Not. R. Astr. Soc.*, 303, 659
- Hopkins, A. M. 2004, *Astrophys. J.*, 615, 209
- Houck, J. R., et al. 2004, *Astrophys. J. Suppl.*, 154, 18
- Hughes, D. H., et al. 1998a, *Nature*, 394, 241
- . 1998b, *Nature*, 394, 241
- Imanishi, M., Dudley, C. C., Maiolino, R., Maloney, P. R., Nakagawa, T., & Risaliti, G. 2007, *Astrophys. J. Suppl.*, 171, 72
- Ivison, R. J., Smail, I., Le Borgne, J., Blain, A. W., Kneib, J., Bezecourt, J., Kerr, T. H., & Davies, J. K. 1998, *Mon. Not. R. Astr. Soc.*, 298, 583
- Jeong, W., Pearson, C. P., Lee, H. M., Pak, S., & Nakagawa, T. 2006, *Mon. Not. R. Astr. Soc.*, 369, 281
- Joint Astronomy Centre. 2004, Atmospheric Transmission, <http://www.jach.hawaii.edu/>, accessed: 15/09/2011
- Juneau, S., et al. 2005, *Astrophys. J. Letters*, 619, L135

- Juvela, M., Mattila, K., & Lemke, D. 2000, *Astron. Astrophys.*, 360, 813
- Kennicutt, Jr., R. C., Tamblyn, P., & Congdon, C. E. 1994, *Astrophys. J.*, 435, 22
- Kessler, M. F., et al. 1996, *Astron. Astrophys.*, 315, L27
- Koekemoer, A. M., et al. 2007, *Astrophys. J. Suppl.*, 172, 196
- Kriek, M., et al. 2006, *Astrophys. J. Letters*, 649, L71
- . 2008, *Astrophys. J.*, 677, 219
- Laurent, O., Mirabel, I. F., Charmandaris, V., Gallais, P., Madden, S. C., Sauvage, M., Vigroux, L., & Cesarsky, C. 2000, *Astron. Astrophys.*, 359, 887
- Le Fèvre, O., et al. 2000, *Mon. Not. R. Astr. Soc.*, 311, 565
- Le Floc'h, E., et al. 2005, *Astrophys. J.*, 632, 169
- Lemke, D., et al. 1996, *Astron. Astrophys.*, 315, L64
- Lilly, S. J., Le Fevre, O., Hammer, F., & Crampton, D. 1996, *Astrophys. J. Letters*, 460, L1+
- Lutz, D., Sturm, E., Genzel, R., Moorwood, A. F. M., Alexander, T., Netzer, H., & Sternberg, A. 2000, *Astrophys. J.*, 536, 697
- Madau, P., Pozzetti, L., & Dickinson, M. 1998, *Astrophys. J.*, 498, 106
- Marsden, G., et al. 2009, *Astrophys. J.*, 707, 1729
- Melbourne, J., Koo, D. C., & Le Floc'h, E. 2005, *Astrophys. J. Letters*, 632, L65
- Menéndez-Delmestre, K., et al. 2007, *Astrophys. J. Letters*, 655, L65
- . 2009, *Astrophys. J.*, 699, 667

- Moncelsi, L., et al. 2011, *Astrophys. J.*, 727, 83
- Morgan, H. L., & Edmunds, M. G. 2003, *Mon. Not. R. Astr. Soc.*, 343, 427
- Nakagawa, T. 2010, in *Society of Photo-Optical Instrumentation Engineers (SPIE) Conference Series*, Vol. 7731, *Society of Photo-Optical Instrumentation Engineers (SPIE) Conference Series*
- Negishi, T., Onaka, T., Chan, K., & Roellig, T. L. 2001, *Astron. Astrophys.*, 375, 566
- Neugebauer, G., et al. 1984, *Astrophys. J. Letters*, 278, L1
- Nguyen, H. T., et al. 2010, *Astron. Astrophys.*, 518, L5+
- Noeske, K. G., et al. 2007, *Astrophys. J. Letters*, 660, L43
- Oke, J. B., et al. 1995, *Publs. Astr. Soc. Pacif.*, 107, 375
- Oliver, S., et al. 2000, *Mon. Not. R. Astr. Soc.*, 316, 749
- . 2010, *Mon. Not. R. Astr. Soc.*, 405, 2279
- Pannella, M., et al. 2009, *Astrophys. J. Letters*, 698, L116
- Papovich, C., et al. 2004, *Astrophys. J. Suppl.*, 154, 70
- Pascale, E., et al. 2009, *Astrophys. J.*, 707, 1740
- Patton, D. R., et al. 2002, *Astrophys. J.*, 565, 208
- Pearson, C. 2005, *Mon. Not. R. Astr. Soc.*, 358, 1417
- Pearson, C., & Khan, S. A. 2009, *Mon. Not. R. Astr. Soc.*, 399, L11
- Pearson, C., & Rowan-Robinson, M. 1996, *Mon. Not. R. Astr. Soc.*, 283, 174

- Pearson, C. P. 2001, *Mon. Not. R. Astr. Soc.*, 325, 1511
- Pearson, C. P., et al. 2007, *Advances in Space Research*, 40, 605
- Pérez-González, P. G., Trujillo, I., Barro, G., Gallego, J., Zamorano, J., & Conselice, C. J. 2008, *Astrophys. J.*, 687, 50
- Pérez-González, P. G., et al. 2005, *Astrophys. J.*, 630, 82
- Pilbratt, G. L. 2004, in *Presented at the Society of Photo-Optical Instrumentation Engineers (SPIE) Conference*, Vol. 5487, *Society of Photo-Optical Instrumentation Engineers (SPIE) Conference Series*, ed. J. C. Mather, 401–412
- Pilbratt, G. L., et al. 2010, *Astron. Astrophys.*, 518, L1+
- Poglitsch, A., et al. 2010, *Astron. Astrophys.*, 518, L2+
- Pope, A., et al. 2006, *Mon. Not. R. Astr. Soc.*, 370, 1185
- . 2008, *Astrophys. J.*, 675, 1171
- Price, R., & Duric, N. 1992, *Astrophys. J.*, 401, 81
- Priddey, R. S., & McMahon, R. G. 2001, *Mon. Not. R. Astr. Soc.*, 324, L17
- Puget, J. L., & Leger, A. 1989, *Ann. Rev. Astron. Astrophys.*, 27, 161
- Raymond, G., Isaak, K. G., Clements, D., Rykala, A., & Pearson, C. 2010, *Publ. Astron. Soc. Japan*, 62, 697
- Reddy, N. A., Erb, D. K., Steidel, C. C., Shapley, A. E., Adelberger, K. L., & Pettini, M. 2005, *Astrophys. J.*, 633, 748
- Rieke, G. H., et al. 2004, *Astrophys. J. Suppl.*, 154, 25

- Rigopoulou, D., Spoon, H. W. W., Genzel, R., Lutz, D., Moorwood, A. F. M., & Tran, Q. D. 1999, *Astron. J.*, 118, 2625
- Rodighiero, G., et al. 2010, *Astron. Astrophys.*, 518, L25+
- Roseboom, I. G., et al. 2010, *Mon. Not. R. Astr. Soc.*, 409, 48
- Rowan-Robinson, M. 1968, *Mon. Not. R. Astr. Soc.*, 138, 445
- Rowan-Robinson, M., & Crawford, J. 1989, *Mon. Not. R. Astr. Soc.*, 238, 523
- Rowan-Robinson, M., et al. 2004, *Mon. Not. R. Astr. Soc.*, 351, 1290
- Rush, B., Malkan, M. A., & Spinoglio, L. 1993, *Astrophys. J. Suppl.*, 89, 1
- Sanders, D. B., & Mirabel, I. F. 1996, 34, 749
- Sanders, D. B., Soifer, B. T., Elias, J. H., Madore, B. F., Matthews, K., Neugebauer, G., & Scoville, N. Z. 1988, *Astrophys. J.*, 325, 74
- Saunders, W., et al. 2000, *Mon. Not. R. Astr. Soc.*, 317, 55
- Scheuer, P. A. G. 1957, in *Proceedings of the Cambridge Philosophical Society*, Vol. 53, *Proceedings of the Cambridge Philosophical Society*, 764–773
- Schmidt, M. 1968, *Astrophys. J.*, 151, 393
- Scott, K. S., et al. 2008, *VizieR Online Data Catalog*, 738, 52225
- Scott, S. E., et al. 2002, *Mon. Not. R. Astr. Soc.*, 331, 817
- Scoville, N., et al. 2007, *Astrophys. J. Suppl.*, 172, 150
- Smail, I., Ivison, R. J., Blain, A. W., & Kneib, J. 2002, *Mon. Not. R. Astr. Soc.*, 331, 495

- Smail, I., Ivison, R. J., Owen, F. N., Blain, A. W., & Kneib, J. 2000, *Astrophys. J.*, 528, 612
- Smith, J. D. T., et al. 2004, *Astrophys. J. Suppl.*, 154, 199
- Smolčić, V., et al. 2011, *Astrophys. J. Letters*, 731, L27+
- Soifer, B. T., & Neugebauer, G. 1991, *Astron. J.*, 101, 354
- SPICA Study Team Collaboration. 2009, private communication
- . 2010, private communication
- Spinoglio, L., Gruppioni, C., Franceschini, A., Valiante, E., & Isaak, K. G. 2011, submitted
- Sturm, E., Lutz, D., Tran, D., Feuchtgruber, H., Genzel, R., Kunze, D., Moorwood, A. F. M., & Thornley, M. D. 2000, *Astron. Astrophys.*, 358, 481
- Sturm, E., Lutz, D., Verma, A., Netzer, H., Sternberg, A., Moorwood, A. F. M., Oliva, E., & Genzel, R. 2002, *Astron. Astrophys.*, 393, 821
- Sturm, E., et al. 1996, *Astron. Astrophys.*, 315, L133
- Swinyard, B., et al. 2009, *Experimental Astronomy*, 23, 193
- Veilleux, S., Kim, D.-C., & Sanders, D. B. 2002, *Astrophys. J. Suppl.*, 143, 315
- Veilleux, S., et al. 2006, *Astrophys. J.*, 643, 707
- Vlahakis, C., Eales, S., & Dunne, L. 2007, *Mon. Not. R. Astr. Soc.*, 379, 1042
- Wall, J. V. 1996, *Q. Jl. R. Astr. Soc.*, 37, 519
- Wall, J. V., Pope, A., & Scott, D. 2008, *Mon. Not. R. Astr. Soc.*, 383, 435
- Werner, M. W., et al. 2004, *Astrophys. J. Suppl.*, 154, 1

Williams, R. E., et al. 1996, *Astron. J.*, 112, 1335

Wilson, G. W., et al. 2008, *Mon. Not. R. Astr. Soc.*, 386, 807

Younger, J. D., et al. 2007, *Astrophys. J.*, 671, 1531

Yun, M. S., Reddy, N. A., & Condon, J. J. 2001, *Astrophys. J.*, 554, 803

Zaritsky, D., Kennicutt, Jr., R. C., & Huchra, J. P. 1994, *Astrophys. J.*, 420, 87

Zheng, X. Z., Hammer, F., Flores, H., Assémat, F., & Pelat, D. 2004, *Astron. Astrophys.*, 421, 847